

國立台灣大學機械工程學系

碩士論文

Department of Mechanical Engineering

College of Engineering


National Taiwan University

Master Thesis

穩態乾顆粒流經障礙物之作用力：即時量測與藉影像分析之估測

In-Situ and Image-Based Force Measurement for a Steady Dry

Granular Flow Over an Obstacle



江明哲

Ming-Jhe Jiang

指導教授：楊馥菱 博士

Advisor: Fu-Ling Yang, Ph.D.

中華民國 101 年 4 月

January, 2012

國立臺灣大學 (碩) 博士學位論文
口試委員會審定書

穩態乾顆粒流經障礙物之作用力: 即時量測
與藉影像分析之估測

**In-Situ and Image-Based Force Measurements for a Steady Dry
Granular flow Over an Obstacle**

本論文係江明哲 (R98522106) 在國立臺灣大學機械工程學系完成之碩 (博) 士學位論文, 於民國 101 年 1 月 16 日承下列考試委員
審查通過及口試及格, 特此證明

口試委員:

楊復春

(簽名)

(指導教授)

蕭述三

Herrn Gjak

系主任

楊耀州

(簽名)

誌謝

碩士的求學過程，對大多數人來說或許只是一個必經的過程；但對我來說，這兩年半的日子另我成長許多。我很慶幸能碰上我的指導教授，楊馥菱老師；在我不知所從的時候，她以一個良師的身分激勵我並指引我方向；在我懵懵懂懂的時候，她以一個朋友的身分告訴我如何堅強自己的心靈並且找到自己的目標。在最後的半年時間裡，為了趕上我下一階段的目標，我投入了所有的心力和老師一起催生了這篇論文；謝謝老師不厭其煩的替我校稿並指引我撰寫的方向與靈感，感謝永達與庚霖，替我的理論發現缺失，並且在我煩悶的時候適時的與我分享心情；感謝學弟峻華，在我焦頭爛額之際幫助我撰寫最不擅長的自動控制程式；感謝我的父母親，是你們對我的教育另我得以在碩士的求學過程中保持樂觀的態度；感謝所有曾經幫助過和指導過我的人，沒有你們的幫助，這篇論文絕對無法完成。

最後，我想感謝我的伴侶，劉薰綺小姐；在每個煩悶緊張的周末，是妳的陪伴讓我得以紓解壓力，感謝妳不厭其煩的聽我抱怨碰到的困難，並不離不棄的陪在我身邊；即使妳自己常覺得沒有對我的課業有任何實質上的幫助，但少了妳的存在，我最後半年的日子就不會是彩色的。

CONTENTS

List of Figures	4
List of Tables	6
Abstract	7
摘要	8
Chapter 1 Introduction and Motivation	9
Chapter 2 Experimental Setup	12
2.1 Facilities.....	12
2.1.1 Reservoir, Chute, and Granular materials.....	13
2.1.2 Image Acquisition System.....	14
2.1.3 Load Cell and the Signal Acquisition System.....	15
2.1.4 Static Calibration of Load Cells.....	20
Chapter 3 Image Processing and Load-cell Signal Analysis	26
3.1 Procedures of Image Analysis.....	26
3.1.1 Locating spheres with Circular Hough Transformation and its Error.....	26
3.1.2 Particle Tracking Velocimetry and its Error.....	31
3.1.3 Average Scheme for Bulk Properties.....	33
Chapter 4 Granular Discharge Analysis	36
4.1 Experiment Facility and Procedure.....	36
4.2 Definition of Steady or Decaying Discharging Region.....	38
4.2.1 Deviation Time and Fitting Rules.....	41
4.2.2 Temporal profiles of decaying discharge.....	46
4.3 Image-Based Analysis of Granular Flow Dynamics.....	55
4.3.1 Depth Profile for Bulk Velocity and Solid-Volume Fraction.....	57
4.3.2 Decaying Bulk Velocity and Solid-Volume Fraction.....	71
Chapter 5 Impact Force of a Steady dry Granular Flow	79
5.1 Experimental Facility.....	79
5.2 Impact, Shear and Normal Signals.....	80
5.3 Methodology of Image Analysis.....	93
5.3.1 Force Measurements From Images: Control Volume Analysis and Reynolds Transport Theorem.....	93
5.4 Comparison of Force Data from Load-Cell and Control Volume Analysis of Images.....	99
Chapter 6 Conclusions and Future Aspect	114
Reference	120

List of Figures

Figure 2.1 Schematic diagram of the experiment facilities.....	13
Figure 2.2 Illustration of camera orientation adjustment.....	15
Figure 2.3 Arrangement of the three load cells in the sensing module.....	19
Figure 2.4 The second load cell box that measures total normal load.....	19
Figure 2.5 Separation zone of each load cell surface.....	21
Figure 2.6 Static calibration results of front plate.....	22
Figure 2.7 Static calibration results of top plate.....	23
Figure 2.8 Static calibration results of tension plate.....	24
Figure 3.1 Principles of linear Hough transformation.....	27
Figure 3.2 Principles of circular Hough transformation.....	28
Figure 3.3 The Laplace (left) and Gaussian (right) filter.....	28
Figure 3.4 (a) original RGB image.....	29
(b) gray image.....	29
(c) filtered image that strong contract at the circumference.....	29
(d) sphere centers located by circular Hough transformation.....	29
Figure 3.5 Circular Hough Transformation error.....	30
Figure 3.6 Illustration of the concept of the nearest neighbor method.....	32
Figure 3.7 Illustration of the area-weighted average scheme.....	34
Figure 3.8 Temporal voltage data after (left) and before (right) filtering.....	35
Figure 4.1 (a) reservoir with packing height H and width W specified.....	37
(b) schematic diagram of experiment facility.....	37
(c) observation line defined along the connection guide.....	38
(d) averaging box and its vertical shift distance.....	38
Figure 4.2 The temporal profiles for the accumulated discharge weight.....	40
Figure 4.3 The deviation time for the onset of unsteady discharge.....	44
Figure 4.4 Double log of the weight difference, ΔW , versus log-scale time.....	50
Figure 4.5 Different trends of decaying discharge profiles.....	51
Figure 4.6 Exponents A and B.....	53
Figure 4.7 Instantaneous depth profile of bulk velocity for W=6cm.....	60
Figure 4.8 Instantaneous depth profile of solid volume fraction for W=6cm.....	61
Figure 4.9 Instantaneous depth profile of bulk velocity for W=24cm.....	63
Figure 4.10 Instantaneous depth profile of solid volume fraction for W=24cm.....	64
Figure 4.11 Illustration of the mismatching nearest neighbor method.....	65
Figure 4.12 The instantaneous mass flow rate comparison.....	68
Figure 4.13 The instantaneous difference on mass flow rate.....	69
Figure 4.14 Depth-averaged bulk velocity for different packing width.....	72
Figure 4.15 Depth-averaged bulk velocity at different locations.....	73

Figure 4.16	Depth-averaged bulk solid volume fraction for different packing width.	74
Figure 4.17	Depth-averaged bulk solid volume fraction at different locations.	75
Figure 4.18	Comparison of 10% local decay in $\bar{\phi}(t)$ to $U(t)$.	78
Figure 5.1	Experimental facility:	
	(a) the chute and where the load cell module was installed.	80
	(b) flow depth h from the load cell top surface to the base.	80
Figure 5.2	Force components for steady flows down a chute of $h=4.8$ cm and 20° .	82
Figure 5.3	Packing formation for the spheres arrested in front of the impact load cell for chute of 2.4 cm depth and 20° inclination:	
	(a) close orderly packing and.	83
	(b) loose and random packing.	83
Figure 5.4	Force components for steady flows down a chute of $h=2.4$ cm, $\theta=20^\circ$.	85
Figure 5.5	Force components for steady flows down a chute of $h=2.4$ cm, $\theta=23^\circ$.	87
Figure 5.6	Force components for steady flows down a chute of $h=2.4$ cm, $\theta=26^\circ$.	88
Figure 5.7	Stationary zone in front of the impact cell for chute of depth $h=4.8$ cm.	90
Figure 5.8	Force components for steady flows down a chute of $h=4.8$ cm at $\theta=23^\circ$.	90
Figure 5.9	Force components for steady flows down a chute of $h=4.8$ cm at $\theta=26^\circ$.	91
Figure 5.10	Shear and normal force components for steady flows down a chute of height $h=4.8$ cm at (a) $\theta=23^\circ$ and (b) $\theta=26^\circ$.	92
Figure 5.11	Control volume at two instants.	94
Figure 5.12	Two control volumes, CV1 and CV2.	95
Figure 5.13	Comparison of impact force obtained from control volume analysis and in-situ load cell measurement for $h=4.8$ cm and $\theta=23^\circ$.	101
Figure 5.14	Comparison of impact force obtained from control volume analysis and in-situ load cell measurement for $h=4.8$ cm and $\theta=26^\circ$.	103
Figure 5.15	Comparison of impact force using control volume of 2/3- and 1/3-original width for $W=6$ cm at (a)-(b): $\theta=23^\circ$ and (c)-(d): $\theta=26^\circ$.	105
Figure 5.16	Impact force using manual PTV results in the control volume analysis using 1/3 width of the original length for $W=6$ cm, at $\theta=23^\circ$ and 26° .	106
Figure 5.17	Impact force using manual PTV for flows at $\theta=23^\circ$. Control volume analysis using 1/3 (a) and 2/3 (b) CV width.	108
Figure 5.18	Impact force using manual PTV for flows at $\theta=26^\circ$. Control volume analysis using 1/3 (a) and 2/3 (b) CV width.	109
Figure 5.19	Normal and shear force obtained from control volume analysis for dry granular flows down a chute of $h=4.8$ cm and $\theta=23^\circ$.	110
Figure 5.20	Normal and shear force obtained from control volume analysis for dry granular flows down a chute of $h=4.8$ cm and $\theta=26^\circ$.	111

List of Tables

Table 2.1 Specification of the normal force load cell.....17
Table 2.2 Specification of the shear force load cell.....18
Table 2.3 Results of static calibration.....24
Table 3.1 The average and the standard deviation of the center location error.....30
Table 3.2 Mean and standard deviation of instantaneous velocity error.....33
Table 4.1 Overall decay level for flows from different packing widths.....76
Table 4.2 Local decay level for flows from different packing widths.....77
Table 5.1 Shear force estimated from CV analysis of manual PTV data.....112



Abstract

This work attempts direct and indirect measurements for the force developed by a steady dry granular flow down an incline as it impinges and runs over an obstacle constructed by putting together two load cells and one shear cell. Three load cells were implemented to achieve in-situ measurements of the impact force, the tangential friction, and the overhead normal loads. High-speed imaging technique and relevant image analysis were employed to estimate depth profiles of the flow density and velocity which information were further integrated into a two-dimensional control volume analysis to estimate the corresponding force components using the requirement of streamwise momentum conservation. The force data obtained from the 3D in-situ and 2D indirect measurements agree well over the inspected inclination angles, 23° and 26° , provided that the flow is not too loose or too thin for which erroneous PTV is inevitable. In addition, we also discover unique temporal profiles for reservoir discharge and explanations are given based on relevant high-speed imaging analysis.

摘要

本實驗探討流經傾斜滑道的穩態乾顆粒流，並以兩顆荷重元與一張力感測器組成長方形障礙物，以即時量測顆粒流跨越障礙物時所產生的衝擊力，荷重力，與側向摩擦力。同時輔以高速照相機由滑道側邊拍攝顆粒流之行為，配合影像分析求得顆粒流之速度與密度，進一步以體積控制分析(control volume analysis)計算顆粒流所產生的力並與即時量測之衝擊力，荷重力，與側向摩擦力比較。體積控制分析與即時量測的結果吻合，同時在比較的過程之中發現質點軌跡測速法(PTV)無法作用於顆粒流過於稀疏的情況。

在產生穩態顆粒流的過程，發現儲存槽內不同的堆積幾何形狀會影響出口的顆粒排放速度，當堆積的長度小於某一特定長度時，流出的顆粒總量與時間的關係會呈現出不同的趨勢。為解釋此現象，我們以高速影像探討其可能原因。

Chapter 1 Introduction and Motivation

A granular flow is the collective motion of dry solid particles and has been an active research topic in the past decades for its common appearance in industrial applications and natural hazards. Extensive investigations have been conducted on the dynamics of steady granular flows in specific configurations—including those in a shear cell or a rotating drum, down an inclined flume or a hopper, and in a horizontal or vertical shaking bed.

Several theoretical or semi-empirical models have also been proposed for flows under different flow conditions. However, research on how such flow may interact with a non-smooth solid boundary—for example, an obstacle—is rare. Such knowledge is important for homeland security since the impact and erosion of a granular flow could destroy infrastructure like a, check dam, a bridge column, or an open channel..., etc. Thus, the primary goal of this work sets out to study the force generated by a dry granular flow down an incline when it runs over an obstacle.

In recent years, the technique of high-speed digital imaging has been a popular measuring means for granular flow dynamics. Since the granulates are opaque or with only limited degree of transparency, the imaging technique is often limited to bulk motion at its top or lateral surfaces. Bulk dynamics—including both its density and velocity fields—is thus limited to two-dimensional and feasible extension to an

equivalent three-dimensional behavior is yet a challenging task. Though the method of refractive index matching has been utilized to achieve imaging into the mixture of solid granulates and coexisting liquid of nearly matched refractive index, it is not applicable to dry granular materials. Thus, it is always desirable to evaluate the image-based two-dimensional description by some three-dimensional in-situ measurements, which is the second objective of this work.

We attempt three-dimensional in-situ measurement of the interaction force between a steady granular flow and an in-flow obstacle by implementing load cells as the obstacle. High-speed imaging technique is employed to capture the bulk motion around the load cell simultaneously from the lateral side. The two-dimensional images are analyzed and integrated into a control volume analysis to estimate the corresponding interaction forces under the requirement of total momentum conservation. Feasibility of such indirect image-based force estimation can be evaluated by comparing the data to the in-situ force measurements. We learned that some three-dimensional flow dynamics cannot be captured by the two-dimensional image-based analysis due primarily to the limitation of the current image processing algorithms. The deficiency in the current imaging technique undoubtedly motivates further research for novel hardware integration or algorithm (software) development.

A sidetrack investigation of this work is the discharge nature of a granular mass

out of a reservoir. To prepare a steady dry granular flow over an obstacle on an inclined chute, we released reservoir spheres from a lateral gate and measure the discharging mass flow rate to determine steadiness. Though a great deal has been learned on vertical discharge from a hopper or an hourglass, our knowledge on lateral discharge is rather limited. However, lateral release is preferred to facilitate a chute flow and thus our primary task is know under what conditions a steady discharge is guaranteed. We fixed the gate opening but varied the packing geometry and interesting discharging behaviors are revealed which phenomenon has not been reported before to the best of our knowledge.

The contents of this thesis are organized as follows. Chapter 2 describes the experimental facility and the corresponding calibrations; Chapter 3 firstly introduces the algorithms of image analysis and it continues to describe how the in-situ load cell signals are processed; Chapter 4 studies the reservoir discharge behaviors and its correlation with flow local rheology; Chapter 5 presents the desired force measurements when a steady dry granular flow runs over an obstacle on an inclined chute. We first present how load cells are implemented in the obstacle to achieve in-situ force measurements. We continue to describe how we employ high-speed imaging techniques to estimate, indirectly, the corresponding force components via standard control volume analysis. Chapter 6 concludes this thesis.

Chapter 2 Experimental Setup

A rectangular reservoir was placed on a hoister with its exit connected to a chute of identical width by a short guide. Experiment particles were placed in the reservoir with different depth and width. A load cell sensing module was installed downstream on the chute and once the particles were released from the reservoir, granular flow developed and ran over the load cell module producing a sequence of force signals. The corresponding flow motion was recorded from the side via a high speed digital camera and the captured image sequence was processed for further analysis. The overall schematic diagram of the experiment facility is shown in figure

2.1.

2.1 Facilities

The experiment facility is composed of the following parts: (a) a rectangular reservoir and a short guide, (b) granular materials, (c) an inclined chute connected to reservoir, (d) load cell sensing module and signal acquisition system, and (e) image acquisition system and illumination facility. The arrangement of these components can be found in figure 2.1.

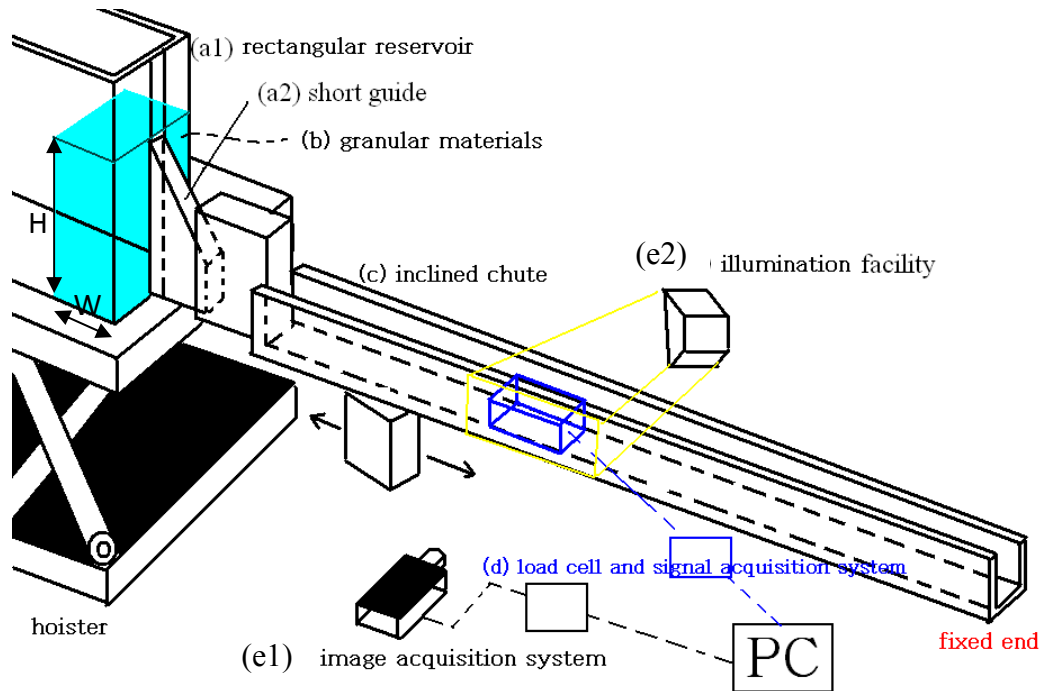


Figure 2.1 Schematic diagram of the experiment facilities.

2.1.1 Reservoir, Chute, and Granular materials

The reservoir is made of acrylic with dimension 90cm in length, 50cm in width, and 60cm in height. The reservoir has an opening of 7cm -width whose height can be adjusted by a sliding gate which was fixed to 10cm throughout this work. The reservoir is placed on a hoister with a 4 -degree inclination to hoister horizontal surface. Experimental particles are mono-sized Polyoxymethylene (POM) spheres of diameter 0.59cm and individual weight of $0.2 \pm 0.002\text{g}$. These dry spheres are poured randomly into the reservoir to a fixed depth, $H=40\text{cm}$, but different packing width, $W=6, 12, 18$ and 24cm were prepared. The chute is also made of acrylic wall of thickness 1cm and the chute is 220cm in length, 7cm in width, and 20cm in height.

The chute inclination angle can be adjusted by moving a solid block to different horizontal locations beneath the chute (see figure 2.1). By sliding open the gate to its fixed height, the stacked spheres can flow out of the reservoir, along the short guide and onto the inclined chute.

2.1.2 Image Acquisition System

High-speed digital camera was employed to record the particle motion. The shooting rate should be fast enough to avoid blurring images and 600 frames per second (FPS) was chosen by trial and error. In chapter 3, we will state how this particular frame rate was determined. For the present image processing, we need good illumination, strong contrast between the spheres and the background, and accurate camera orientation with respect to the flume lateral walls. Thus, one 1000-watt halogen lamp was placed at the front side of chute to illuminate the spheres. To adjust the camera orientation, we firstly used a gradienter to make sure that the camera inclination angle from the horizontal was the same as that of the chute. Next, a mirror was placed at the chute lateral wall facing the camera. A laser pointer was placed on the top of camera to emit a continuous ray and the camera was rotated about the vertical until the reflected laser hit the emitting point. All these manipulations are illustrated in figure 2.2.

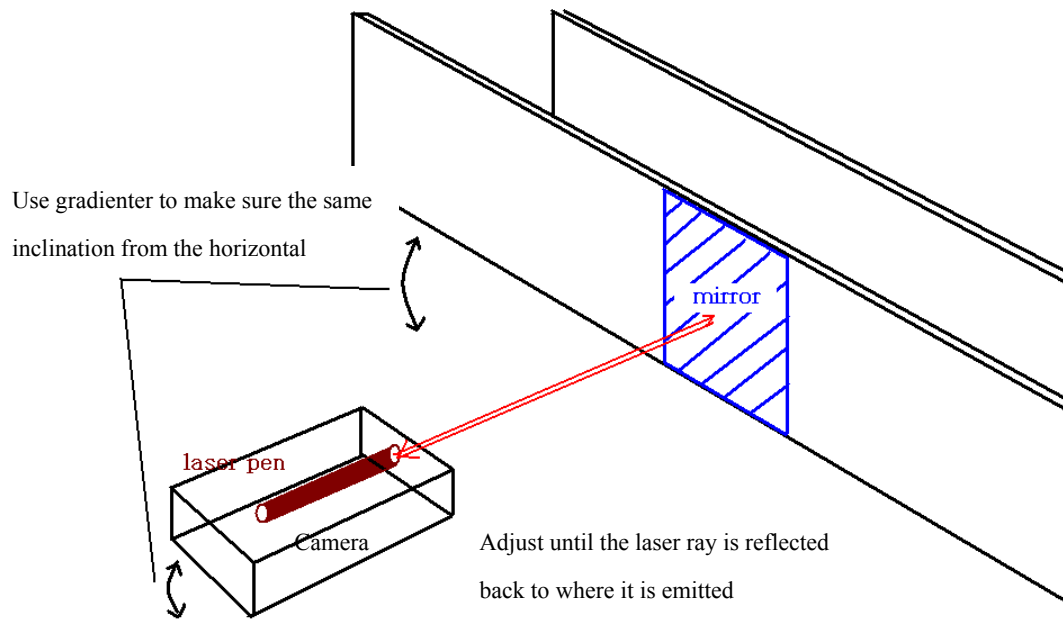


Figure 2.2 Illustration of camera orientation adjustment.

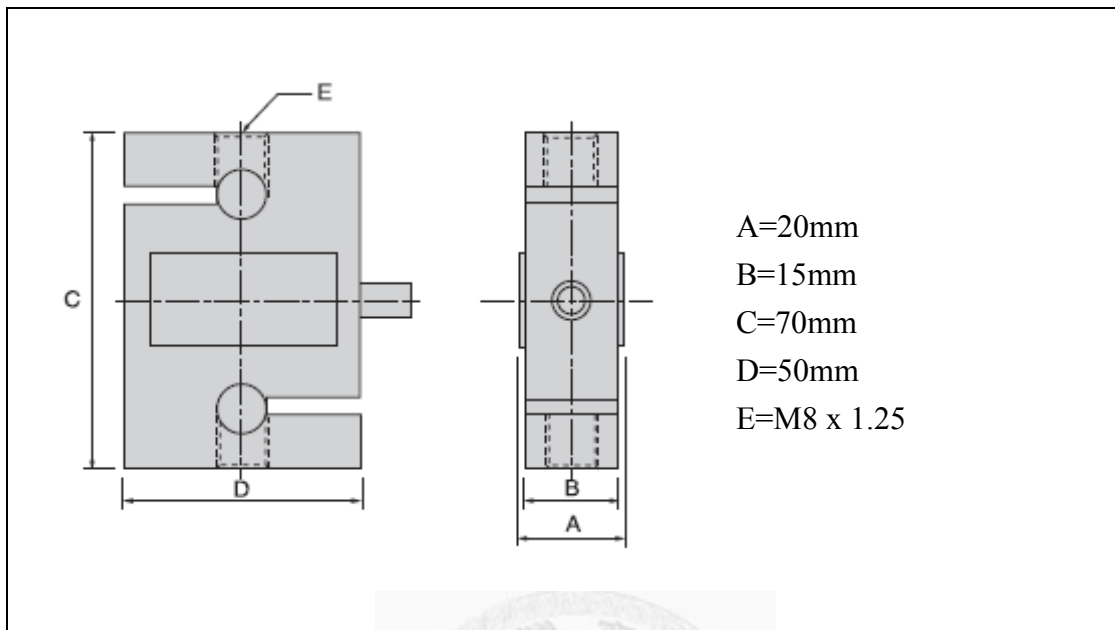
2.1.3 Load Cell and the Signal Acquisition System

Two types of load cells were employed in this work (Model S50 and S25, Esense Scientific Company); one for normal force measurement and the other for shear force measurement. The specification of these load cells are provided in Table 2.1 and Table 2.2, respectively. In order to make sure these load cells can stay intact while receiving the impact of granular flow, a load cell box was designed to host these load cells giving the aforementioned *sensing module* in this work. The box dimensions was 16cm in length, 7.5cm in width, and 8cm in height and is made of aluminum oxide. The load box arrangement is shown in figure 2.3, with the front load

cell measuring the impact force, one rear for top normal force and the other rear component sensing the shear force. Further, another box containing only two normal force load cells are designed to measure the overload as shown in figure 2.4. This box was employed to check the reservoir discharge whose function will be introduced into further details later. The load cell data was acquired by a NI9237 (National Instrument Corporation) data –acquisition card. This 4-channel and full-bridge acquisition model can simultaneously sample the four channels at the highest frequency of 50K/sec. On-board analog-to-digital converter of 24-bit resolution transfers the load cell signals to personal computer via an USB 2.0 interface.

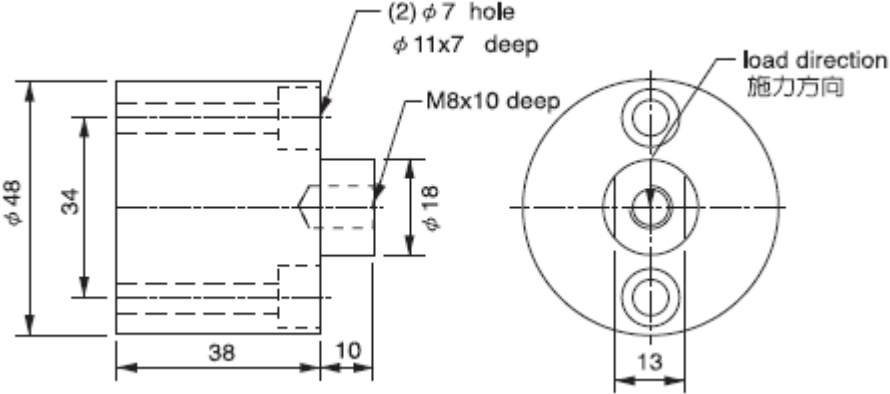


Table 2.1 Specification of the normal force load cell.



Rated Output	2.0mv/v
Total Error	0.05% R.O.
Input Resistance	430 or 405 \pm 25 Ω
Output Resistance	350 \pm 5 Ω
Save Overload Rating	50Kg x 150%

Table 2.2 Specification of the shear force load cell.

	
Rated Output	1.0mv/v
Total Error	0.3% R.O.
Input Resistance	420 ± 15Ω
Output Resistance	350Ω
Save Overload Rating	20Kg x 300%

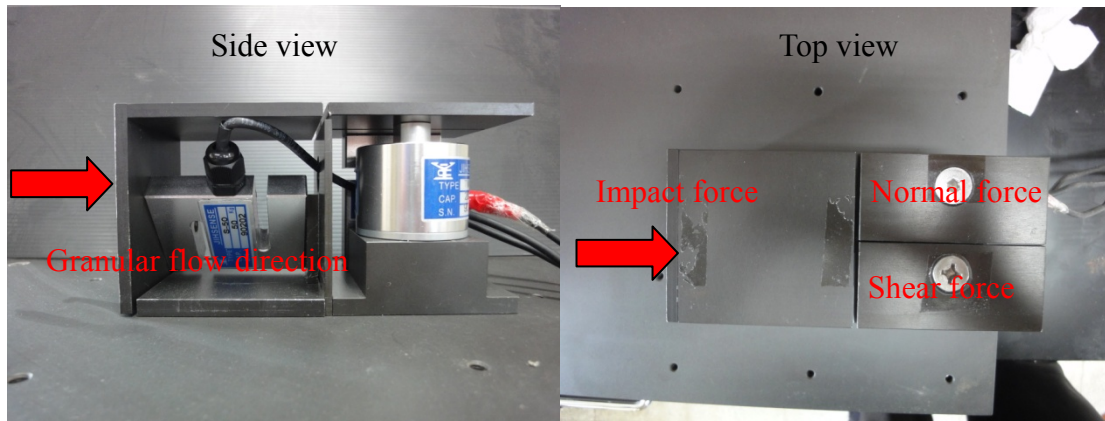


Figure 2.3 Arrangement of the three load cells in the sensing module with the incoming flow direction indicated by the arrow. Left: side view; right: top view.

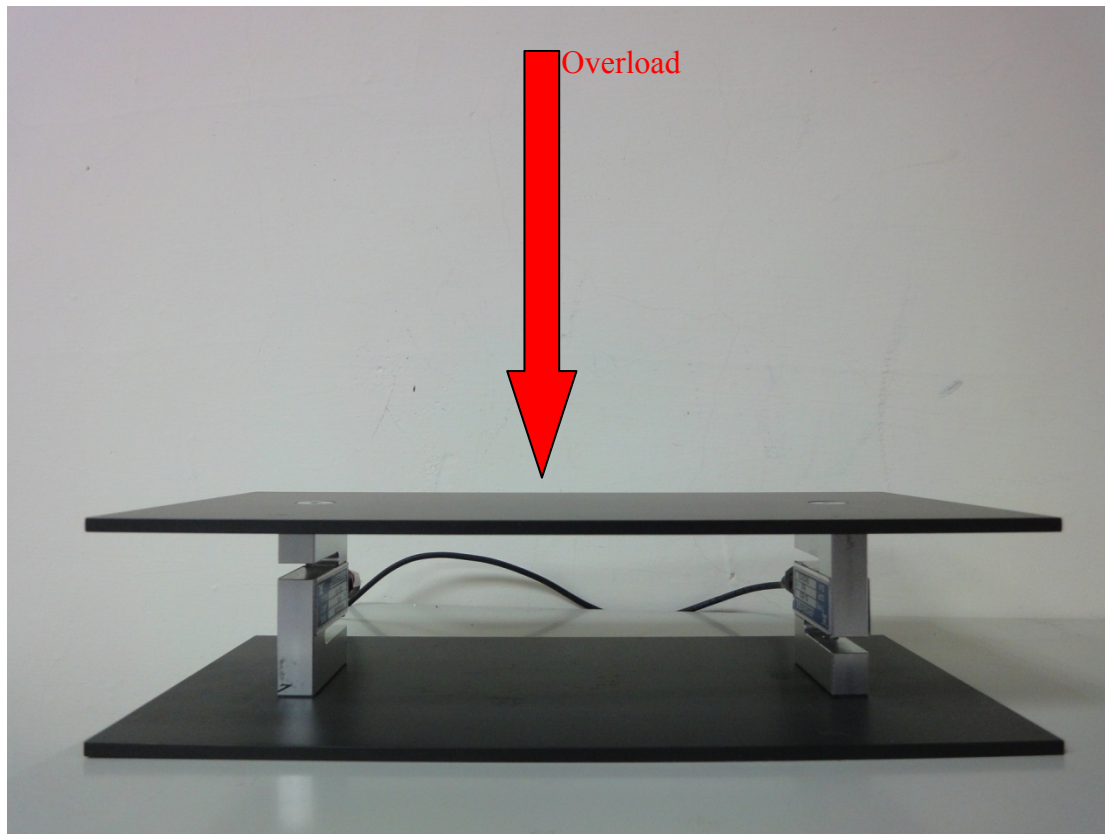


Figure 2.4 The second load cell box that measures total normal load

2.1.4 Static Calibration of Load Cells

In 2.1.3, we designed a load cell box to stabilize load cells and we check that the box does not affect the load cell force-voltage signal in this section. We applied various static weights to the load cells and compared the results with their nominal weight-voltage relationship. The nominal weight-voltage relationship for the normal force component is $6.4 \times 10^{-6} \text{mv}$ per 160gw; for shear force component, it is $8 \times 10^{-6} \text{mv}$ per 160gw. For the three load cell components, we captured the signals under the following loading conditions: (1) putting three 160gw counterpoises one by one on the load cell measuring surface, with a 5-second interval; (2) removing the counterpoise one by one with the same time interval. In order to minimize calibration error, we separated the measuring surface of each load cell into several zones as shown in figure 2.5 and did the same calibration procedure for each zone. Figure 2.6 (a) to (i) shows the adding-weight curve (blue) and reducing-weight curve (red) for the front plate, figure 2.7 (a) to (c) shows the same results of top plate, and figure 2.8 shows the same results of tension plate. Table 2.3 shows the numerical results, the negative signal corresponds to a compression force on the measuring surface.

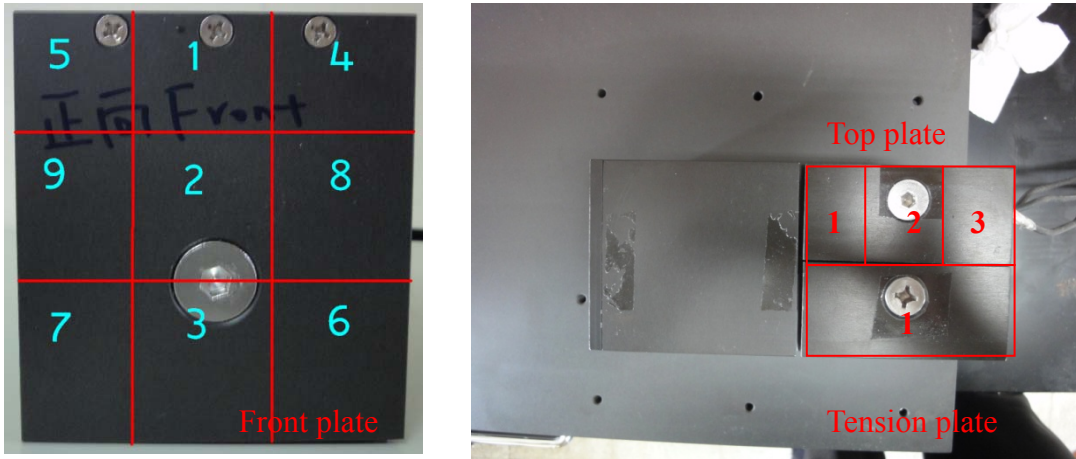
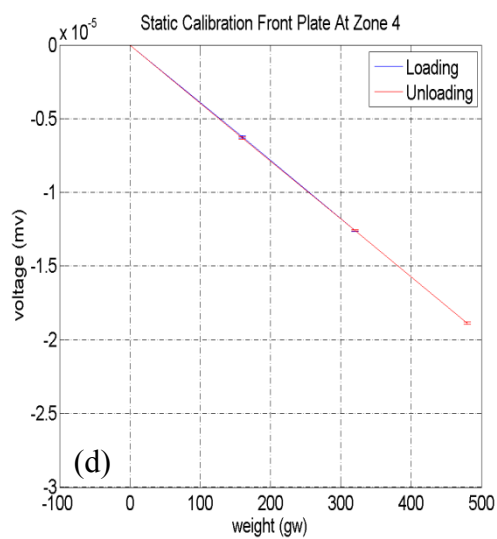
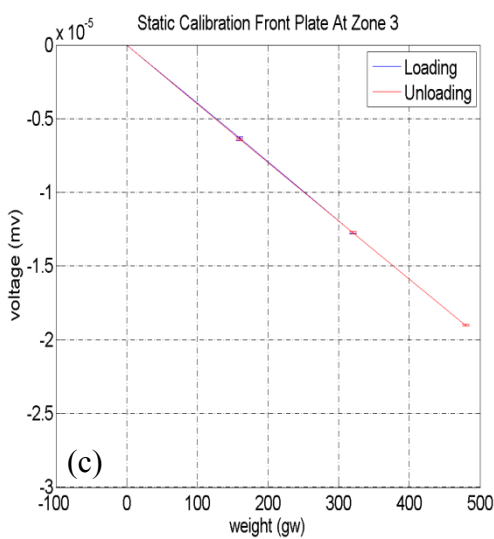
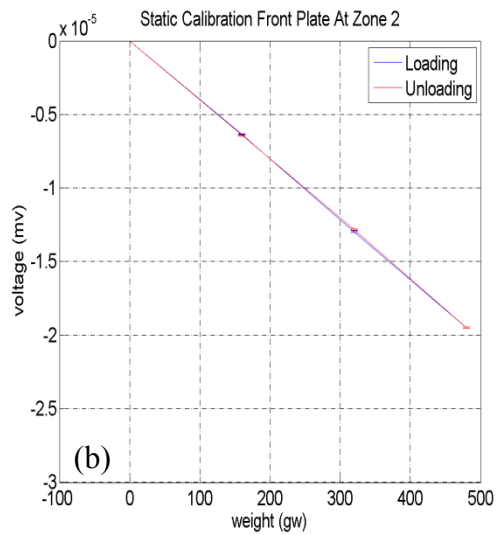
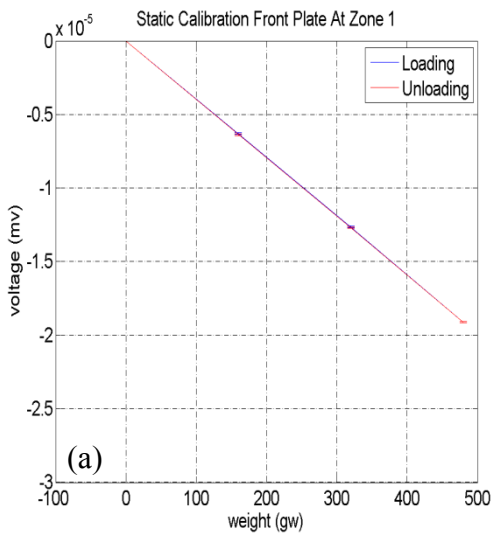


Figure 2.5 Separation zone of each load cell surface.



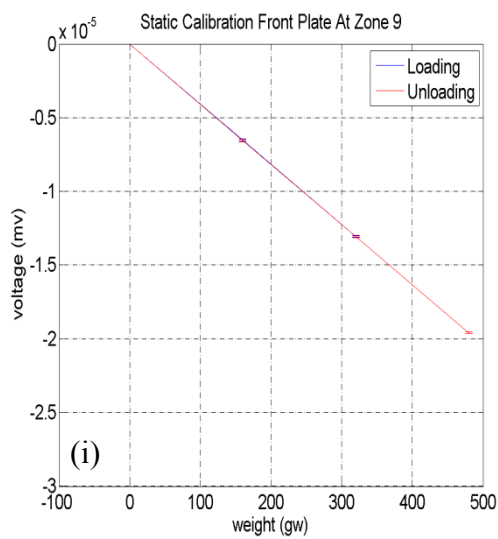
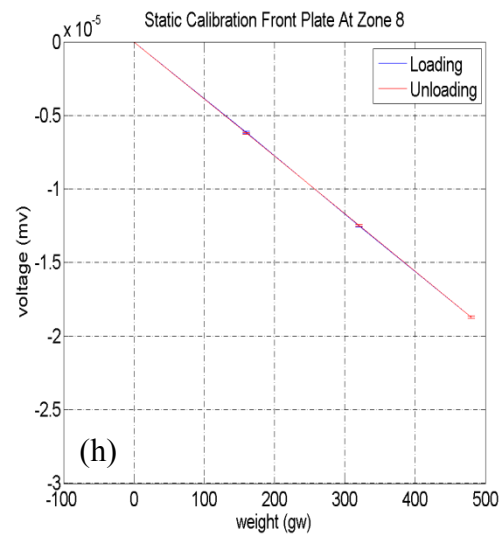
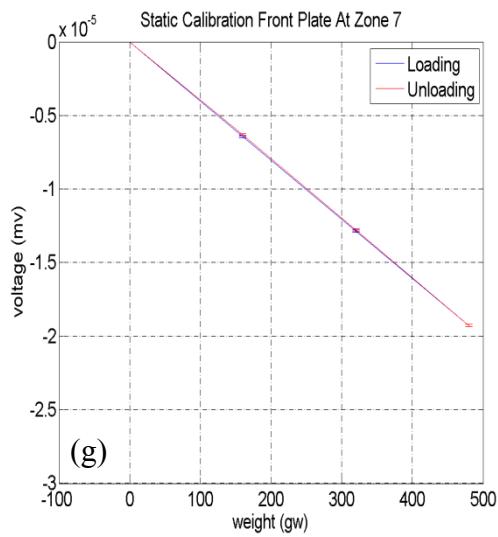
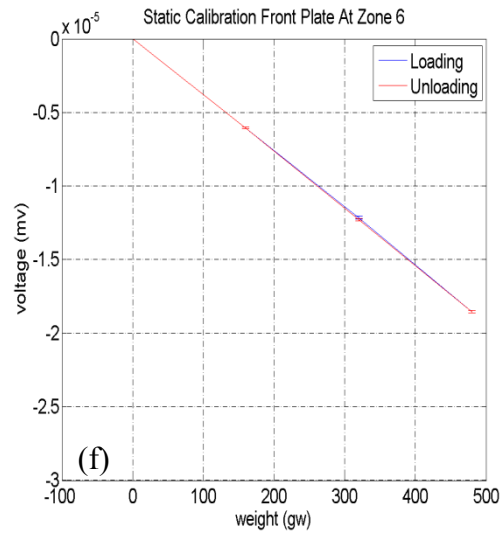
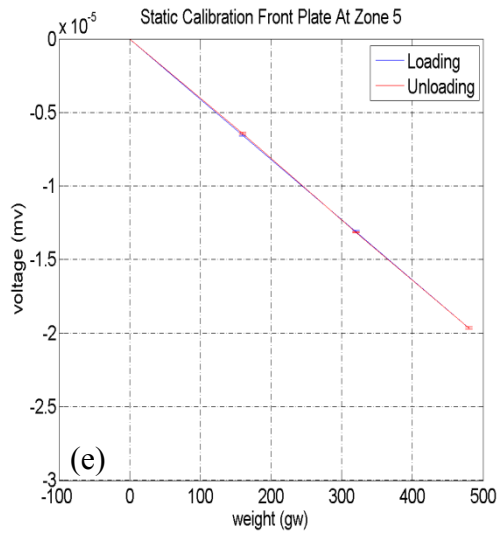


Figure 2.6 Static calibration results of front plate.

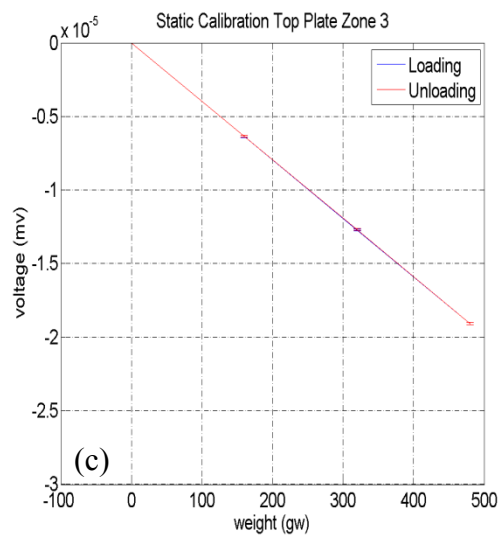
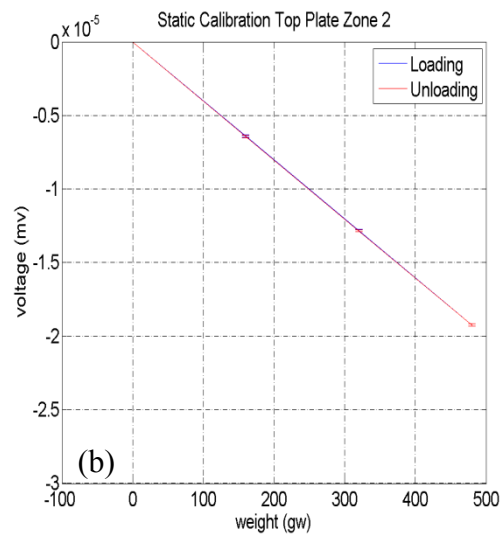
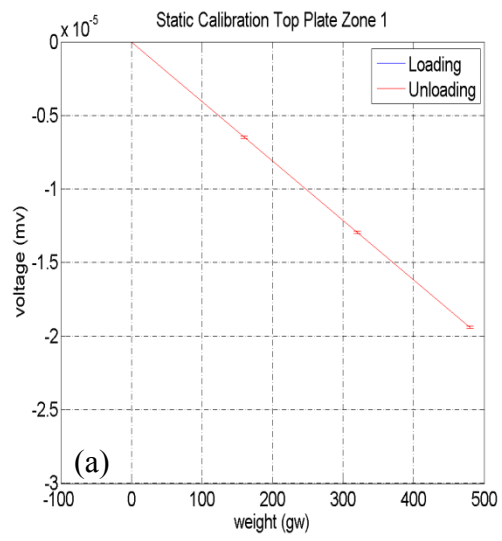


Figure 2.7 Static calibration results of top plate.

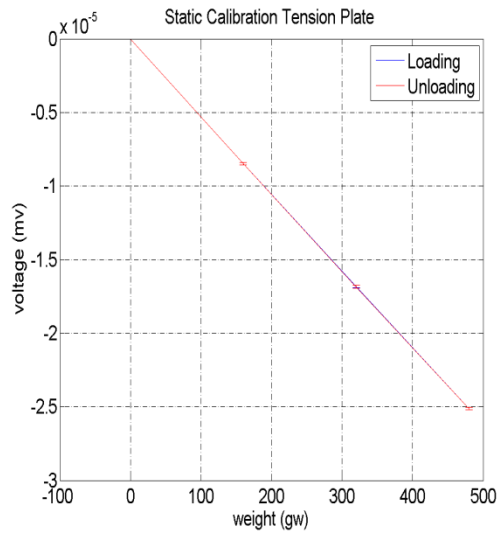


Figure 2.8 Static calibration results of tension plate.

Table 2.3 Results of static calibration.

Zone	Output voltage Mean value ($\times 10^{-6} mv$)	Standard deviation of the mean
Front Plate zone 1	6.3717	0.44%
Front Plate zone 2	6.4907	1.42%
Front Plate zone 3	6.3338	1.03%
Front Plate zone 4	6.2907	1.71%
Front Plate zone 5	6.5521	2.38%
Front Plate zone 6	6.1620	3.72%

Front Plate zone 7	6.4202	0.32%
Front Plate zone 8	6.2410	2.48%
Front Plate zone 9	6.5278	2.00%
Top plate zone 1	6.4919	1.44%
Top plate zone 2	6.4106	0.17%
Top plate zone 3	6.3554	0.70%
Tension plate	8.3831	4.79%

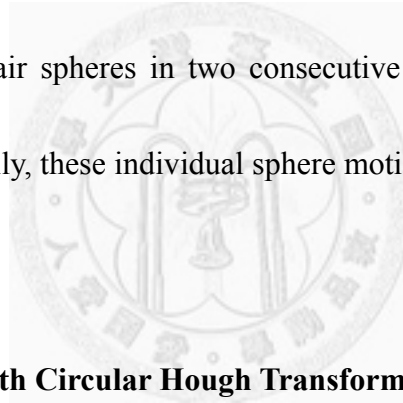
From table 2.3, the standard deviation for all static calibration mean errors are under 5%. Therefore, we may ensure that the load cell box has little influence on its response and we can use nominal weight-voltage relationship for later analysis.

Chapter 3 Image Processing and Load-cell Signal Analysis

In this chapter, the methods we used to analyze the load cell signals and the digital images are introduced.

3.1 Procedures of Image Analysis

We analyzed the digital images by the following methods: (1) we applied Laplace and Gaussian filters to enhance image contrast and then applied *circular Hough transformation* to locate individual sphere center; (2) we used the method of the nearest neighbor to pair spheres in two consecutive images to achieve particle tracking velocimetry. Finally, these individual sphere motions are averaged in space to estimate bulk motion.



3.1.1 Locating spheres with Circular Hough Transformation and its Error

Linear Hough transformation is a sequence of transformation between physical space, parameter space, and accumulator space. Consider a set of points from a line whose equation $y = ax + b$ is desired. If we change from x-y-plane in the physical space to the a-b-plane in the parameter space, it becomes $b = y - ax$ and every point on the line changes to a line on the a-b-plane. All these lines intersect at a point (a , b) in the parameter space and the obtained coefficients determine the slope and the intercept for the original line $y = ax + b$ in the physical space. In the procedures, a set

of points are chosen firstly from the physical space (x-y-plane) and transformed into lines on the parameter space (a-b-plane). The transformation of each x-y-point to a-b-line results in a “voting” process in the accumulator space. Figure 3.1 illustrates the principle of linear Hough transformation.

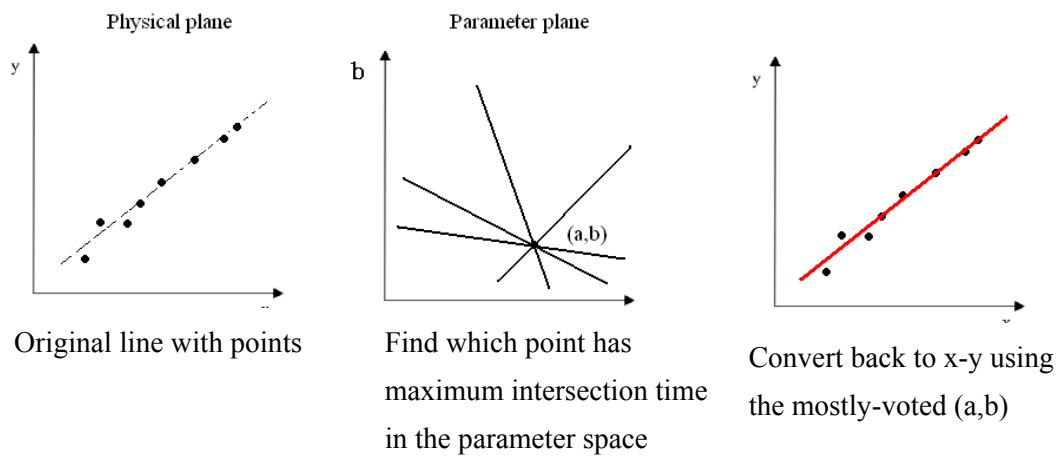


Figure 3.1 Principles of linear Hough transformation.

Later on, Duda and Hart (1975[9]) extended the concept and developed the *circular Hough transformation* method to detect a two-dimensional circular object. The object of interest now has three parameters in its physical space - its center (a,b) and radius (r), which results in a 3D parameter space spanned by a-b-r. Consider a set of point from the circumference of an unknown circle $(x - a)^2 + (y - b)^2 = r^2$. We follow the same concept of linear Hough transformation and transform these points into a cone with its vertex at (x,y) with radius falling in $0 < r < \infty$. These cones should intersect theoretically at a point (a, b, r) which gives the desired parameters for the original circle on the x-y-plane. Figure 3.2 illustrates the principle of circular Hough

transformation.

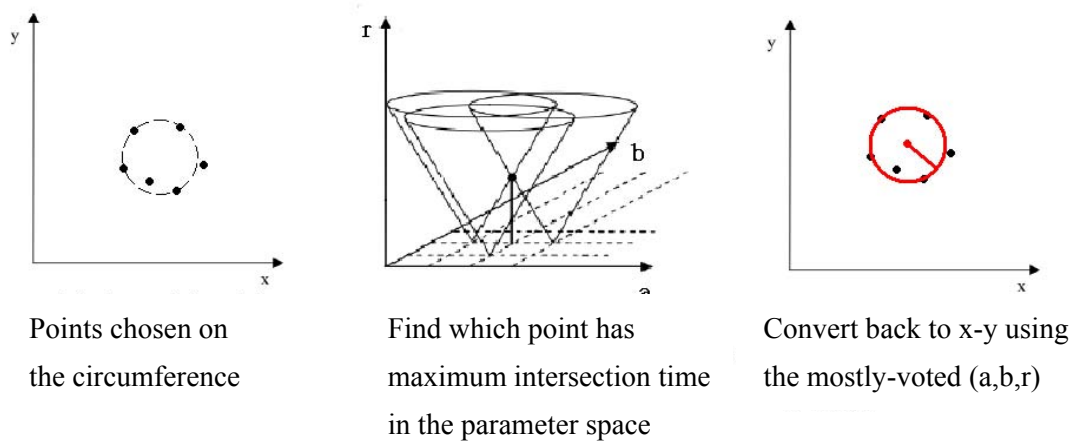


Figure 3.2 Principles of circular Hough transformation.

Form figure 3.2, it is apparent that the success of circular Hough transform crucially relies on if we can effectively select points on the object edge (ie, circumference of the sphere image). Thus, we applied Laplace and Gaussian filters in advance to enhance the gradient at sphere edge to assist better Hough results. These filters can be viewed as numerical operations to adjust the brightness value of each image pixel.

Figure 3.3 shows how these numerical operators behave in the x-y plane and we use the built-in *matlab* commands to condition our digital images.

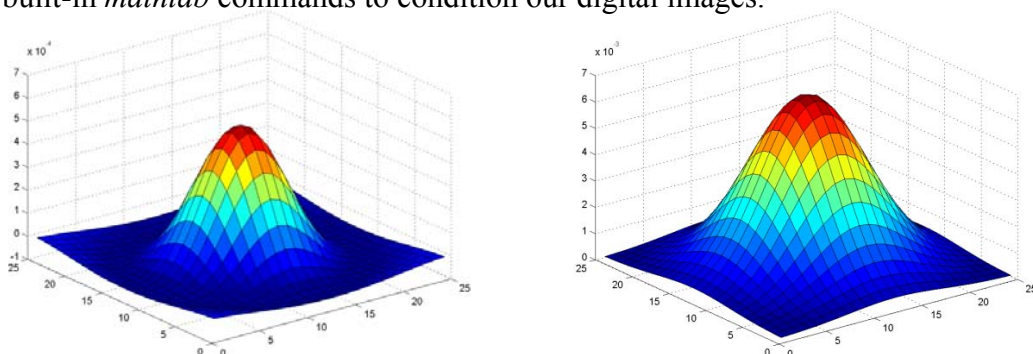


Figure 3.3 The Laplace (left) and Gaussian (right) filter.

The sequence of how an acquired image was processed to give the desired sphere locations at figure 3.4(d)

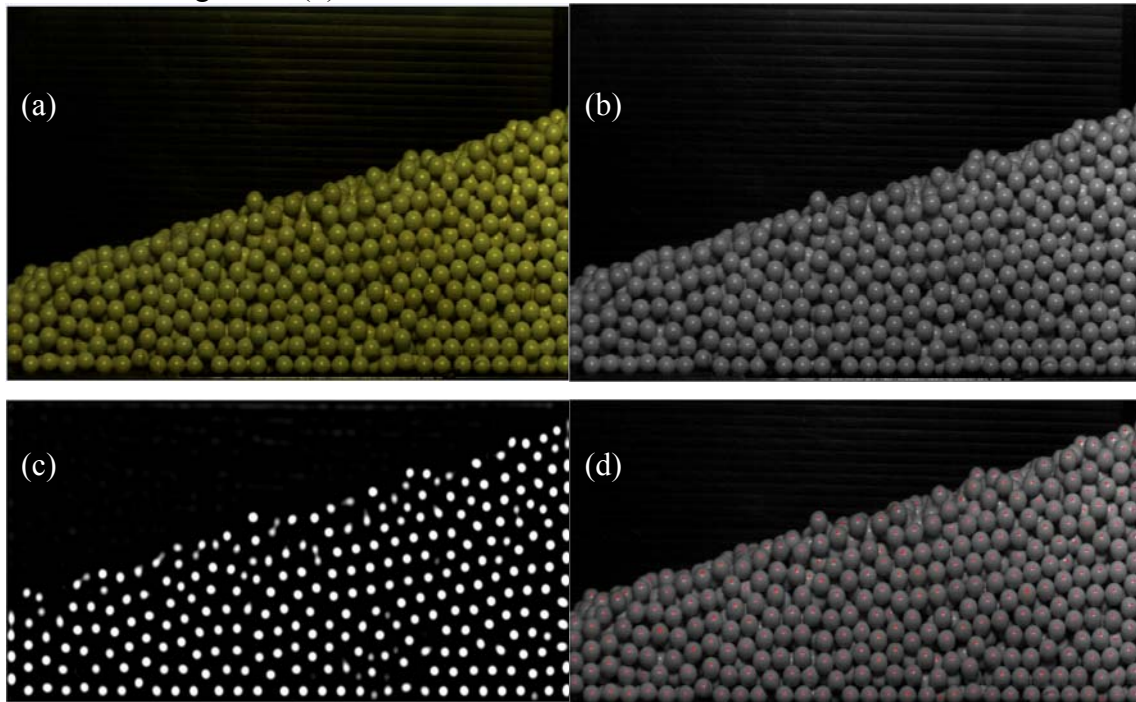


Figure 3.4 (a) original RGB image, (b) gray image, (c) filtered image that strong contract at the circumference, and (d) sphere centers located by circular Hough transformation.

The difference between actual center position and estimated position (red dots in figure 3.4(d)) were calculated in different zones in an image. Three zones were considered: at the right and left edges and in the middle of the image as in figure 3.5. The errors were examined for all the spheres in each zone with the actual position determined manually. Table 3.1 summarizes the average and the deviation of the errors for each zone at different times indicated by the frame number.

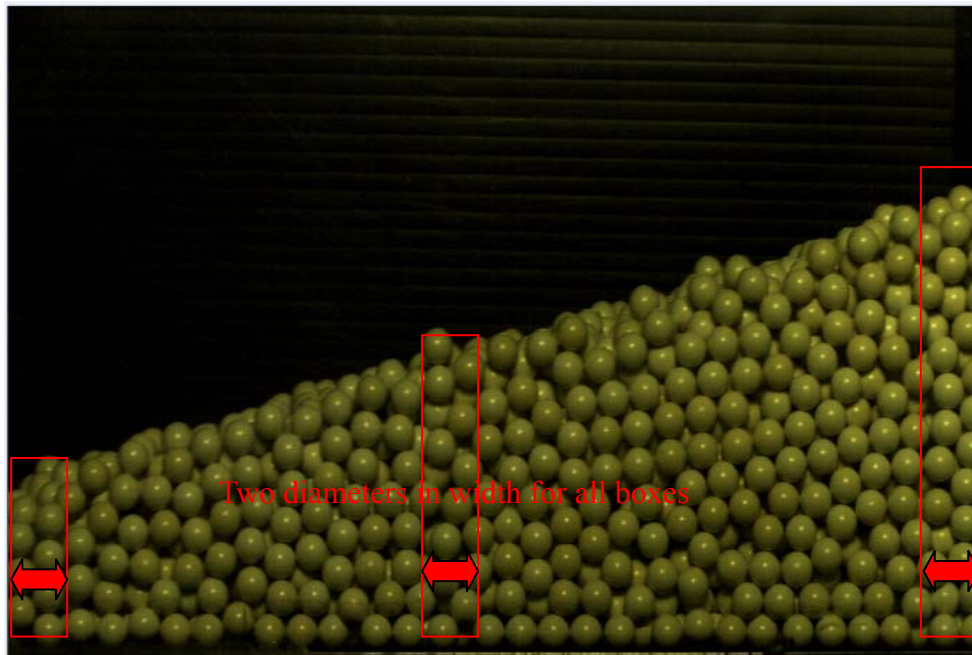


Figure 3.5 Three zones considered in an image to evaluate the error in the sphere location via the circular Hough transformation.

Table 3.1 The average and the standard deviation of the center location error.

Zone Frame number	Left Edge (pixels)	Middle (pixels)	Right Edge (pixels)
600	2.1 ± 1.22	1.02 ± 0.26	1.36 ± 0.25
1200	2.09 ± 1.17	1.58 ± 0.55	1.59 ± 0.65
1800	1.52 ± 0.73	2.11 ± 0.94	1.68 ± 0.77
2400	1.74 ± 0.61	2.36 ± 0.25	2.00 ± 0.79
3000	1.87 ± 0.54	1.24 ± 0.47	1.35 ± 0.23

3600	1.44 ± 0.47	1.76 ± 0.54	2.10 ± 0.60
4200	1.54 ± 1.01	1.21 ± 0.45	1.26 ± 0.27
4800	1.66 ± 0.23	1.96 ± 0.41	1.39 ± 0.18

On these images, one sphere diameter spans 32 pixels, and the error presented in table 3.1 shows that the overall location error fall below 10% of sphere diameter.

3.1.2 Particle Tracking Velocimetry and its Error

We applied the nearest neighbor method to track the same particle in two consecutive images. Figure 3.5 (a) represents the image at an initial time t and figure 3.5(b) represents the image at later time $t+1/\text{FPS}$. For particle P1, we located its center at t and plotted this position on the second image by the red dot. We set a search circle of radius of one diameter, $1D$, as plotted by the dash circle in figure 3.5 (b). In figure 3.5 (b), the dash circle intersected with a few adjacent spheres and we computed the distance between their centers and that of P1 at t . The sphere that possesses the shortest distance was chosen to represent the same particle P1 in the latter image. In the nearest neighbor method, we fail to match the correct particle if its displacement exceeds one particle diameter between two image. Thus, the elapsed time ($1/\text{FPS}$) should be chosen accordingly. In this thesis, the particular 600 FPS was determined by trial-and-error.

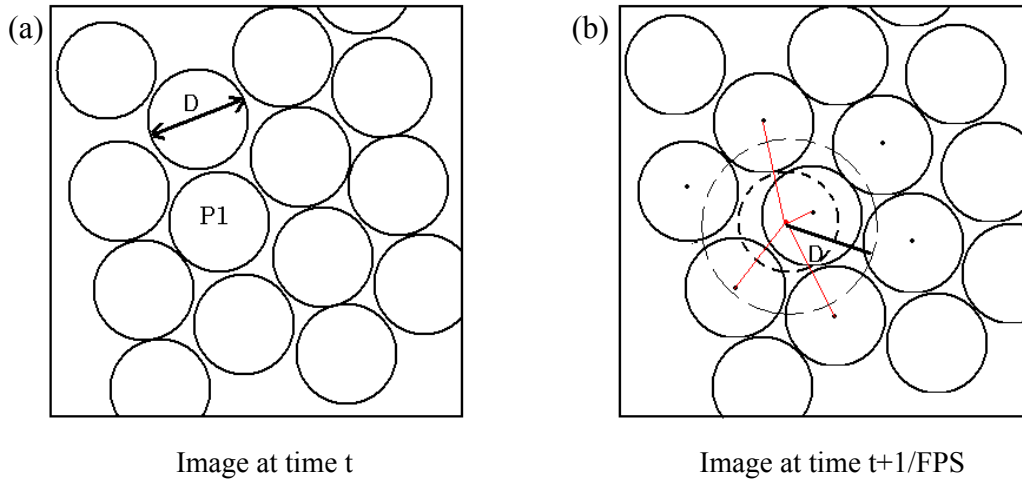


Figure 3.6 Illustration of the concept of the nearest neighbor method to achieve PTV. (a) The location of sphere P1 is firstly determined and its location is marked in the latter image at $t+1/FPS$ by the red dot in (b). A search circle of radius of on diameter is sketched by the dashed line in (b). For this case, two spheres were included by the search circle and the one that gives the shortest distance is chosen to match P1 at earlier time t .

In Table 3.1, we estimated the location error which should be intrinsic for locating at time t and $t+1/FPS$ as $\pm \Delta x(t)$ and $\pm \Delta x(t+1/FPS)$. Thus, we used the largest difference to estimate an upper bound error of our PTV analysis by $(|\Delta x(t)| + |\Delta x(t+1/FPS)|) \times FPS$ and Table 3.2 shows the mean and the standard deviation of *instantaneous* velocity error for different zones at various instant.

Table 3.2 Mean and standard deviation of instantaneous velocity error, an upper bound.

Zone Frame number	Left Edge (cm/s)	Middle (cm/s)	Right Edge (cm/s)
600	3.37±0.98	2.94±0.84	2.88±0.69
1200	4.97±1.04	2.66±1.12	2.55±0.67
1800	3.66±1.11	3.44±1.10	2.63±0.78
2400	3.88±1.09	3.08±1.15	2.73±0.84
3000	3.79±1.45	3.23±1.01	2.99±0.71
3600	4.64±1.24	2.92±0.96	2.85±0.79
4200	4.22±1.15	2.99±0.98	2.92±0.73
4800	4.17±1.25	2.47±0.83	3.22±0.89

3.1.3 Average Scheme for Bulk Properties

In this work, the obtained *individual* sphere information is averaged in space to estimate a bulk property with a weighting by the individual projection area. Two properties that we concern are bulk velocity, \vec{U} , and bulk solid volume fraction, ϕ , based on the concept that the property carried in the solid phase, whether discrete or continuous, should be conserved. We used an averaging box of side-length $a=2D$ in

figure 3.7 that encloses partial or the whole sphere. Each sphere has its velocity, \vec{U}_i , estimated by PTV, and included area (shaded part), A_i . The bulk velocity for this area is then computed

$$\vec{U} = \frac{\sum_i \vec{V}_i \times A_i}{\sum_i A_i}, \quad (3.1)$$

considering total momentum conservation. The solid volume fraction is calculated by

$$\phi = \frac{\sum_i A_i}{a^2}, \quad (3.2)$$

which represents how densely sphere are packed in the averaging box.

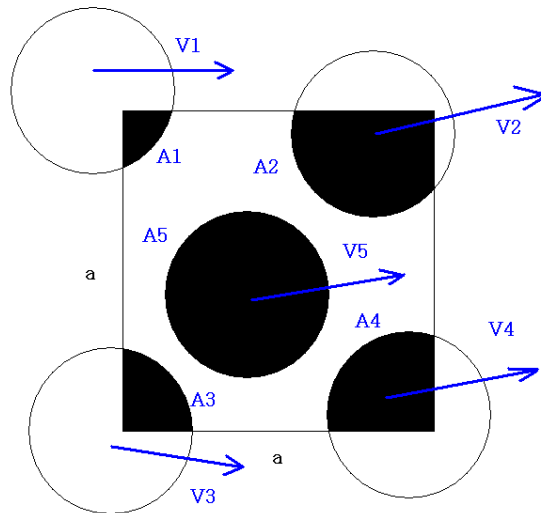


Figure 3.7 Illustration of the area-weighted average scheme.

3.2 Procedures of Load Cell Signal Analysis: Filtering and Conversion

The raw data captured at 1K/sec from load cell can be noisy and was filtered by the built-in inverse *5-order Chebyshev* filter in *Labview* using a low-pass cutoff frequency of *50Hz*. The second filter was then applied to smooth the instantaneous data by using the average of 50 consecutive data prior and post to it. The data obtained after apply these two filters are compared to its raw data in figure 3.8 and the conditioning effect is obvious. Finally, this is voltage temporal data is transferred by the force-voltage relationship validated in section 2.1.4 to obtain the corresponding force magnitudes.

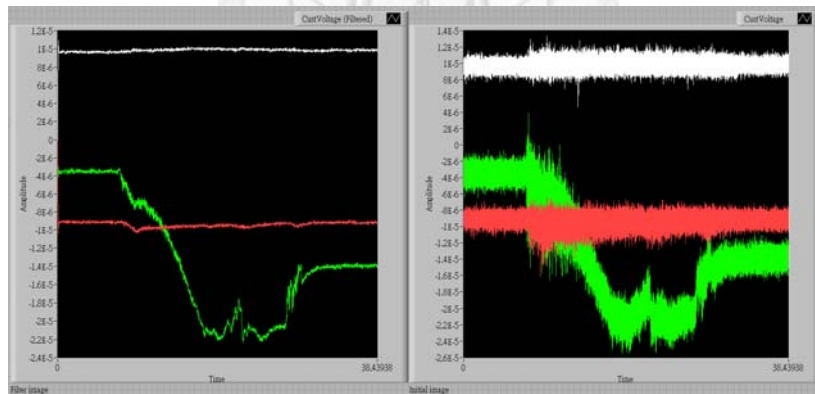


Figure 3.8 Temporal voltage data after (left) and before (right) filtering

Chapter 4 Granular Discharge Analysis

In 2.1.3, we mentioned that we want to measure the impact and the shearing force for a dry steady granular flow which requires steady discharge of granular materials from the reservoir. Thus, it is natural to wonder whether the packing amount and hence of the reservoir geometry spheres can affect the discharge mass flow rate. In the following section, we introduce how we estimated mass flow rate and determined the flow steadiness.

4.1 Experiment Facility and Procedure

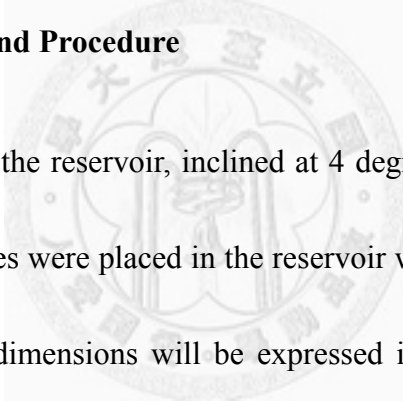
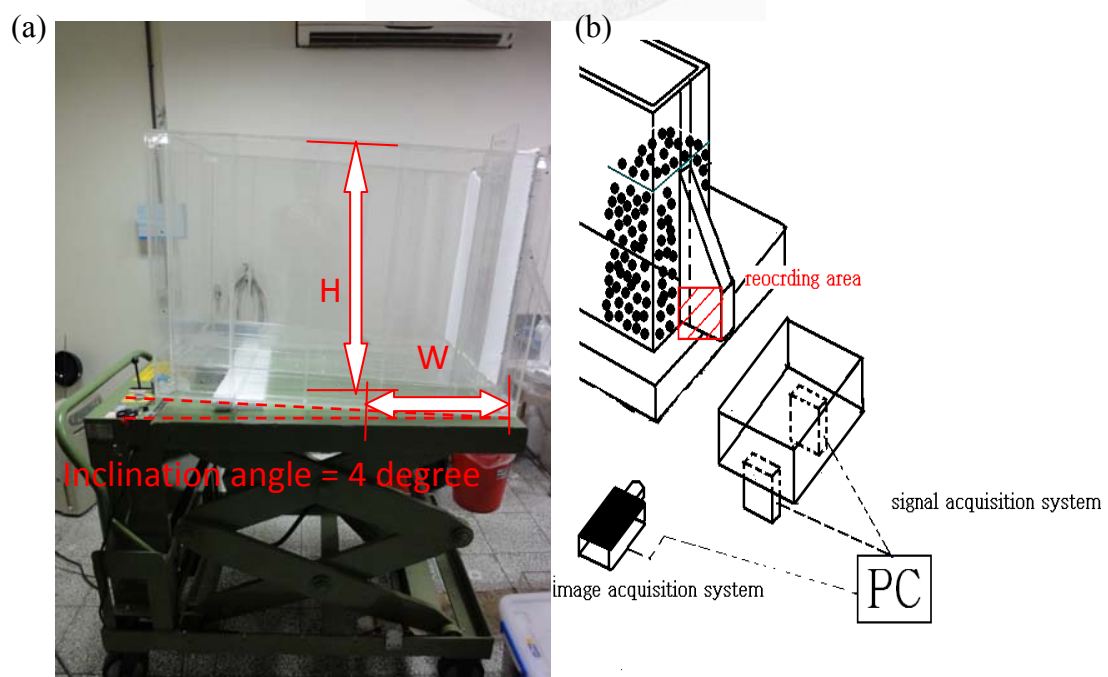


Figure 4.1(a) shows the reservoir, inclined at 4 degrees on a horizontal hoister in which experiment spheres were placed in the reservoir with different width, W , and different height, H . Both dimensions will be expressed in centimeters (cm) here in after. The packed spheres were released from the reservoir gate of constant opening of 10 cm and the released spheres moved along a short connection guide. To estimate the mass flow rate, we put a plastic container to receive the released spheres and the accumulated total weight is monitored by the second load cell module introduced in figure 2.4 with its measuring surface fixed to the center of the container base. The schematic diagram of the experiment facility is shown in figure 4.1(b). The container was placed carefully to ensure that most spheres fell to the container center. At the

side of the connection guide, a high-speed digital camera was employed to record the sphere motion to analyze its flowing properties. To analyze the granular flow motion, we defined the connection guide into three observation lines—next to the reservoir gate, at the guide center, and by the guide exit—with a 7-cm separation, as illustrated in figure 4.1 (c). The aforementioned averaging square box—of side length $2D$ —is laid along each line with a $0.2D$ vertical shift, as shown in figure 4.1(d). The obtained PTV for individual spheres was averaged to estimate the bulk flow properties. Such vertical shift allows us to obtain a depth profile for the bulk velocity and solid volume fraction from which we can also estimate their corresponding depth-averaged values. This image-based flow dynamics will be correlated to the bulk flow steadiness information obtained from the load-cell data.



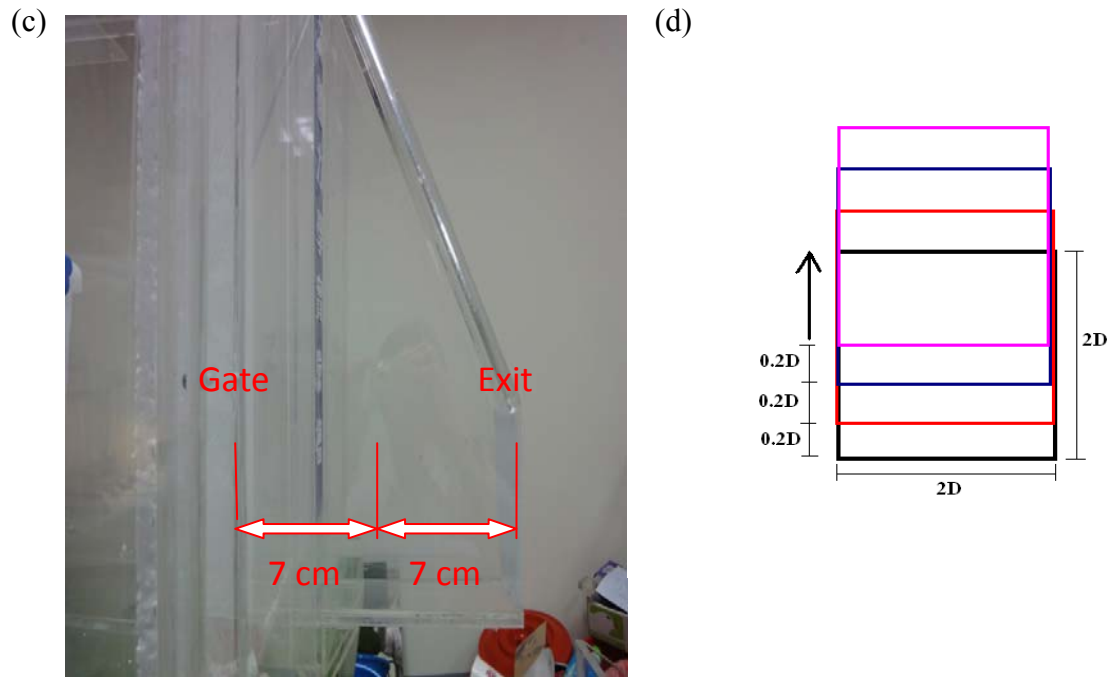


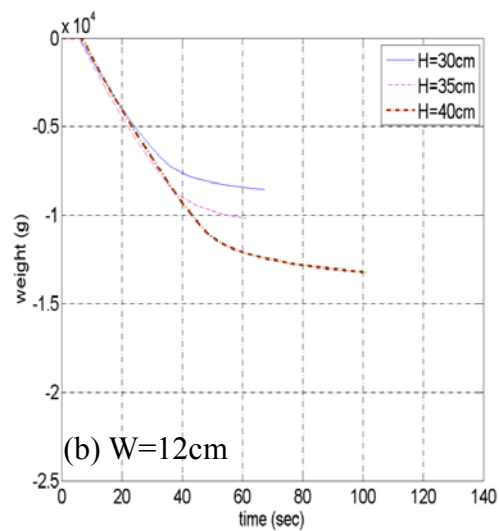
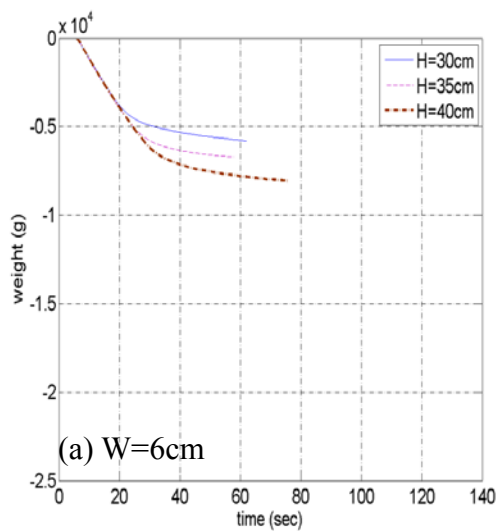
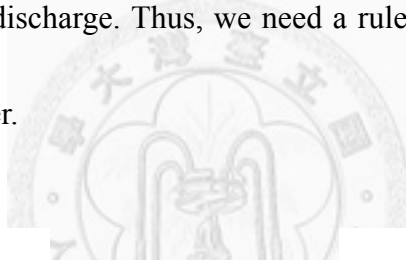
Figure 4.1 (a) reservoir with packing height H and width W specified, (b) schematic diagram of experiment facility, (c) observation line for bulk flow properties defined along the connection guide, (d) averaging box and its vertical shift distance.

4.2 Definition of Steady or Decaying Discharging Region

In this work, a total of different reservoir packing geometries were considered by changing four $W=6,12,18,$ and 24 cm and $H=30, 35,$ and 40 cm. The temporal profiles for the accumulated discharge weight from each packing is shown in figure 4.2. Figures 4.2 (a)-(d) compare profiles from different H for a specific W and figures (e)-(h) are for different W under the same H . Each curve is the average of three experiments. Two common features are observed: (1) every curve has a linear segment followed by a non-linear segment of decaying magnitudes as time progressed; (2) addition of W or H obviously extends the linear segment. Further, for packing with

$H < 30\text{cm}$, the liner segment is especially short as shown in Fig 4.2(e) and hence all the following analyses focus on the cases with packing height over 30cm.

The linear segment clearly results from steady discharge from the reservoir and its slope should correspond to the overall mass flow rate. Therefore, we used the linear segment to identify a *steady discharge* and the non-linear segment is referred to a bulk in *decaying discharge*. We then hoped to use the moment when a discharge changes from linear to non-linear temporal profile to define a *deviation time* to signal the termination of steady discharge. Thus, we need a rule to determine the deviation time in a systematic manner.



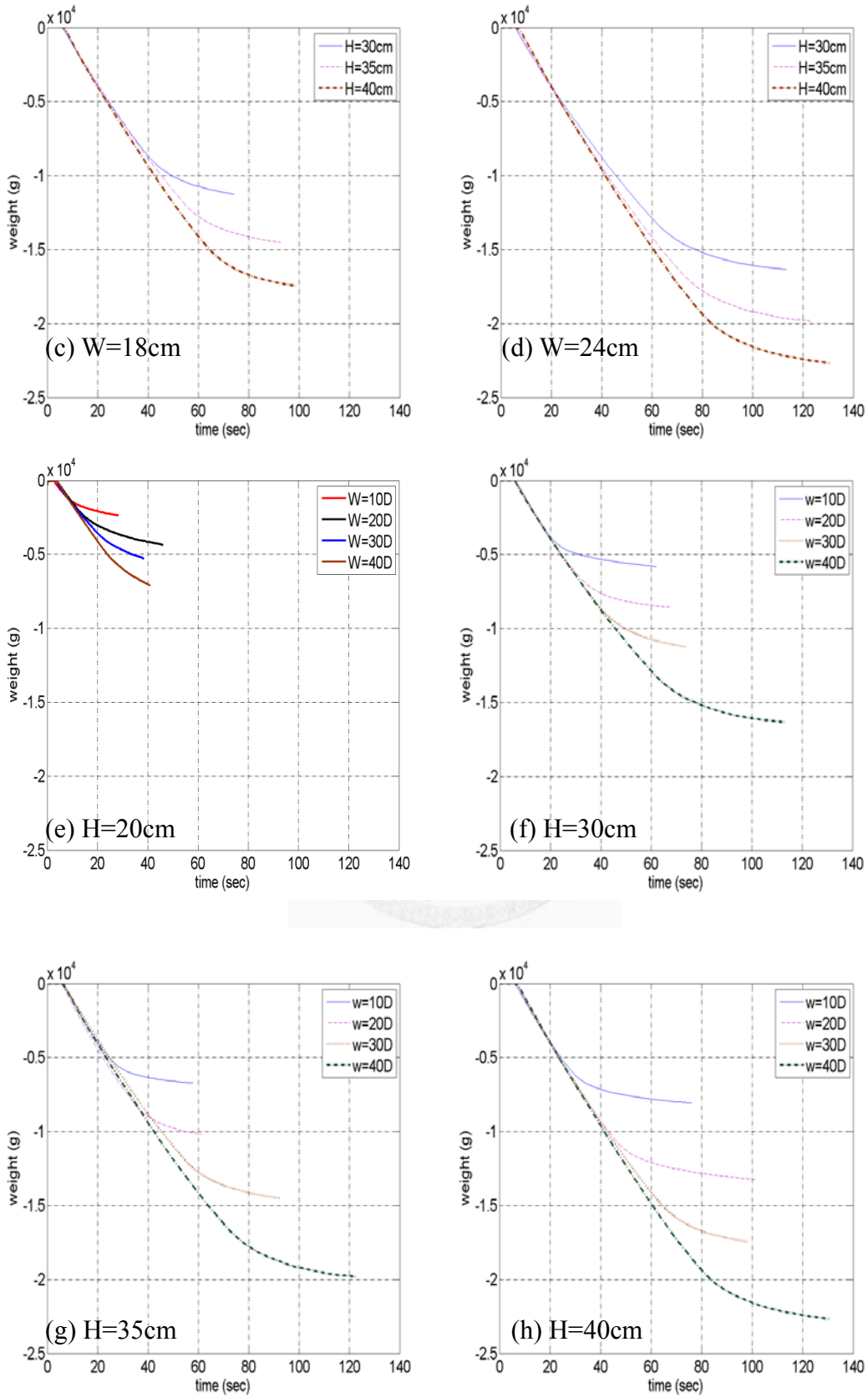


Figure 4.2 The temporal profiles for the accumulated discharge weight for various reservoir packing: (a)-(d) varying W , (e)-(f) varying H .

4.2.1 Deviation Time and Fitting Rules

The following analysis was conducted to determine the deviation time for a particular reservoir packing geometry. We used the *goodness of linearity* for a specific duration of the load-cell data to determine when non-linear deviation is no longer negligible. For this analysis, we chose the time when 5% of the total packed granular mass had accumulated in the container as the starting point. The reason of why we did not start from the beginning was that when spheres fell in empty container, frequent impacts and rebounds from the container base and sidewalls resulted in random noises and ripples on the signal. Only when sufficient spheres had piled in the container that these unwanted signals disappeared. From the time of 5% total weight, we identified the moments when 15%, 25%, 35%, 45%, and 55% of total weight had piled in container as the fitting end points, giving five fitting intervals. A line was then fitted to the data falling in each interval by the least square method; that is, the temporal evolution data of 5%~15% total weight was fitted to give one slope and similarly for the data in 5%~25%, 5%~35%,.....,and etc. Such idea of segmental fitting is illustrated in figure 4.3 using the discharge from a reservoir packing of $W=18\text{cm}$ and $H=40\text{cm}$. To determine which section gives the best fit to a linear profile, we used the so-called “*R-square*” statistical parameter. This parameter, R_s , measures how

successful the fit is by the ratio of the sum of squares of the regression (SSR) and the total sum of squares (SST) which two quantities are

$$SSR = \sum_{i=1}^n w_i (\hat{y}(x) - \bar{y})^2 \quad \text{and} \quad (4.1(a))$$

$$SST = \sum_{i=1}^n w_i (y_i - \bar{y})^2, \quad \text{giving} \quad (4.1(b))$$

$$R_s = SSR / SST. \quad (4.1(c))$$

In these expressions, n indicates the total number of data points, w_i is some user-specified weighting of every chosen data point and was set to unity, \bar{y} is the average of the chosen data points, $\hat{y}(x)$ represents the data predicted by the fitted line, and finally y_i represents the true value at each chosen moment. This parameter, R_s , falls between 0 and 1 with unity indicating perfectly linear fit and zero signaling a failed linear fit. Thus, the segmental linear fit that gave the largest R_s was chosen as the best fit whose slope gives an estimation to the bulk mass discharge rate.

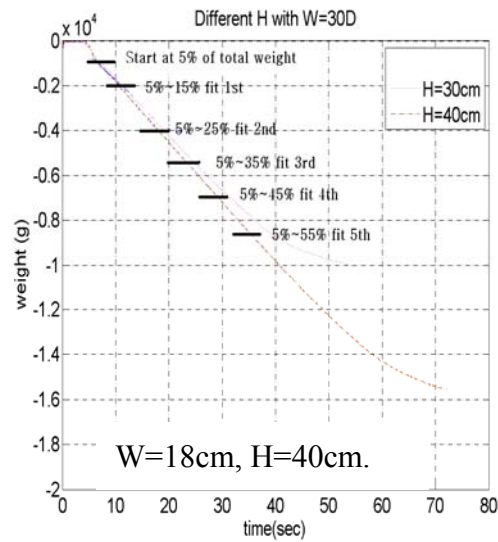


Figure 4.3 Illustration of the intervals considered in segment fitting.

After the best fit of a discharge curve has been determined and denoted as $\hat{w} = ax + b$, the degree of deviation of a raw data (t, w) from the line was computed as $D(t) = (\hat{w}(t) - w) / w$, The moment (t) when this value grows over 0.05 was determined as the desired *deviation time* of the onset. The results obtained from various packing geometries using the five designated intervals (with 5-15% to 5-55% total weights) are compared in figure 4.3(a)-(e) with increased intervals. Further, that correspond to the best fit is shown in figure 4.3(f).

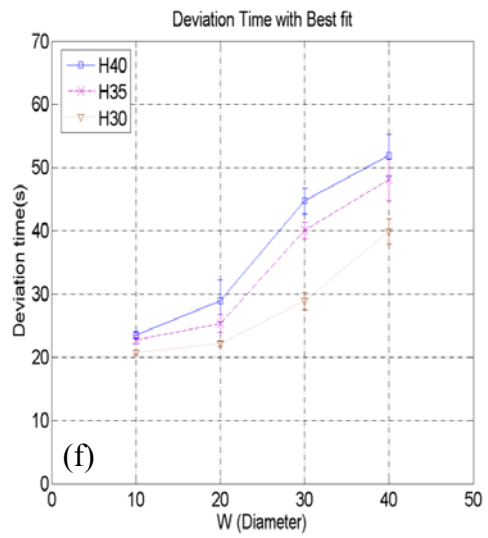
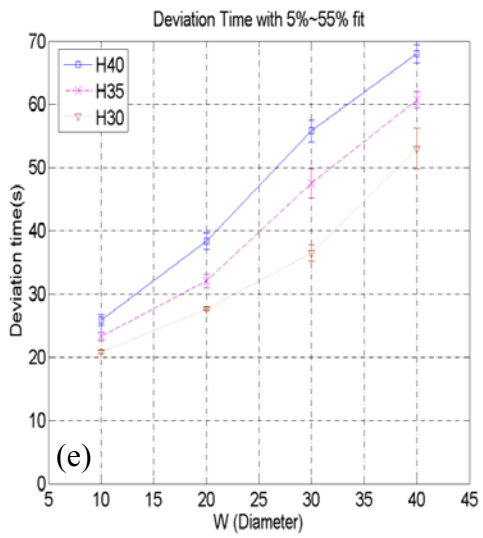
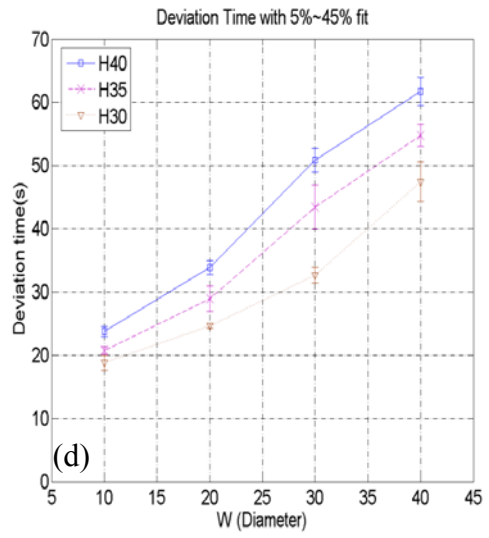
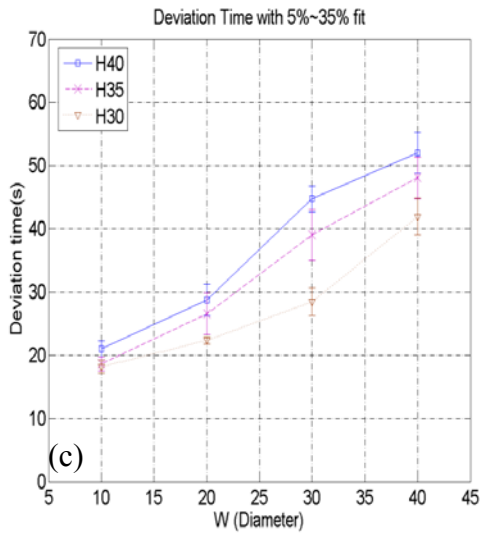
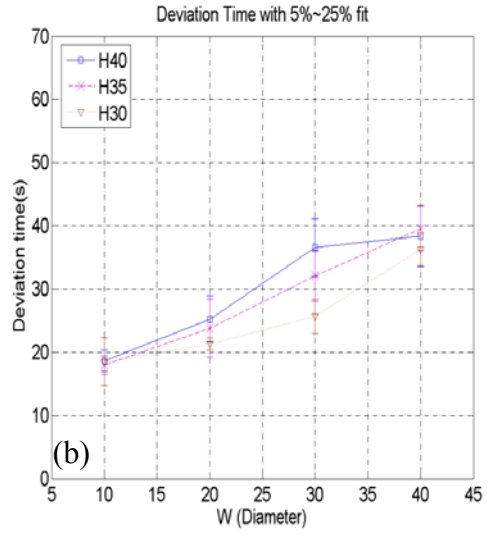
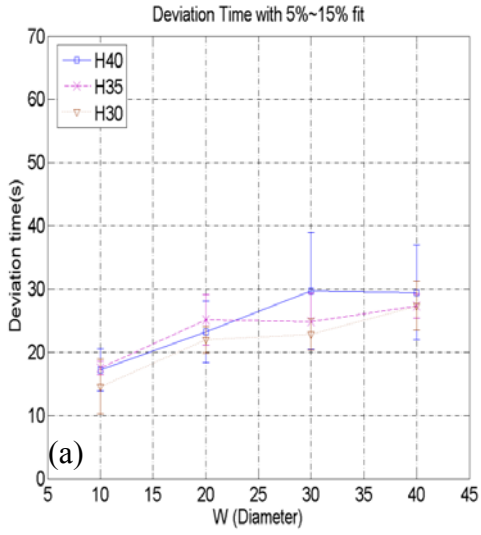


Figure 4.3 The deviation time for the onset of unsteady discharge for various reservoir packing geometry using different segmental fittings, (a)-(e). The data obtained from the best fit is compared in (f).

From figure 4.3(a)-(f), we can see that the deviation time increases monotonically with the reservoir packing size, especially with the packing width W , which phenomenon agrees to our intuition. Further, the degree of increment with W seems to enlarge when the fitting interval is increased implicitly suggesting minute but continuous discharge decay over time from the seemingly linear profile. In other words, if a perfect linear line was detected over the longest fitted range (5~55% total weight), the deviation time should not change with the fitting interval. However, a cross-comparison for the smallest packing with $W=10D$ and $H=30\text{cm}$ reveals slight increase of the deviation time from 15 seconds in figure 4.3(a) to 20 seconds in figure 4.3(e) when the fitting segment is increased. This phenomenon is also observed for flows from other reservoir packing geometries which implies slightly degraded decaying of mass flow rate throughout the reservoir discharge. The trend that the deviation time increases with the reservoir packing is also observed in figure 4.3 (f) when the best linear fit is employed as the reference. This figure guided us for when to start recording the 'quasi-steady' flow motion by a lateral high speed digital camera.

4.2.2 Temporal profiles of decaying discharge

In addition to determine the deviation time, we also wonder if the decaying discharge profiles have any specific pattern. Thus, we use the best-fitted line, $\hat{w} = at + b$ to extrapolate the difference of an experimental data from it as $\Delta W(t) = |w - \hat{w}|$. Nearly zero value is obtained in the steady discharge segment but $\Delta W(t)$ grows in time (with t) and we baldly assume an exponential growth of this deviation as

$$\Delta W(t) = e^{At^B} . \quad (4.2(a))$$

To extrapolate the two constant components, A and B, we transform equation (4.2(a)) into logarithmic scale twice giving firstly $\log(\Delta W) = At^B$ and finally

$$\log \log(\Delta W) = \log A + B \log t . \quad (4.2(b))$$

Thus, taking double log of (ΔW) and examining it with respect to log-scale time, a linear correlation would be revealed if the speculated growth rate in equation (4.2(a)) does occur in our system. A typical result is shown in figure 4.4 for discharge from a packing with $W=6\text{cm}$ and $H=35\text{cm}$. The fluctuating profiles between $1.8 < \ln t < 3$ result from nearly zero deviation in the linear segment and conforming profiles for decaying discharge from repeated experiments is observed after $\ln t > 3.12$ which is the natural log value of the deviation time. It is this later decaying discharge segment

that we examine in the following. For all the reservoir packing considered in this work, its temporal profile of (ΔW) is firstly examined in the form of double-log (ΔW) versus $\ln t$ in the left subplot of figure 4.4 (a)-(l). The deviation time determined from the best linear fit was employed to isolate the decaying discharge segment in the right subplot for each packing.

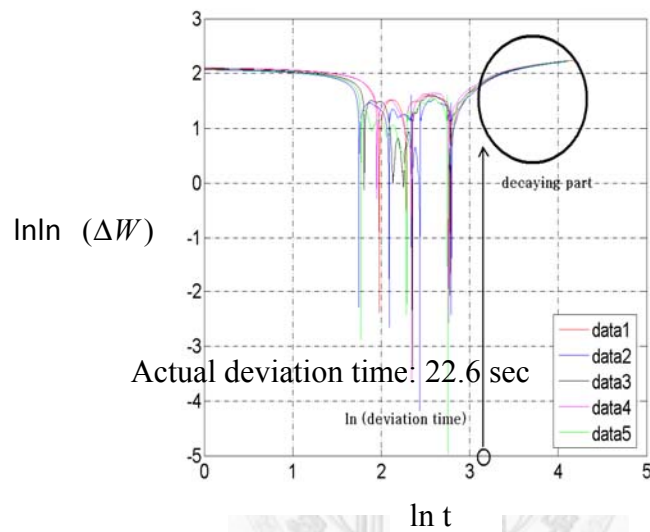
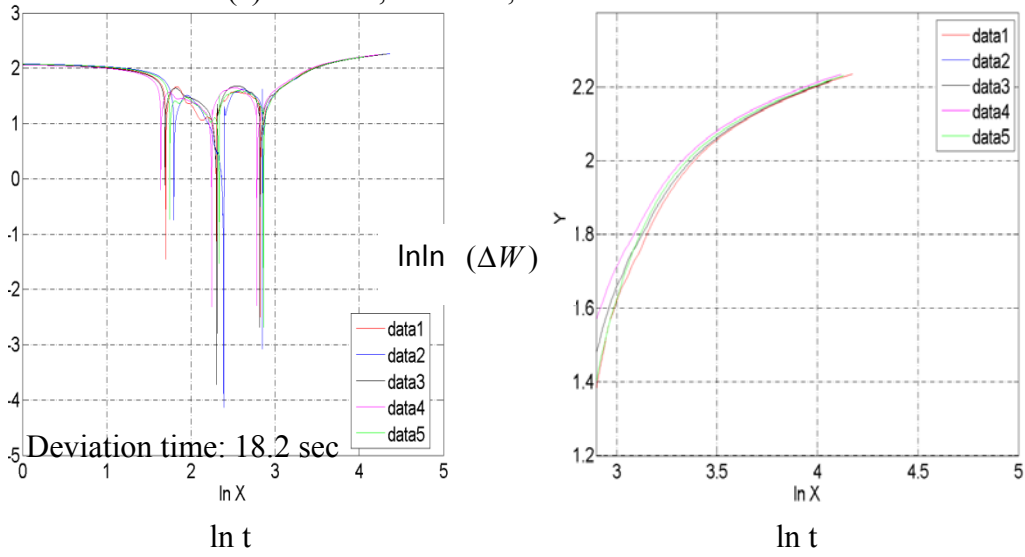
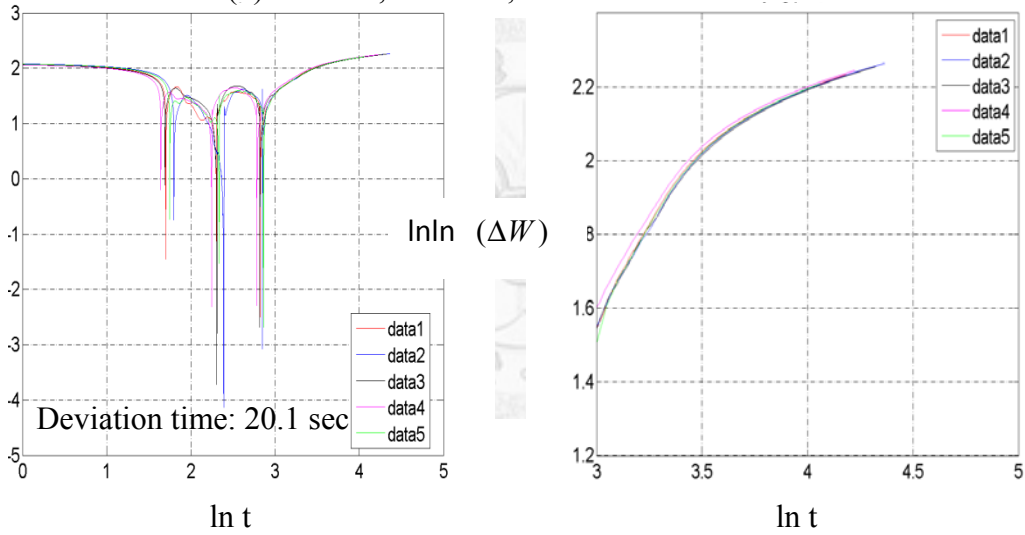


Figure 4.4 Double-log of the weight difference ($\Delta W(t) = |w - \hat{w}|$) versus logarithmic scale time for discharge from the packing with $W=6\text{cm}$ and $H=35\text{cm}$.

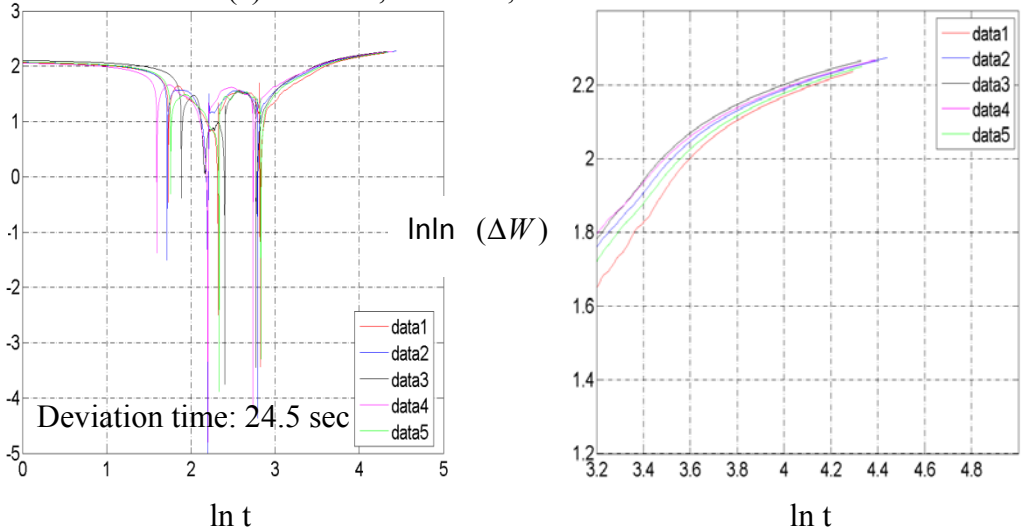
(a) $W=6\text{cm}$, $H=30\text{cm}$; best fit in 5%~55%



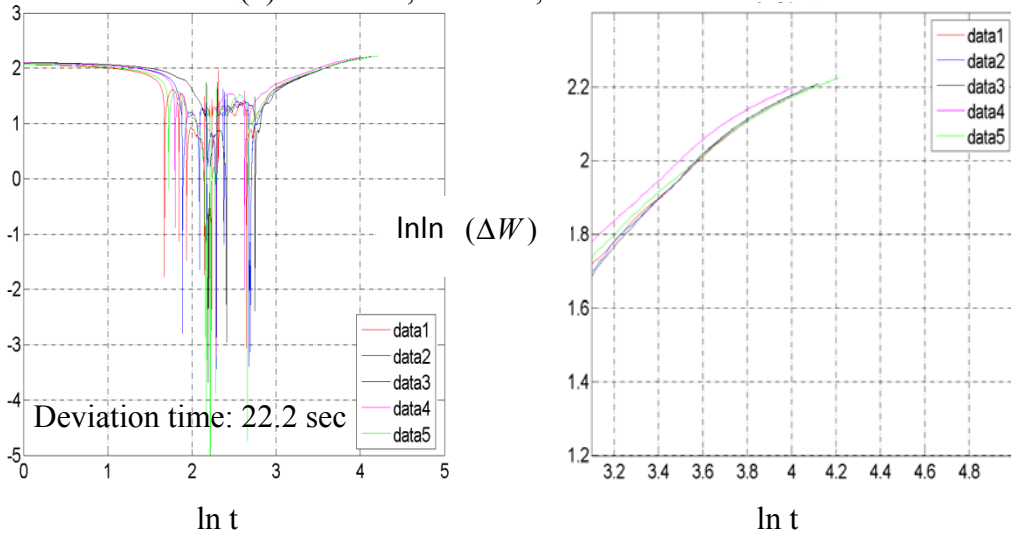
(b) $W=6\text{cm}$, $H=35\text{cm}$; best fit in 5%~55%



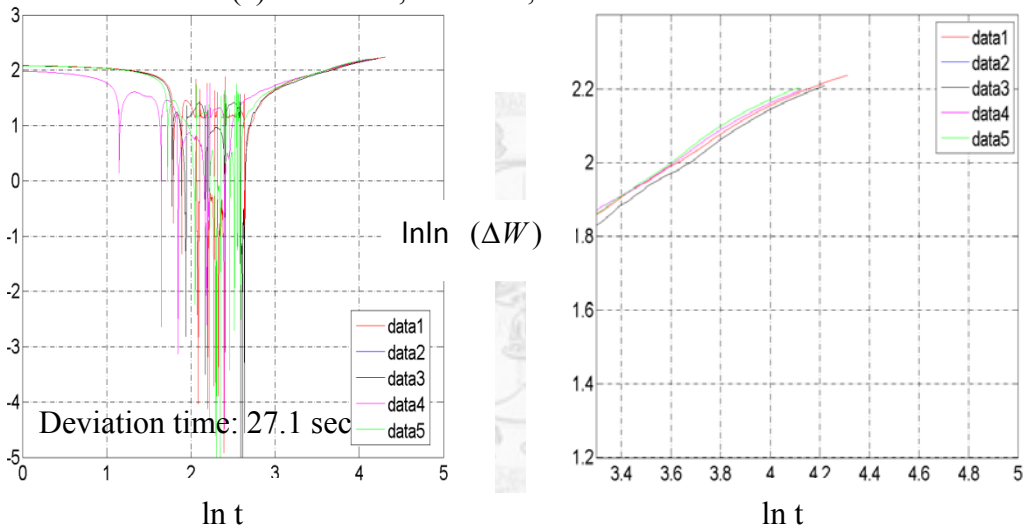
(c) $W=6\text{cm}$, $H=40\text{cm}$; best fit in 5%~45%



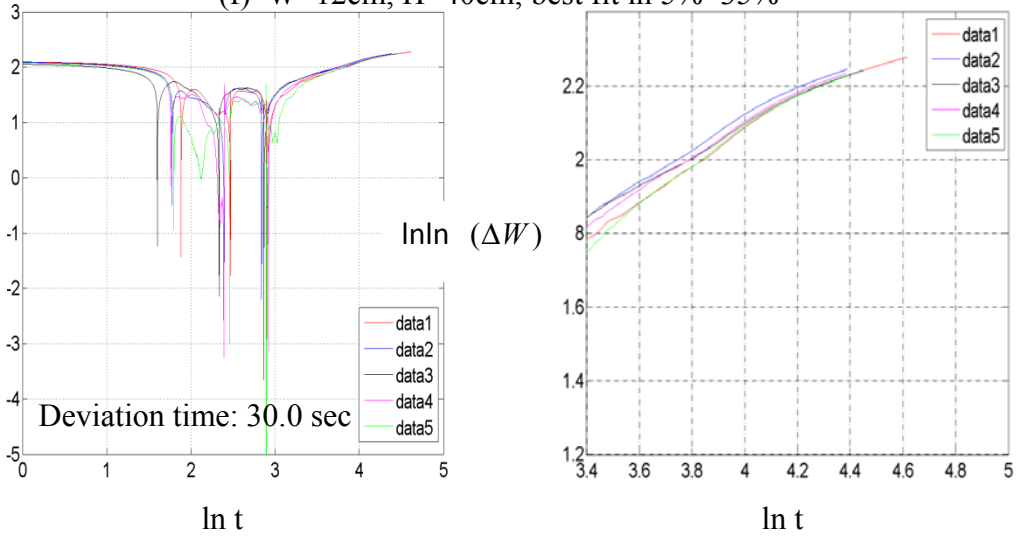
(d) $W=12\text{cm}$, $H=30\text{cm}$; best fit in 5%~35%



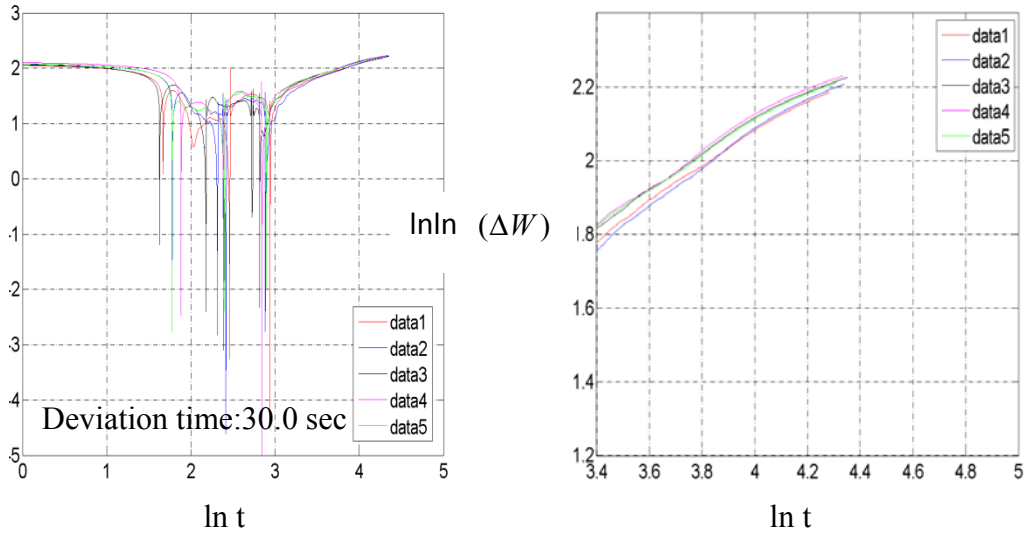
(e) $W=12\text{cm}$, $H=35\text{cm}$; best fit in 5%~35%



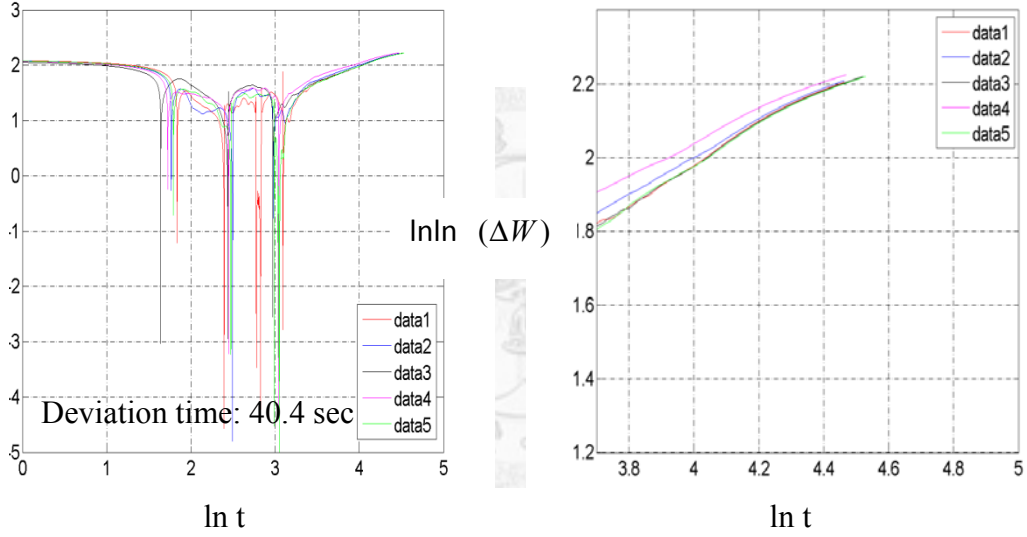
(f) $W=12\text{cm}$, $H=40\text{cm}$; best fit in 5%~35%



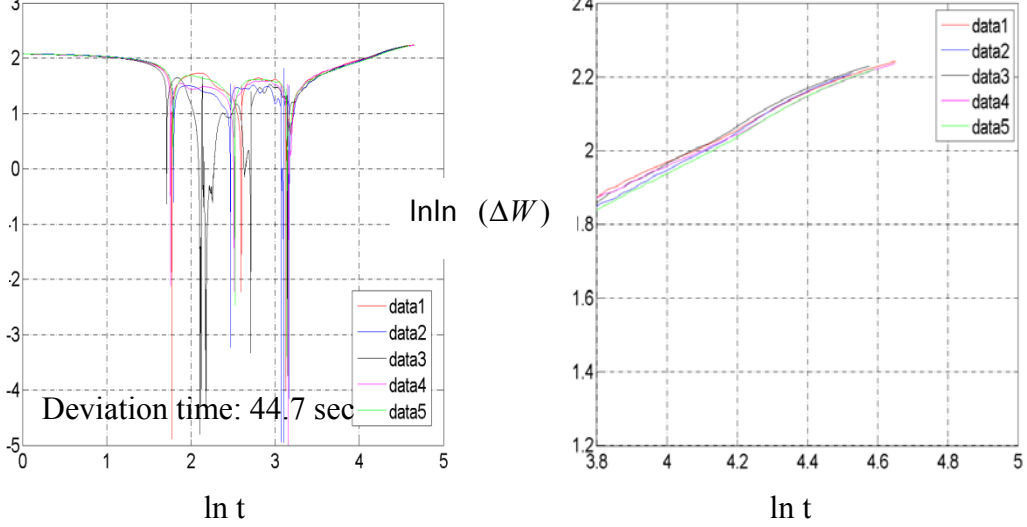
(g) W=18cm, H=30cm; best fit in 5%~35%



(h) W=18cm, H=35cm; best fit in 5%~35%



(i) W=18cm, H=40cm; best fit in 5%~35%



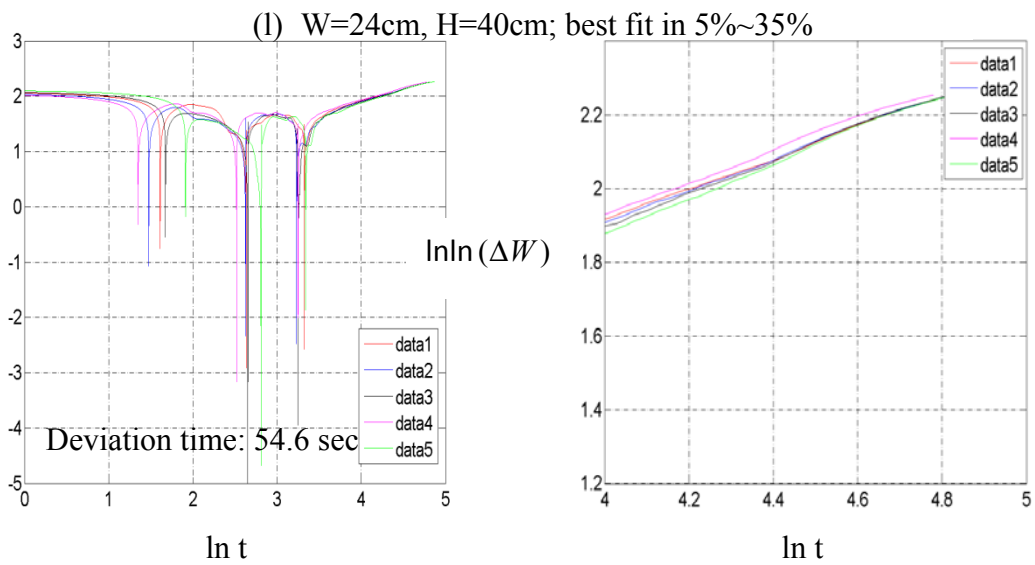
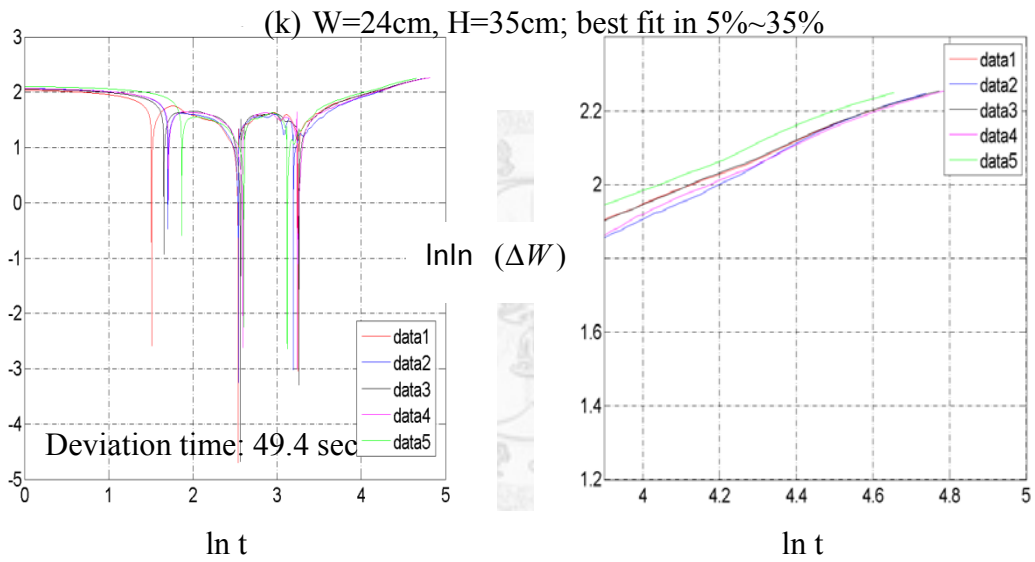
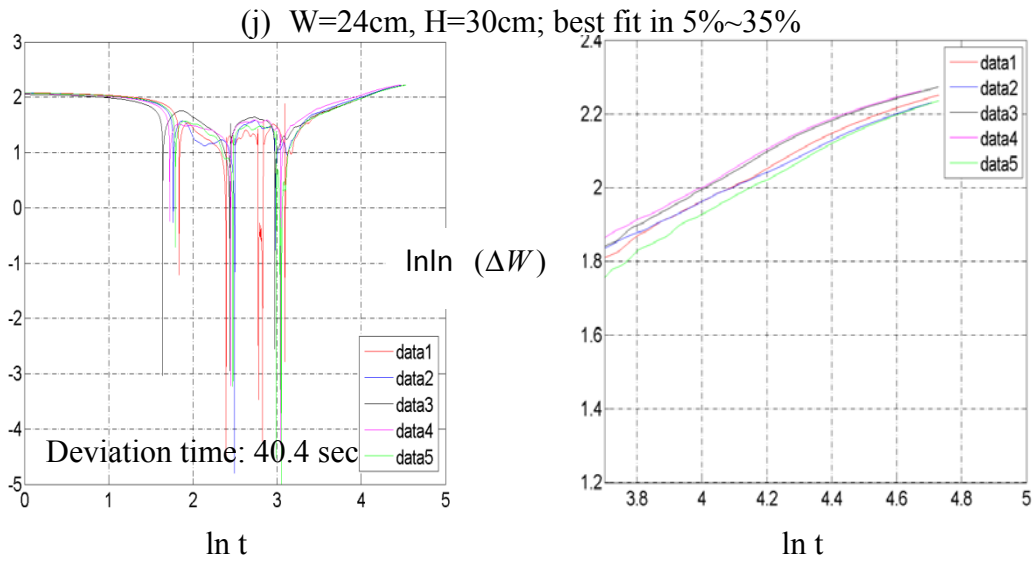


Figure 4.4 Double log of the weight difference, ΔW , versus log-scale time.

For the packing of $W=12$ cm, 18 cm, and 2 cm, a linear trend between double-log ΔW and $\ln t$ is clearly revealed as the example case shown in figure 4.5 (a). A least-square fitting gives the exponent constants with high R-square value above 0.9. However, discharges from a narrow packing with $W=6$ cm but varying $H=30$ cm, 35 cm, 40 cm all give nonlinear evolution profile for the decaying discharge like figure 4.5 (b). The early evolution profiles from repeated experiments give scattered data but nicely conformed linear tails are revealed as boxed and denoted by Part B for these decaying discharge profiles. We thus use liner tails to estimate the corresponding A and B.

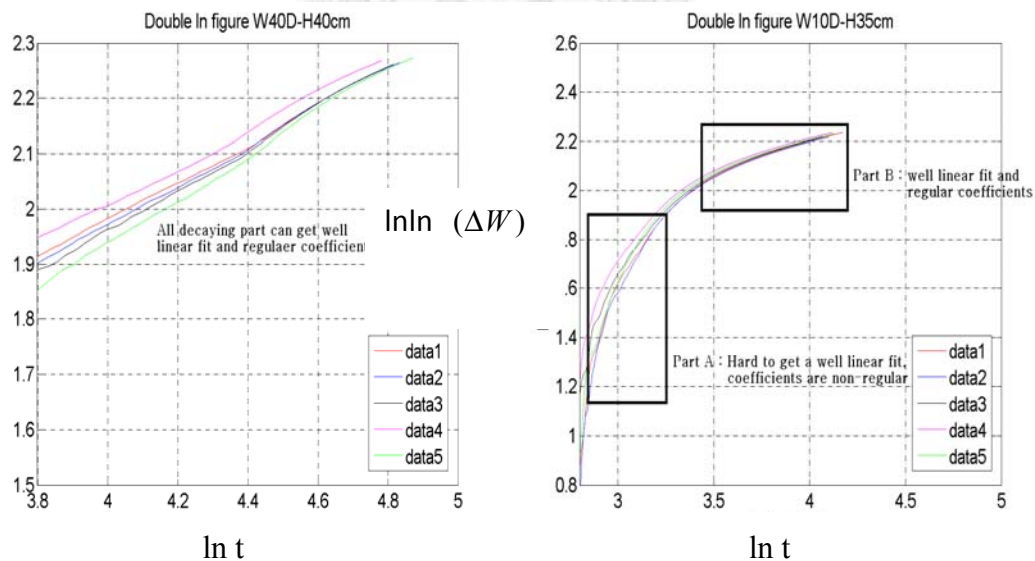
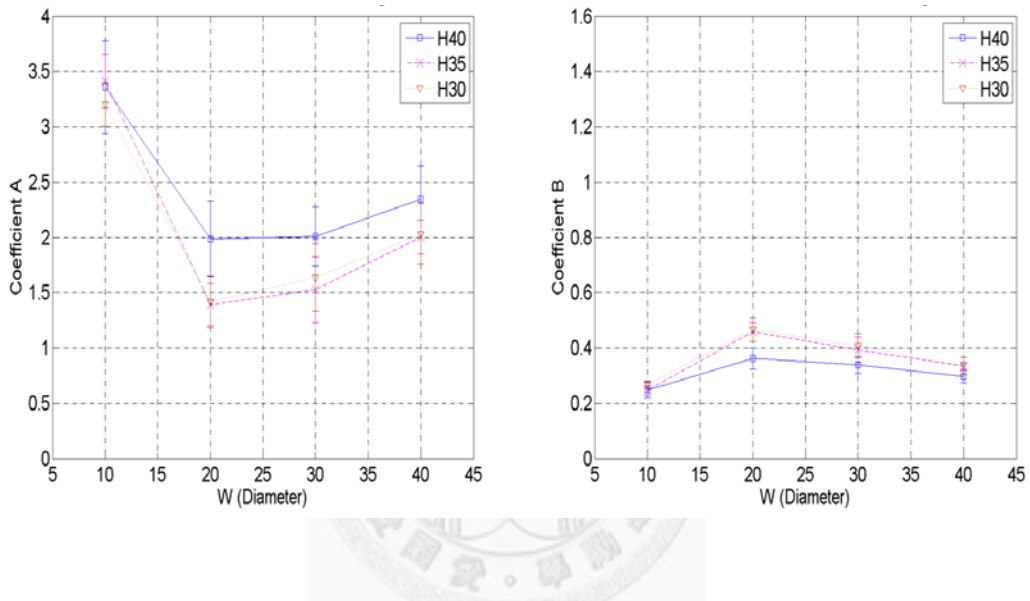


Figure 4.5 Different trends of decaying discharge profiles: (a) single linear trend for packing with $W>12$ cm. Here the case is for $W=24$ cm and $H=40$ cm; (b) mom-linear evolution profile for decaying discharge is found only for the narrow packing with $W=6$ cm. Here, $W=6$ cm and $H=35$ cm.

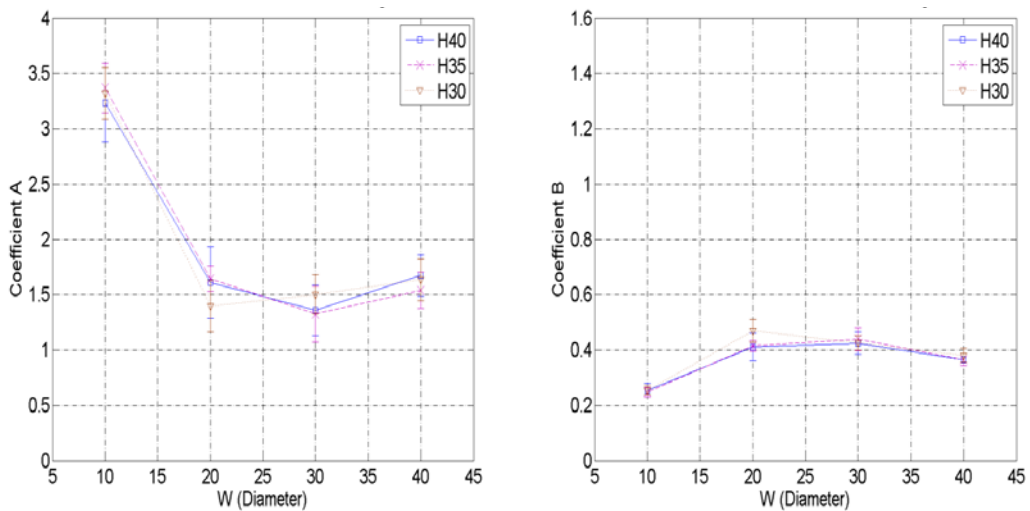
Recall that the difference in accumulated weight ΔW is calculated here with respect to the best-fit linear discharge profile and thus different fitting segments may

be employed. Thus, we systematically compare the exponents A and B for ΔW when the reference linear profile is fitted from different segments on the original $W-t$ plot. The fitted is indicated in the subtitle with increasing duration and the coefficient A and B are compared in the left and the right subplot, respectively, with respect to W and H.

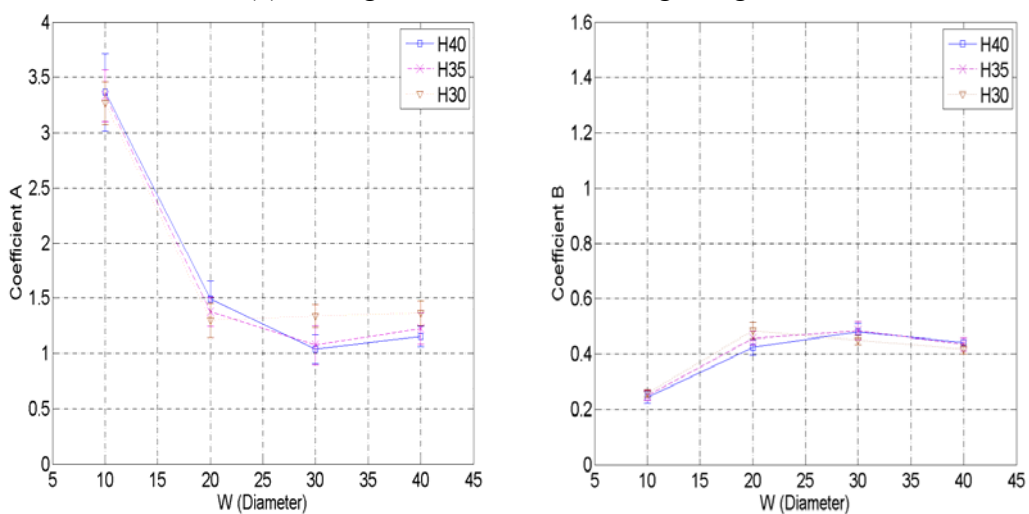
(a) Fitting in 5%~15% total weight segment.



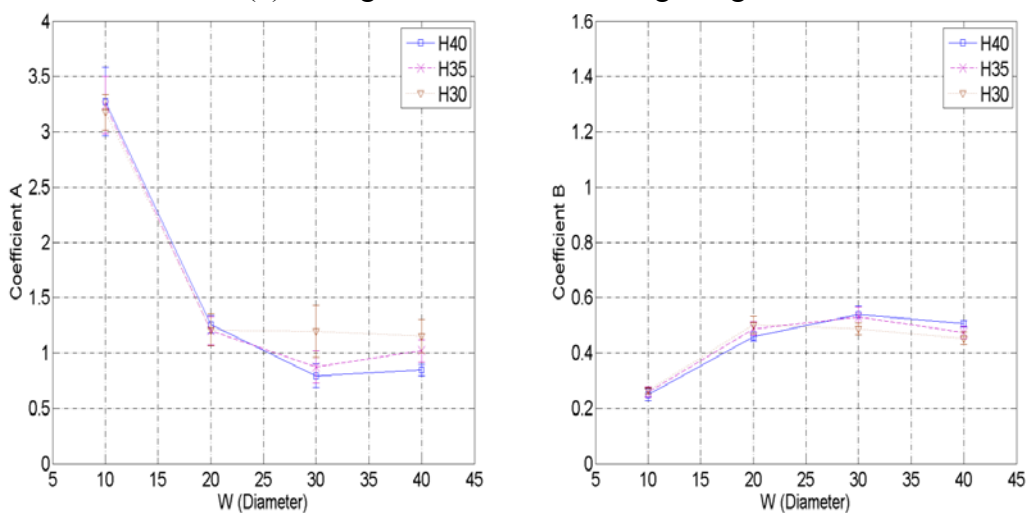
(b) Fitting in 5%~25% total weight segment.



(c) Fitting in 5%~35% total weight segment.



(d) Fitting in 5%~45% total weight segment.



(e) Fitting in 5%~55% total weight segment.

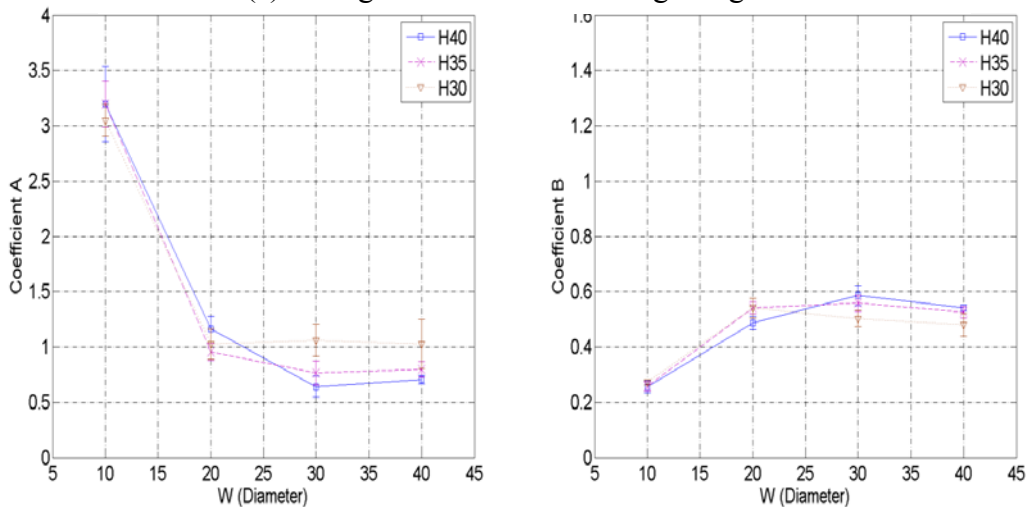


Figure 4.6 Exponents A and B in $\Delta W(t)$ from reference linear profiles obtained using segments of $\Delta W(t)$ data.

For discharges from wider packing with $w=12$ cm, 18 cm, and 24 cm, the best linear fit is determined from the 5-35% segment and the corresponding exponent constants fall in a narrow range as $1 < A < 1.5$ and $0.4 < B < 0.5$. The conforming tails from the discharge temporal profiles $W=6$ cm gives $3 < A < 5$ and $0.2 < B < 0.3$, we also note that packing height H has little or no influence on $\Delta W(t)$. It is worth noting that this phenomenon must result from flow overall dynamics and high-speed digital imaging technique has been employed to study flow features. In particular, we analyze the depth profiles of bulk velocity and solid volume fraction along the decaying discharge process.

4.3 Image-Based Analysis of Granular Flow Dynamics.

We already found that reservoir packing height, H , has negligible effect on A and B and thus we only consider the cases with the highest packing ($H=40$ cm) in the following investigation. Limiting by the camera memory, we could only record for 13.86 seconds with the chosen resolution (FPS=600). In order to cover the whole decaying behavior that often lasted over one minute, we repeated the experiments and started recording at consecutively shifted starting times. The recording time reference was set by the temporal signal of accumulated total weight, $W(t)$, for its good repeatability and any two consecutive camera recordings were overlapped to ensure that no information was lost. For example, for discharges from a packing with $W=6$

cm and $H=40$ cm, we recorded from 5 to 18.86 seconds in the first experiment. We repeated the experiment but shifted recording duration to 18~31.86 seconds, with an advanced starting time at 18 seconds from the previous terminal 18.86 seconds. A third experiment was recorded from 31 to 44.86 seconds using the same 0.86-second overlapped time and this procedure was repeated until the decaying discharge on $W(t)$ profile is mostly covered. We terminated the recording when the flow at the guide exit thinned down to one diameter thick. The total recording time for each packing width is summarized for later comparison: 5~75 seconds for $W=6$ cm, 10~91 seconds for $W=12$ cm, 25~103 seconds for $W=18$ cm, and 35~116 seconds for $W=40$ cm with constant $H=40$ cm.

The recorded sphere motions were analyzed at three observation lines—at the reservoir gate, in the guide center, and by the guide exit—as mentioned in section 4.1 (see figure 4.1). Each zone spans 7cm (12D) and the local sphere motions obtained from PTV were averaged by equation (3.1) and (3.2) using a square averaging box of 2D side-length and shift it by 0.2D to estimate a local bulk velocity and solid volume fraction, U and ϕ . An instantaneous depth profile can be generated by shifting the averaging box along the flow height.

4.3.1 Depth Profile for Bulk Velocity and Solid-Volume Fraction

Considering that extensive amount of high-speed images are obtained for the discharge of each reservoir packing, only one flow from either the narrowest ($W=6\text{cm}$) or the widest ($W=24\text{cm}$) was analyzed in this work. The bulk velocity and solid-volume fraction depth profiles were examined at specific times t_i to examine how each flow evolves in time. Since the images were captured at high frame rate (600PFS), the resulting PTV and hence bulk U and ϕ could fluctuate severely in time due to the small time interval. Thus, some local smoothing is required to ‘average-out’ these fluctuations for more meaningful bulk ‘instantaneous’ depth profiles and two methods were attempted. Firstly, we calculated four consecutive instantaneous depth profiles from t_i with a $\Delta t=1/600$ -second interval and we used their mean to represent the bulk mean instantaneous properties at t_i . For example, the velocity profiles at t_i , $t_i+\Delta t$, $t_i+2\Delta t$, and $t_i+3\Delta t$ are averaged to give $U(t_i, y)$ and similarly for $\phi(t_i, y)$. In the second method, we extract sphere information at t_i and $t_i+4\Delta t$ to calculate a new PTV giving instantaneous bulk $U(t_i, y)$ and $\phi(t_i, y)$ with an extended time interval of $4\Delta t$.

For the flow from the narrowest packing ($W=6\text{cm}$), the two bulk instantaneous velocity depth profiles were compared at the three observation lines—from up- to down-stream—introduced in section 4.1 (see figure 4.1), in figure 4.7(a)-(c) at $t_i =$

9, 22, 35, 50, and 63 seconds. In each subplot, the mean instantaneous depth profiles are shown by the red line with the corresponding standard deviation at each flow height indicated. The blue dots show the instantaneous depth profile by using the extended time interval. The corresponding depth profiles for solid-volume fraction at the three guide locations are provided in figure 4.8(a)-(c). The $U(t_i, y)$ and $\phi(t_i, y)$ from the thickest packing with $W=24\text{cm}$ are examined at $t_i = 35, 51, 65, 80, 93,$ and 109 seconds in figure 4.9 and 4.10, respectively, with each containing three subplots (a)-(c) for data obtained at the same three observation lines.

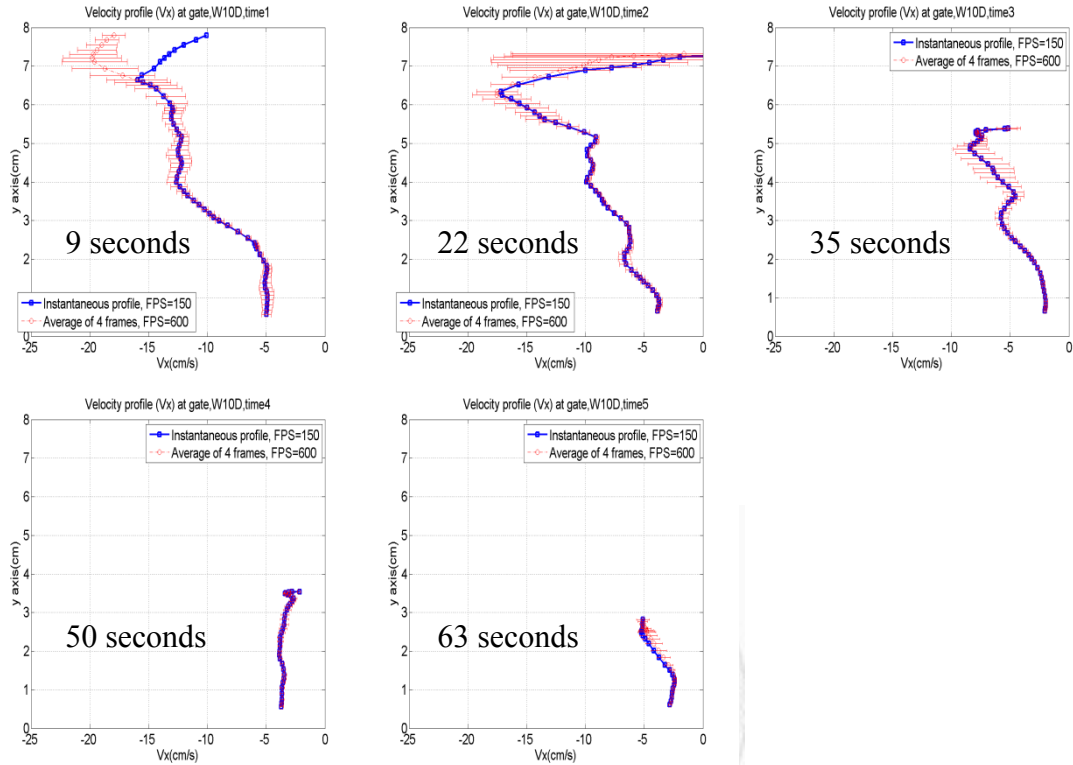
It is clear that the depth profiles from both estimation methods (the red line vs. the blue dots) give nearly matching U and ϕ results for both the flows from the narrowest and the widest packing over the inspected durations. However, severe deviation between the two depth profiles is observed for both U and ϕ from the two packing geometries—see $U(t=9\text{sec}, y)$ in figures 4.7(a) and 4.7(c), $\phi(t=9$ and 22 sec, $y)$ in figure 4.8(c), $U(t=35$ and $51\text{sec}, y)$ in figures 4.9(c), and $\phi(t=35$ and 51 sec, $y)$ in figure 4.10(c). All these discrepancies are found near the free surface of each flow at early times and mostly at the reservoir gate or the guide exit.

Possible reason is attributed to mismatch spheres in the nearest neighbor method which in turn gives erroneous PTV data. Recall that a search circle of radius of one sphere diameter is employed to identify possible spheres in the consecutive

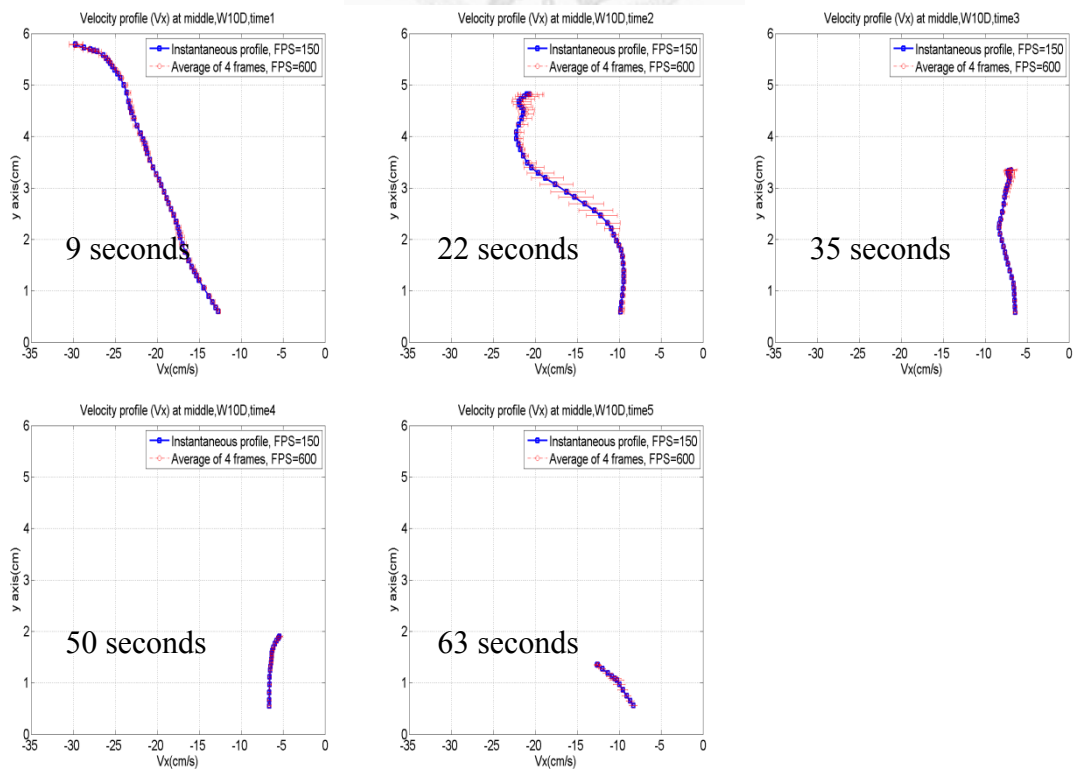
image to be matched to the candidate in the previous image. We identify the sphere possessing the shortest distance from the candidate in the second image to obtain PTV result for the candidate. However, in the regime of rapid sphere motion, the candidate sphere can move a large displacement downstream leaving vacancy for other spheres—from upstream or from the bulk away from the wall—to fill in as illustrated at Time 4 in figure 4.11. These newly emerging spheres (in dark shade) are much closer to the candidate original location (in dashed circles) than the candidate later locations (in solid circles). It is also possible that the candidate sphere moves to the vicinity of the original position of other candidates—as marked by the bold circles. All these scenarios can result in erroneous matching between two consecutive images giving wrong PTV results at Time 3. Such rapid change in sphere configuration may occur when the reservoir spheres are pushed through the gate at flow initiation like that shown in subplot (a) in figures 4.7 and 4.9. This scenario can also happen in loose flow at the free surface of the bulk leaving the guide exit in subplot(c) of those figures. The occurrence of mismatching and hence incorrect PTV data becomes inevitable when too large a time interval is adopted—like that between Time 1 and Time 4 in figure 4.11 or that in the second evaluation scheme. Thus, the mean depth profiles from four instantaneous PTV (with $\Delta t=1/600$ second interval) should give us more accurate data than the calculation using $4\Delta t$. In contrast, since the computation of ϕ

only requires the instantaneous sphere configuration, the depth profile without time averaging should be more accurate.

(a) W=6 cm, at the gate



(b) W=6 cm, in the middle of the guide



(c) $W=6$ cm, at the guide exit

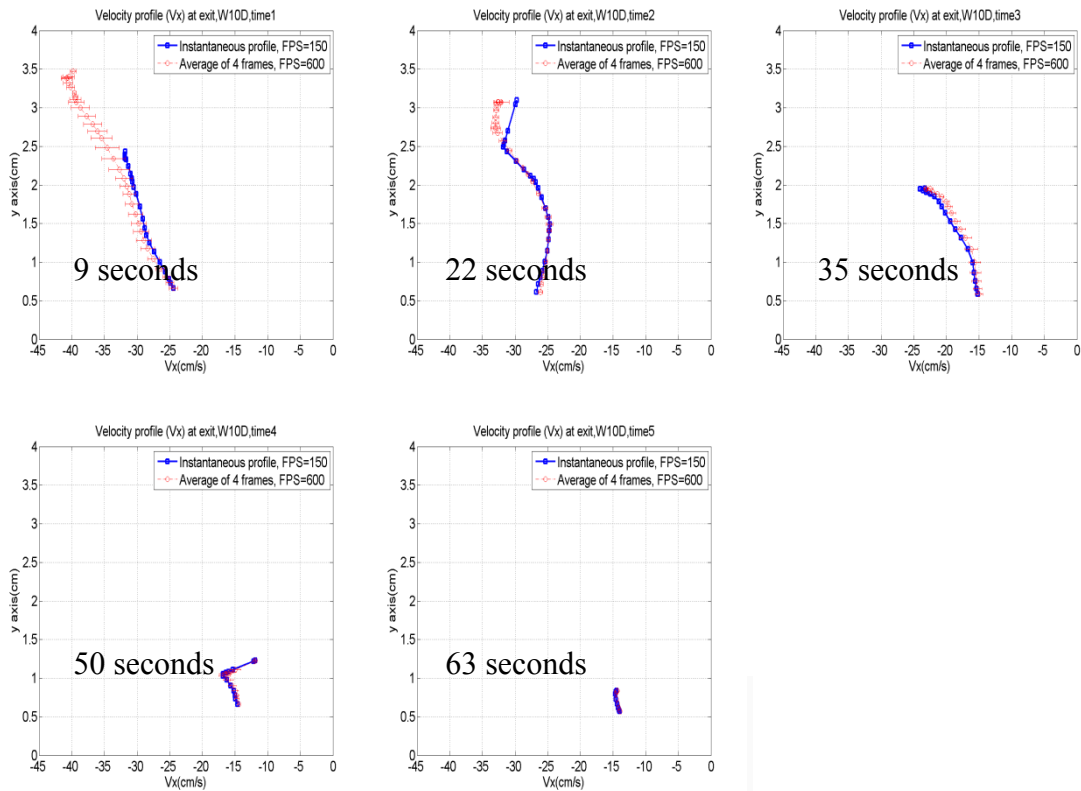
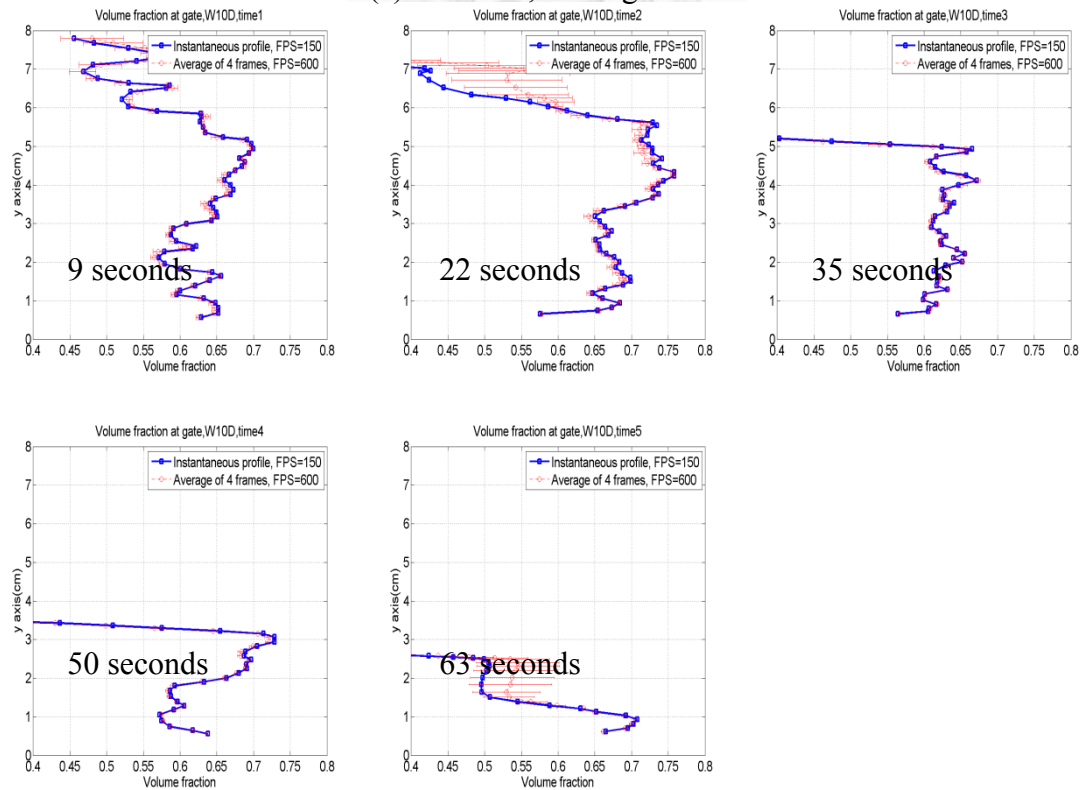
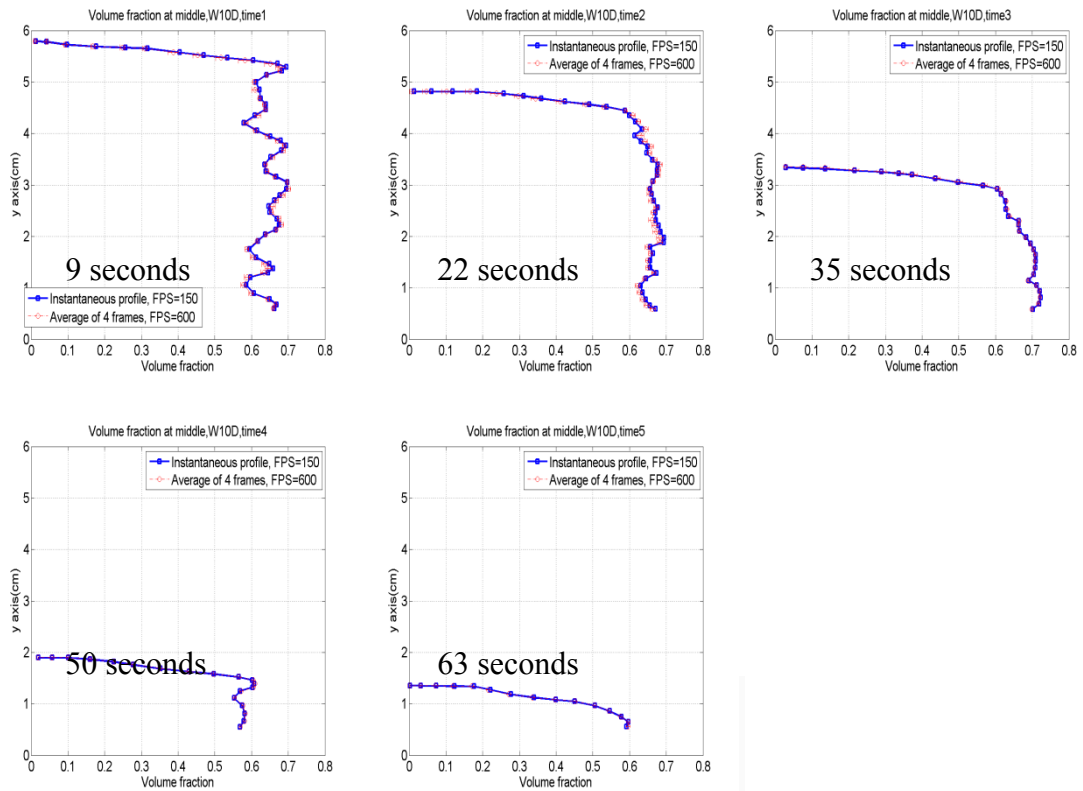


Figure 4.7 Instantaneous depth profile of bulk velocity for flow from the packing with $W=6$ cm at (a) reservoir gate, (b) middle of guide, and (c) guide exit. With specific inspection times in each subplot.

(a) $W=6$ cm, at the gate



(b) $W=6$ cm, in the middle of the guide



(c) $W=6$ cm, at the guide exit

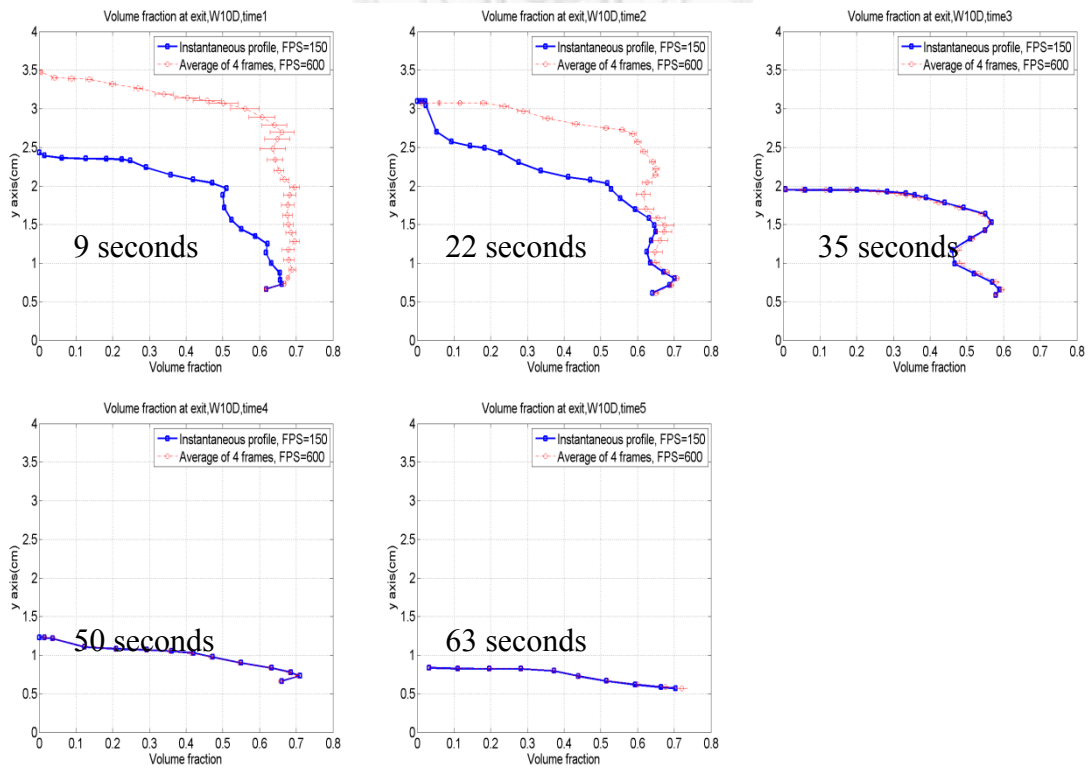
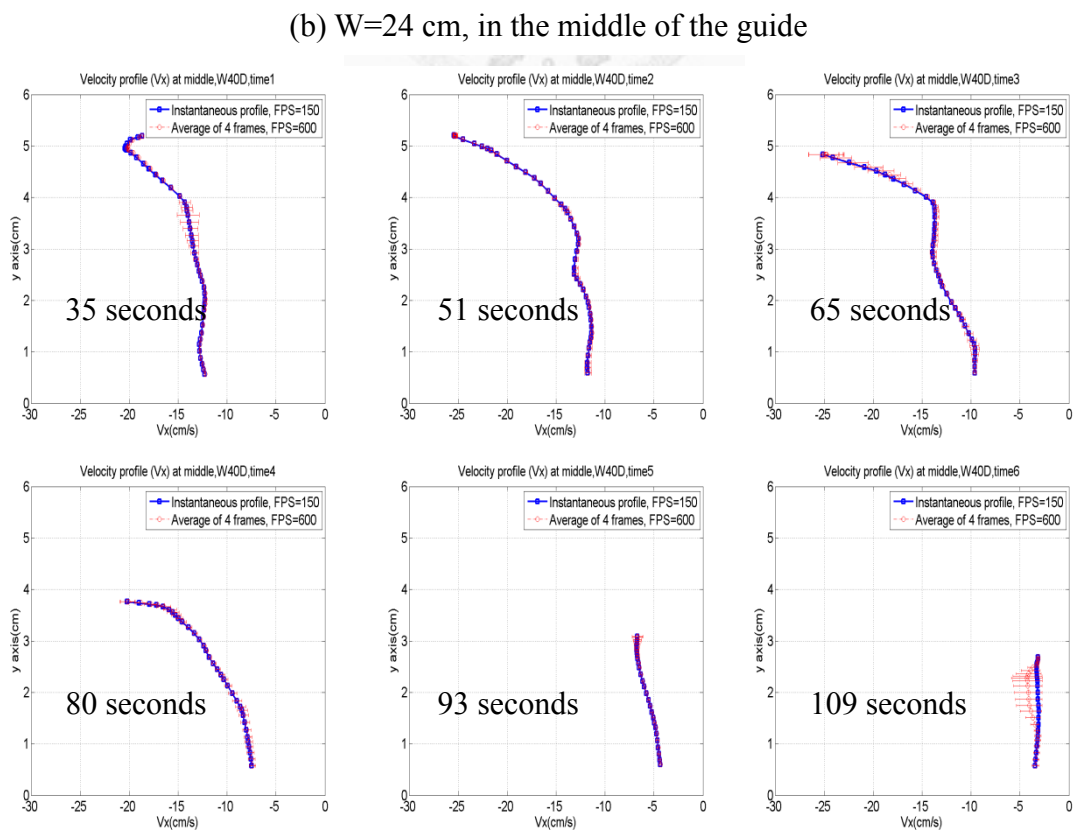
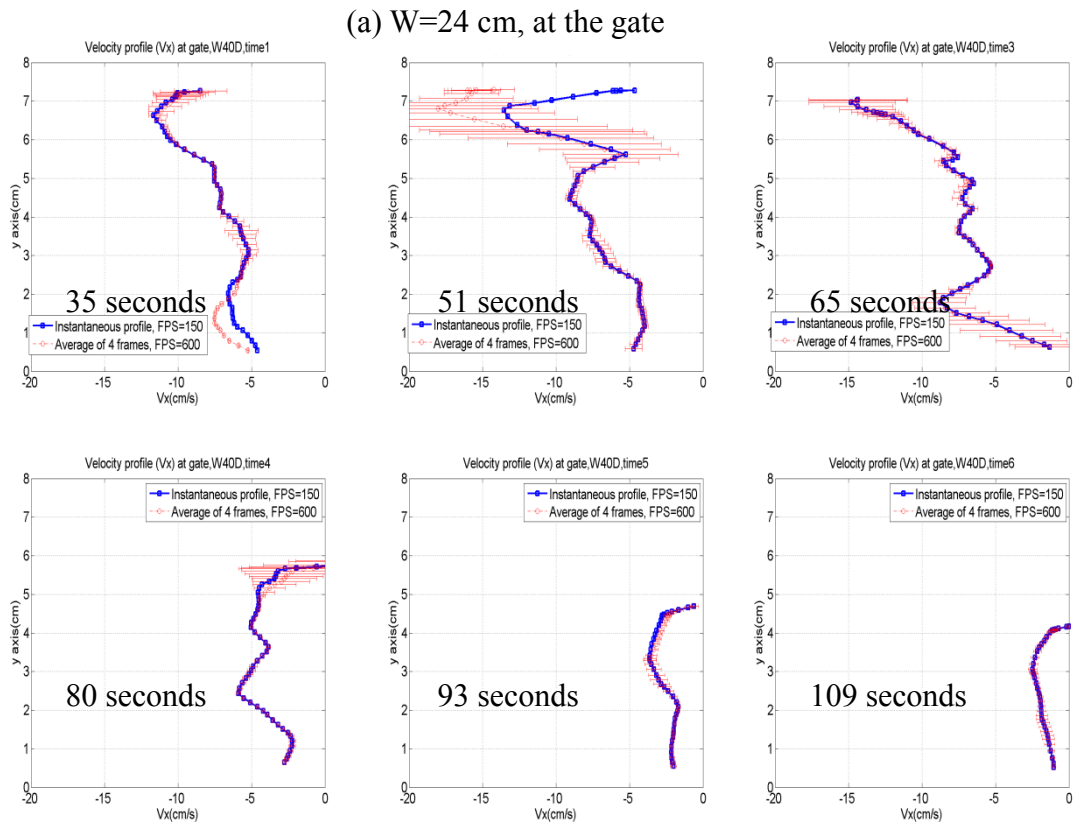


Figure 4.8 Instantaneous depth profile of solid volume fraction for flow from the packing with $W=6\text{cm}$ at (a) reservoir gate, (b) middle of guide, and (c) guide exit. With specific inspection times in each subplot.



(c) $W=24$ cm, at the guide exit

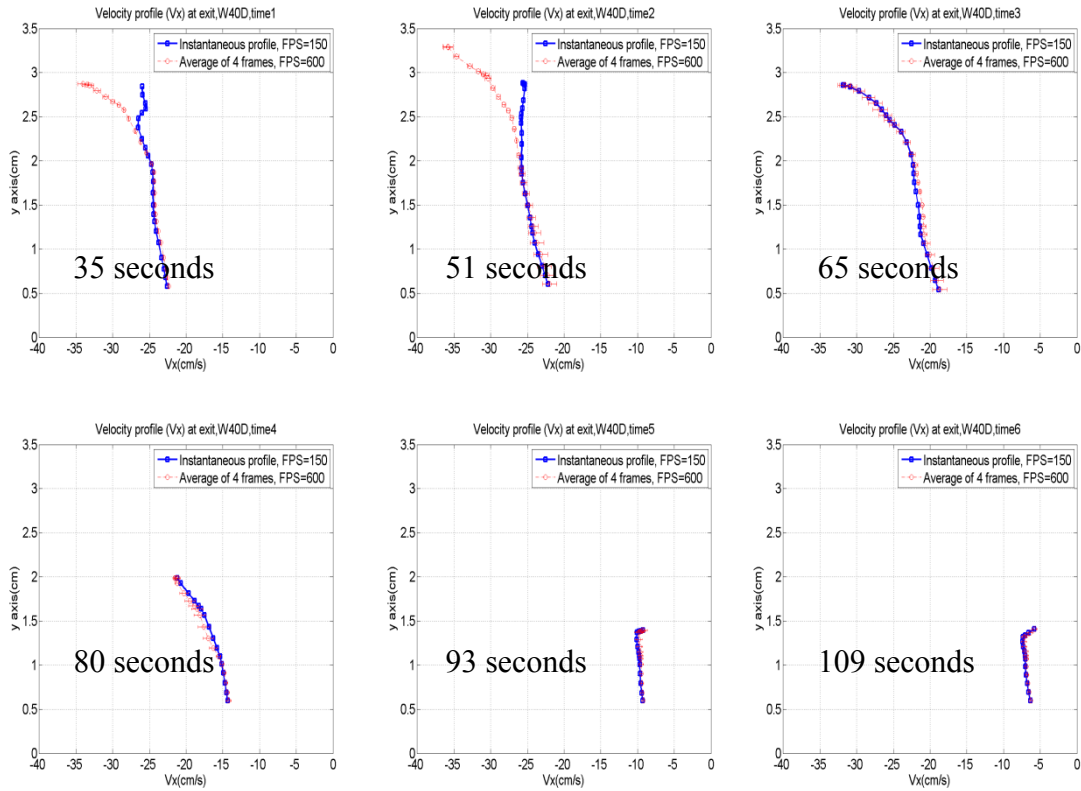
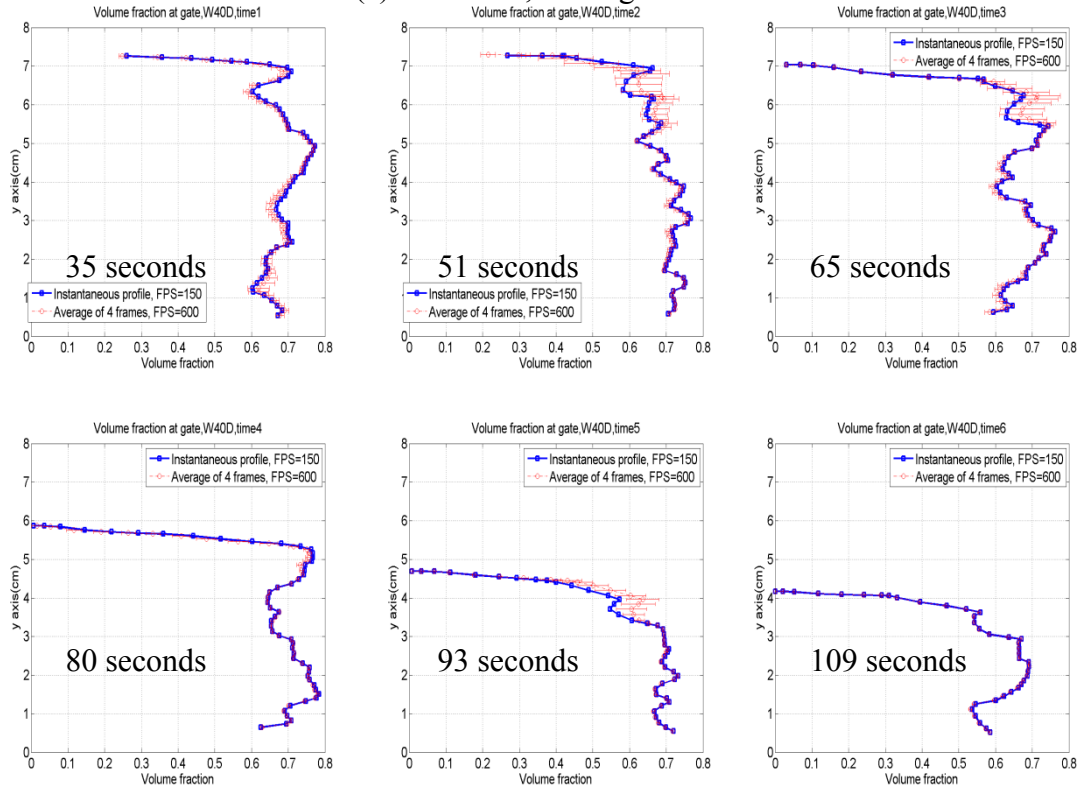
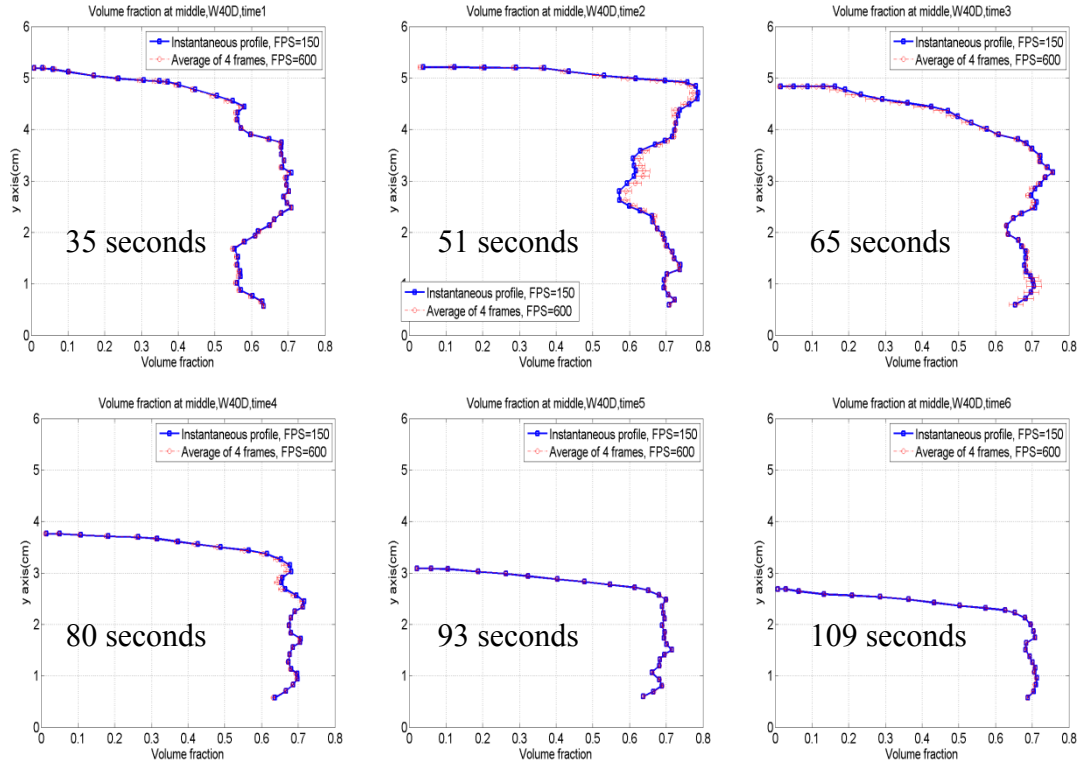


Figure 4.9 Instantaneous depth profile of bulk velocity for flow from the packing with $W=24$ cm at (a) reservoir gate, (b) middle of guide, and (c) guide exit. With specific inspection times in each subplot.

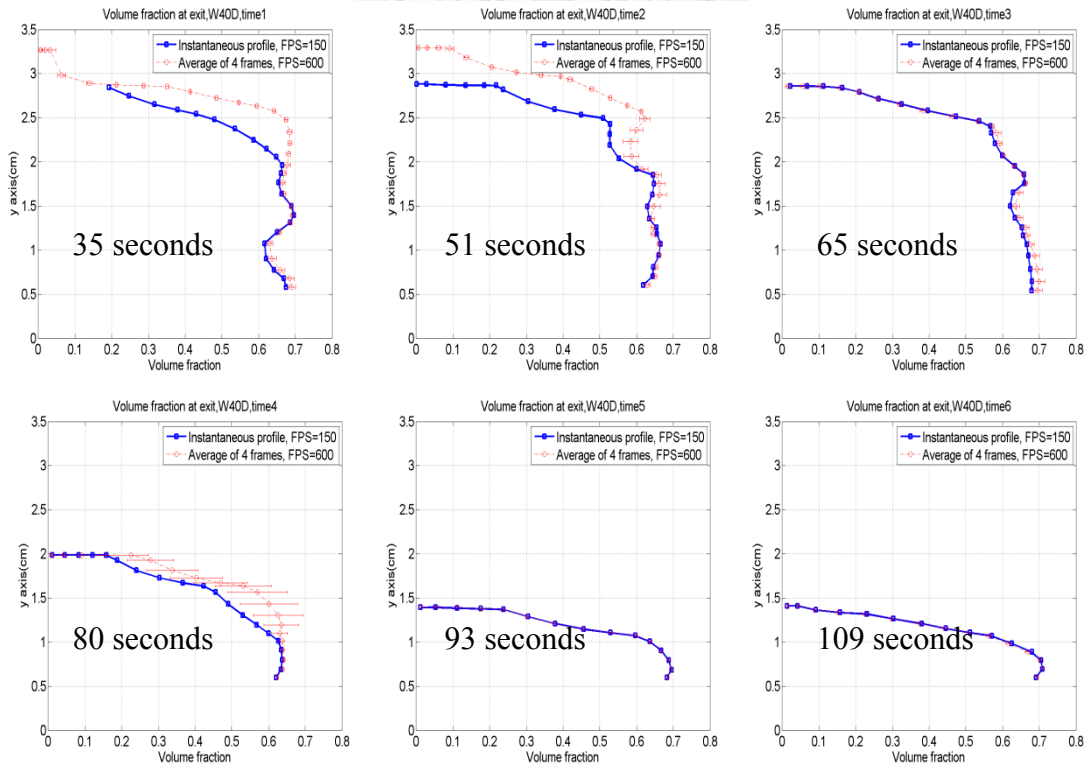
(a) $W=24$ cm, at the gate



(b) $W=24$ cm, in the middle of the guide



(c) $W=24$ cm, at the guide exit



(c)

Figure 4.10 Instantaneous depth profile of solid volume fraction for flow from the packing with $W=24\text{cm}$ at (a) reservoir gate, (b) middle of guide, and (c) guide exit. With specific inspection times in each subplot.

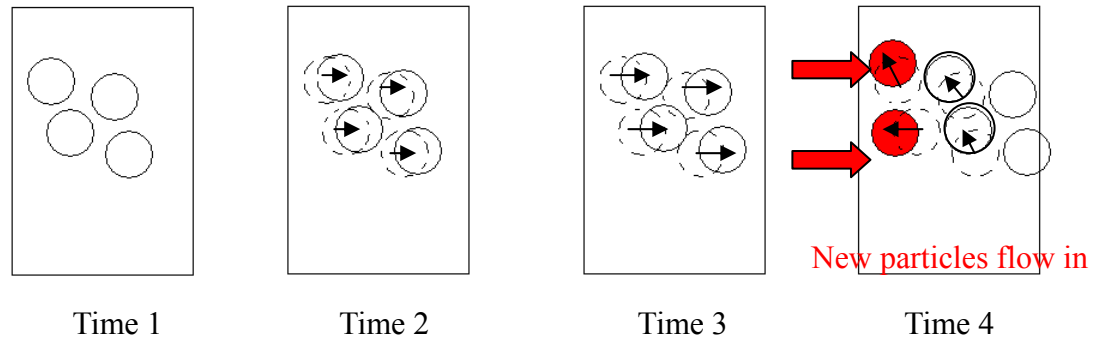
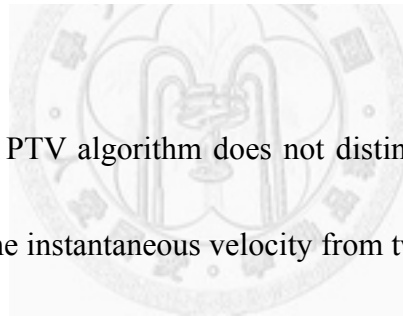


Figure 4.11 Illustration of the nearest neighbor method where mismatching spheres occur at Time 4.



Because the current PTV algorithm does not distinguish when such mismatch occur, we decided to use the instantaneous velocity from two consecutive images with $1/600$ interval and the instantaneous sphere configuration to obtain U and ϕ in the following analysis.

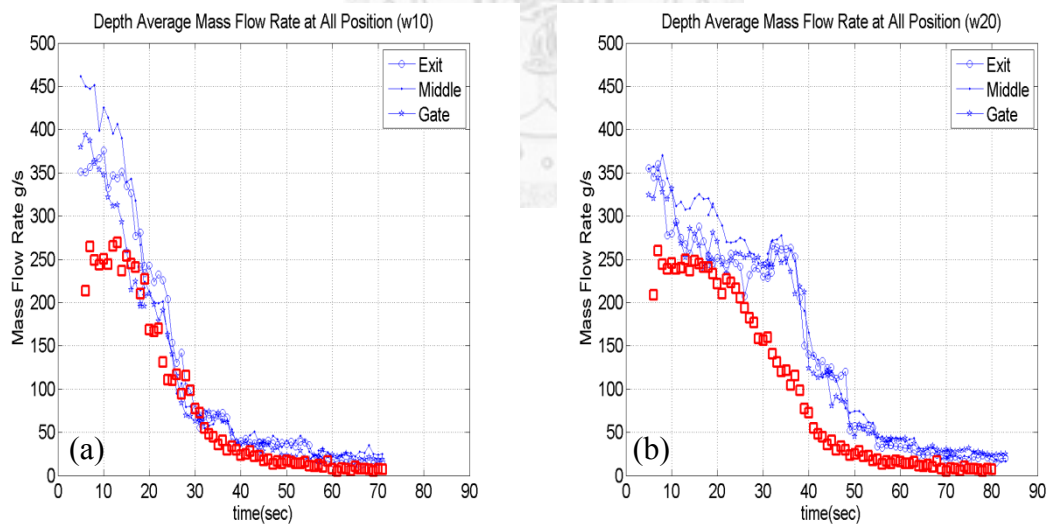
We then estimate the bulk mass flow rate from lateral 2D images and from load cell signal that represents the total deposited weight. Using bulk solid fraction and velocity profiles from 2D images and assuming that the mass flux is constant across the chute, we may estimate the mass flow rate at a specific streamwise location by

$$m_{image} = \rho_s w \int_0^h \phi u dz \quad (4.3(a))$$

where ρ_s represents the sphere density, w represents the chute width and h is the local flow depth. The mass flow rate can also be measured from load cell signal as

$$\dot{m}_{LC} = dW/dt \quad (4.3(b))$$

using the total deposited weight, $W(t)$. Equation 4.3(b) is actually the time rate of change of $W(t)$ in figure 4.2. The mass flow rates from equation 4.3(a) and 4.3(b) at different streamwise positions are compared in figure 4.12 for flows from different reservoir packing widths. In these figures, the red squares are for \dot{m}_{LC} and the blue circle, dot, and star lines are for \dot{m}_{image} .



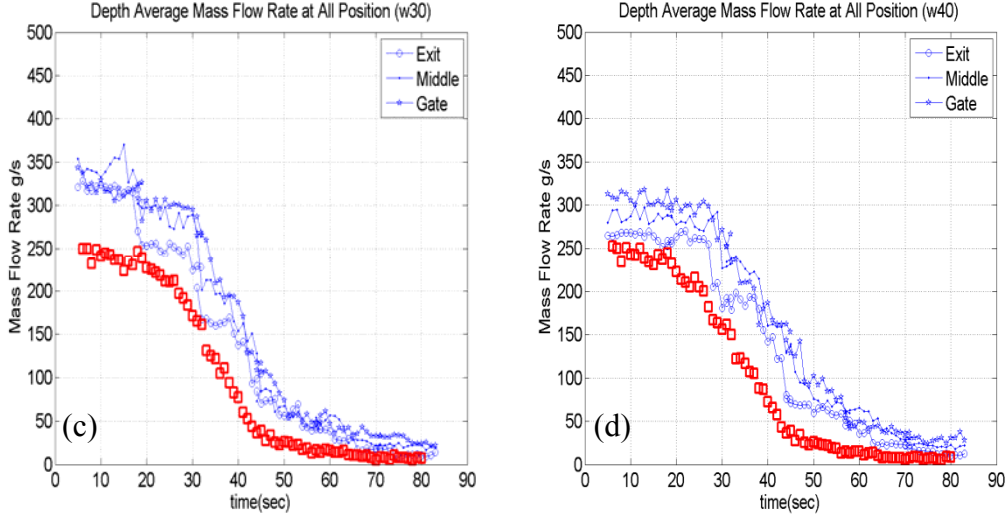


Figure 4.12 Instantaneous mass flow rate calculated by 2D image analysis (blue), and by load cell signal (red), with constant depth and different packing width (a) $W=6\text{cm}$, (b) $W=12\text{cm}$, (c) $W=18\text{cm}$ and (d) $W=24\text{cm}$.

It is clear that \dot{m}_{image} is overestimated throughout the observation for all packing width, W . We suspected that the overestimation is due to the error in volume fraction estimated from the lateral images. To estimate an upper bound for overestimation, we consider a 3D minimum volume fraction, $\phi_{min} = 0.4$, in which packing persistent contacts exists throughout the control volume. Nonzero $\phi_{image} - \phi_{min}$ can result in instantaneous difference in mass flow rate as

$$\Delta \dot{m} = \rho_s w \int_0^h (\phi_{image} - 0.4) u dz \quad (4.3c)$$

where ϕ_{image} is the bulk volume fraction estimated by 2D lateral images. The results obtained at the gate, middle, and the guide exit are shown by blue, red, and black respectively in figure 4.13 for the four packing widths. On the same plot, the

overestimated flow rate from the load cell data, $\dot{m}_{image} - \dot{m}_{LC}$, are also shown by blue, red, and brown lines.

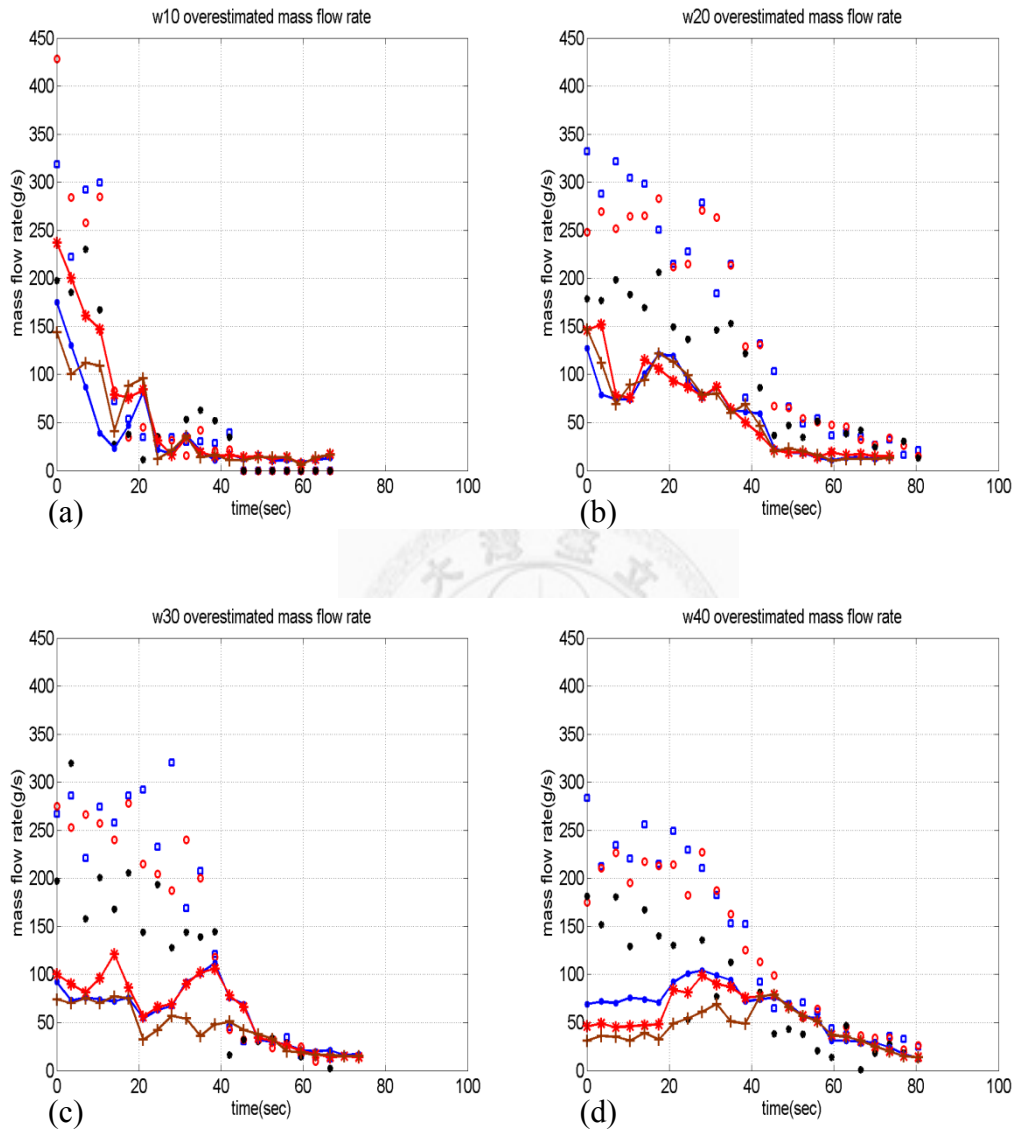


Figure 4.13 Instantaneous difference on mass flow rate, $\dot{m}_{image} - \dot{m}_{LC}$ in solid lines and Δm in scattered points. With a 3.5 seconds interval and different colors stands for different streamwise positions. (a) $W=6\text{cm}$, (b) $W=12\text{cm}$, (c) $W=18\text{cm}$ and (d) $W=24\text{cm}$.

From figure 4.13, it is obvious that $\dot{m}_{image} - \dot{m}_{LC}$ is smaller than the difference $\Delta \dot{m}$ from an assumed minimum ϕ_{min} in equation 4.3(c). This implies that the actual flow is denser than ϕ_{min} . However, when the two data sets conform at later times, $t > 20$ seconds for $W=10$ in figure 4.13(a) and $t > 40$ seconds for the rest, the actual flow volume fraction asymptotes to ϕ_{min} and the bulk moves in a loose formation.



4.3.2 Decaying Bulk Velocity and Solid-Volume Fraction

Considering that the accumulated weight reflects bulk overall dynamics which should be less sensitive to local changes in bulk properties as portrayed by those depth profiles. Thus, we further calculate the *depth-averaged* bulk velocity U and solid volume fraction ϕ at a specific streamwise location as:

$$\bar{U}(x) = \frac{\sum_{i=1}^N U_i(x, y_i)}{N}, \text{ and} \quad 4.4(a)$$

$$\bar{\phi}(x) = \frac{\sum_{i=1}^N \phi_i(x, y_i)}{N}. \quad 4.4(b)$$

In these expressions, N represents the total number of averaging boxes stacked at x , U_i and ϕ_i denotes the corresponding bulk velocity and solid volume fraction for each box. By monitoring $\bar{U}(x)$ and $\bar{\phi}(x)$ in time, we obtained the temporal profiles of depth-averaged bulk velocity, $\bar{U}(x, t)$, and solid volume fraction, $\bar{\phi}(x, t)$, at a streamwise location. In this work, three x_s were considered as those introduced earlier at the reservoir gate, middle of the gate, and at the guide exit.

For each reservoir packing, we chose a time close to the end of its steady charge and monitored the subsequent depth-averaged velocity and solid volume fraction. Figure 4.14(a)-(d) shows the results at three x_s for packing with $W=6\text{cm}\sim 24\text{cm}$, but identical $H=40\text{ cm}$. The initial plateau in each figure corresponds to its data in steady

discharge. Clearly, the flow from the packing with $W=6\text{cm}$ exhibited the fastest velocity at the beginning at all x_s in figure 4.13(a) but slowed down quickly with a mild rise at the end. The profiles for other larger packing slowed down more mildly throughout the decaying discharge. The possible reason for the final rise in $W=6\text{cm}$ will be discussed later.

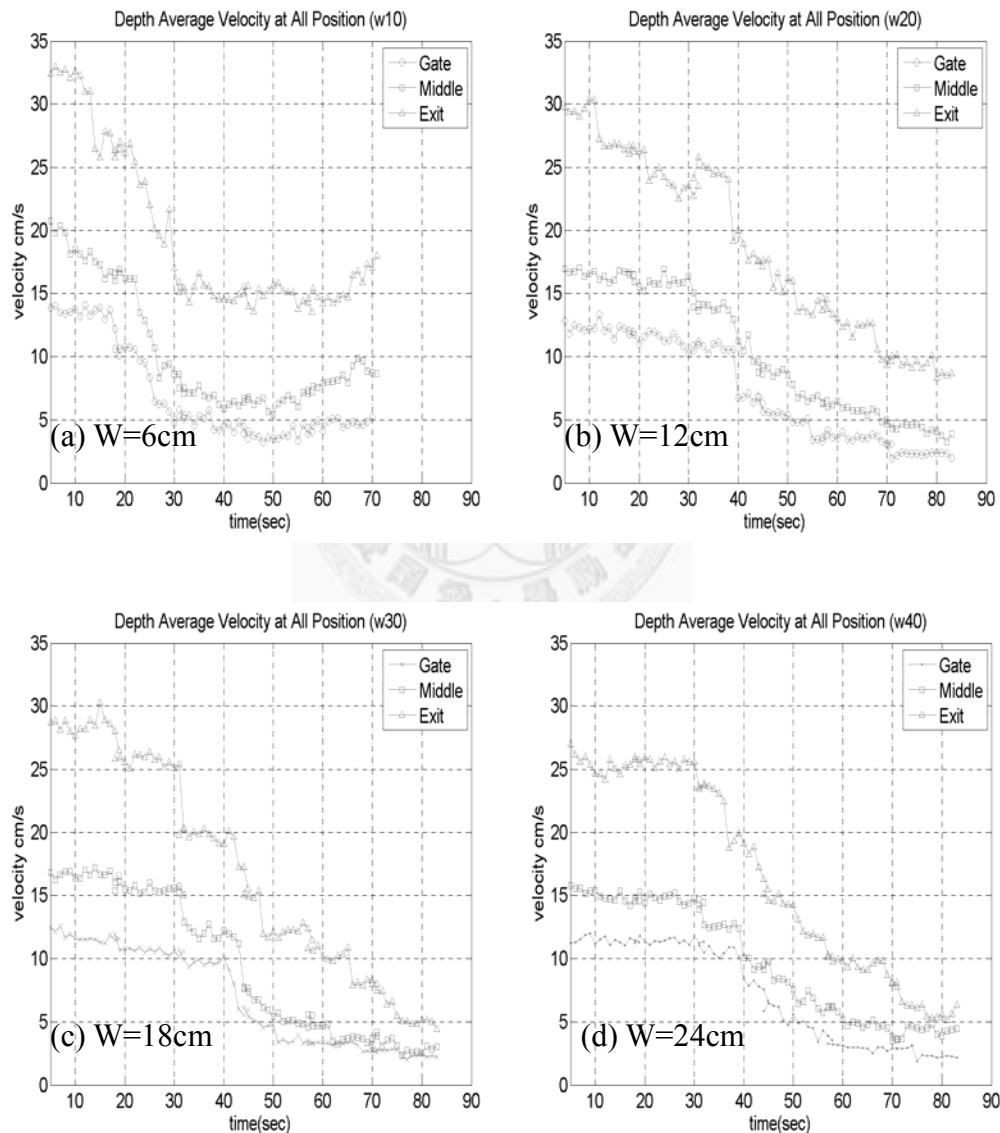


Figure 4.14 Temporal evolution of bulk depth-averaged velocity at specific x_s for four reservoir packing geometries (a)-(d) $W=6\text{cm}$, 12cm , 18cm , and 24cm .

Next, we rearranged the data and examine $\bar{U}(t)$ from the four packings at the three streamwise locations in figure 4.15(a)-(c). The peculiar discharge feature for the flow from the narrowest packing $W=6\text{cm}$ is revealed more clearly. At the beginning, the profiles for $W=6\text{cm}$ show the same trend as others but dramatic drops soon follows as indicated by the bold arrows while the other profiles remain mildly decreasing until a much delayed drop.

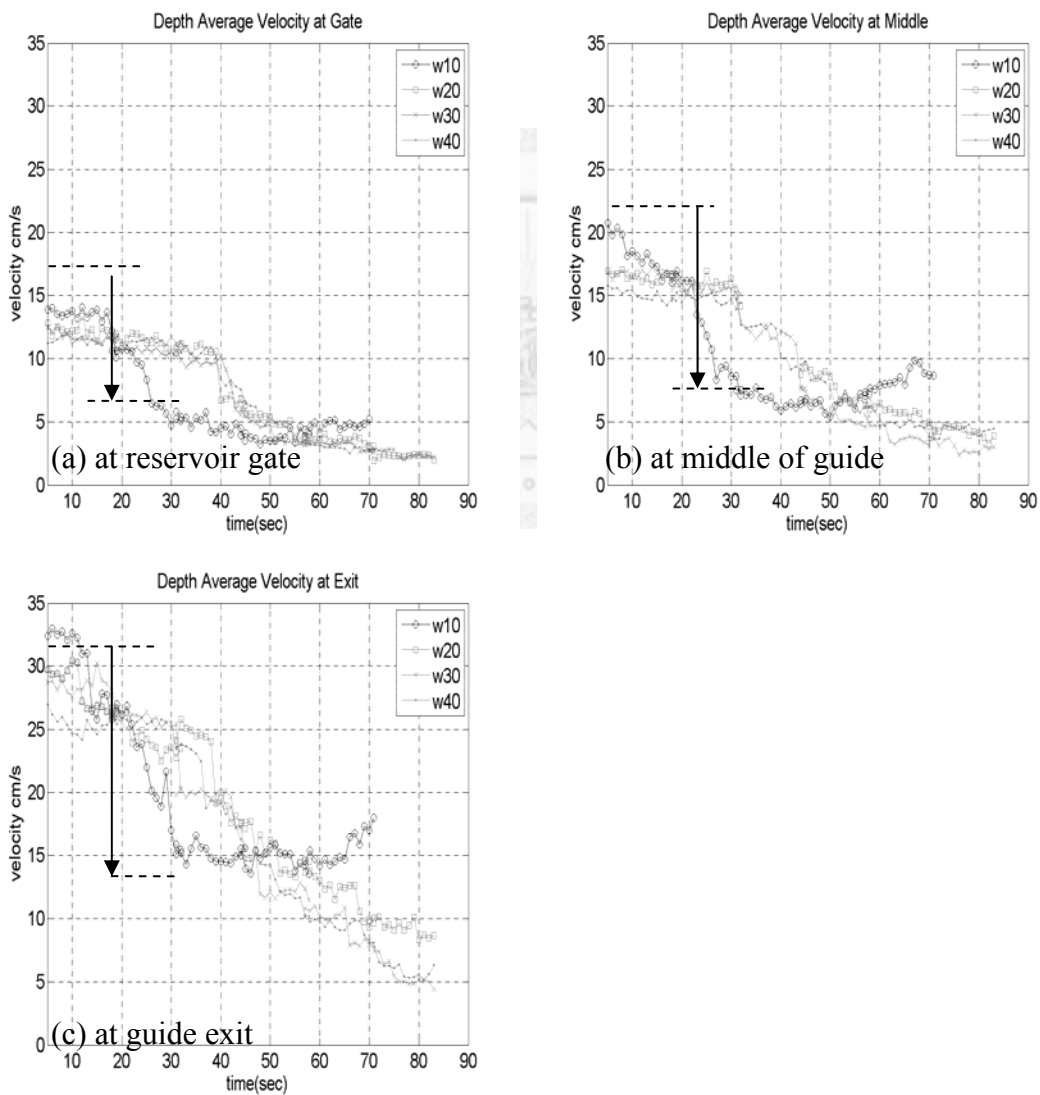


Figure 4.15 Temporal profiles for depth-averaged bulk velocity at three x_s for flows from different packing width ($W=6, 12, 18,$ and 24cm) and identical $H=40\text{cm}$.

In addition to bulk velocity, the flow solid volume fraction can also affect the temporal profile of the accumulated discharge bulk weight. The temporal evolution of depth-averaged bulk solid volume fraction estimated at the three streamwise locations is compared for different reservoir packing geometries is figure 4.16(a)-(d). Another set of comparison is made in figure 4.17 focusing on discharges from different packing at the same streamwise location on the guide.

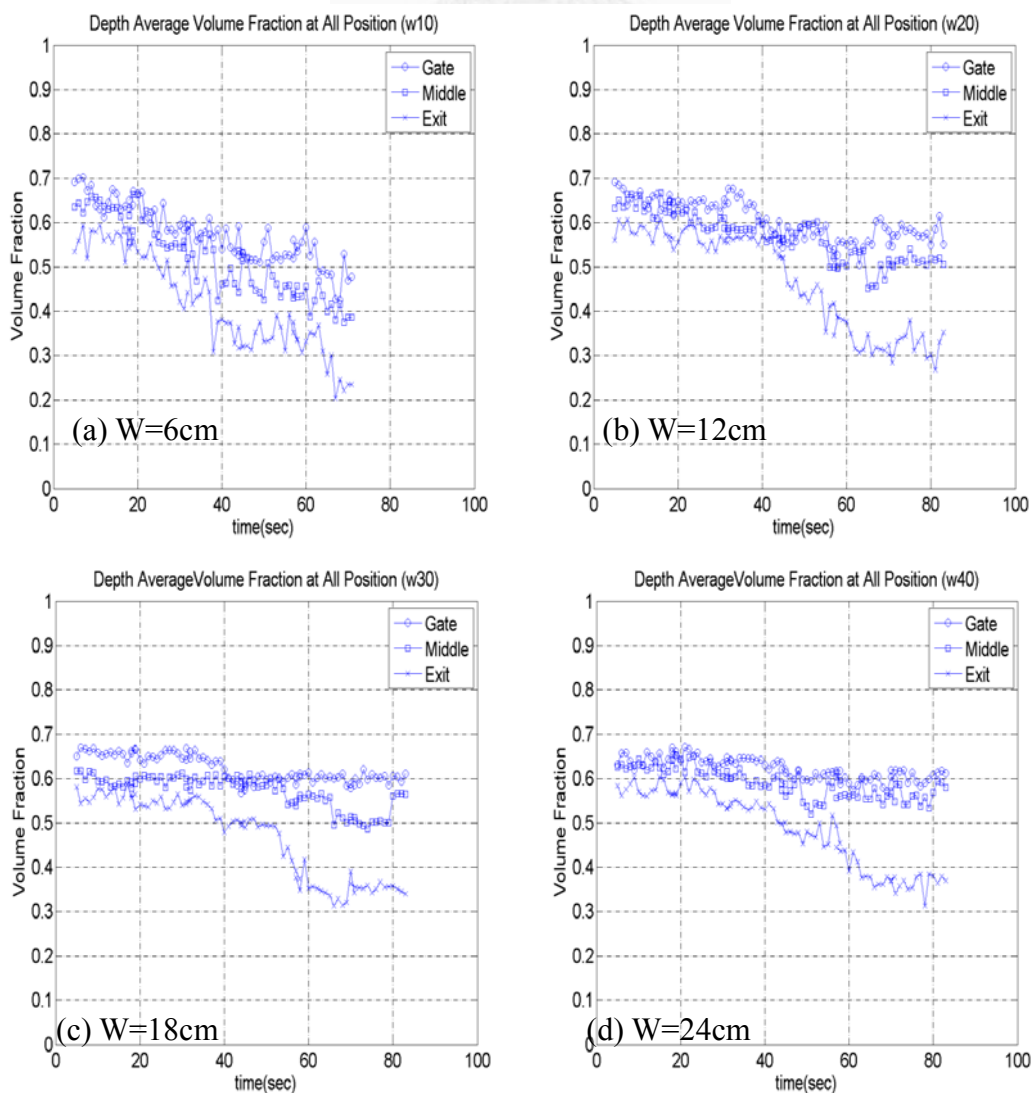


Figure 4.16 Temporal profile of depth-averaged bulk solid volume fraction for flows from different reservoir packing along the three streamwise location: (a) $W=6\text{cm}$, (b) $W=12\text{cm}$, (c) $W=18\text{cm}$, and (d) $W=24\text{cm}$.

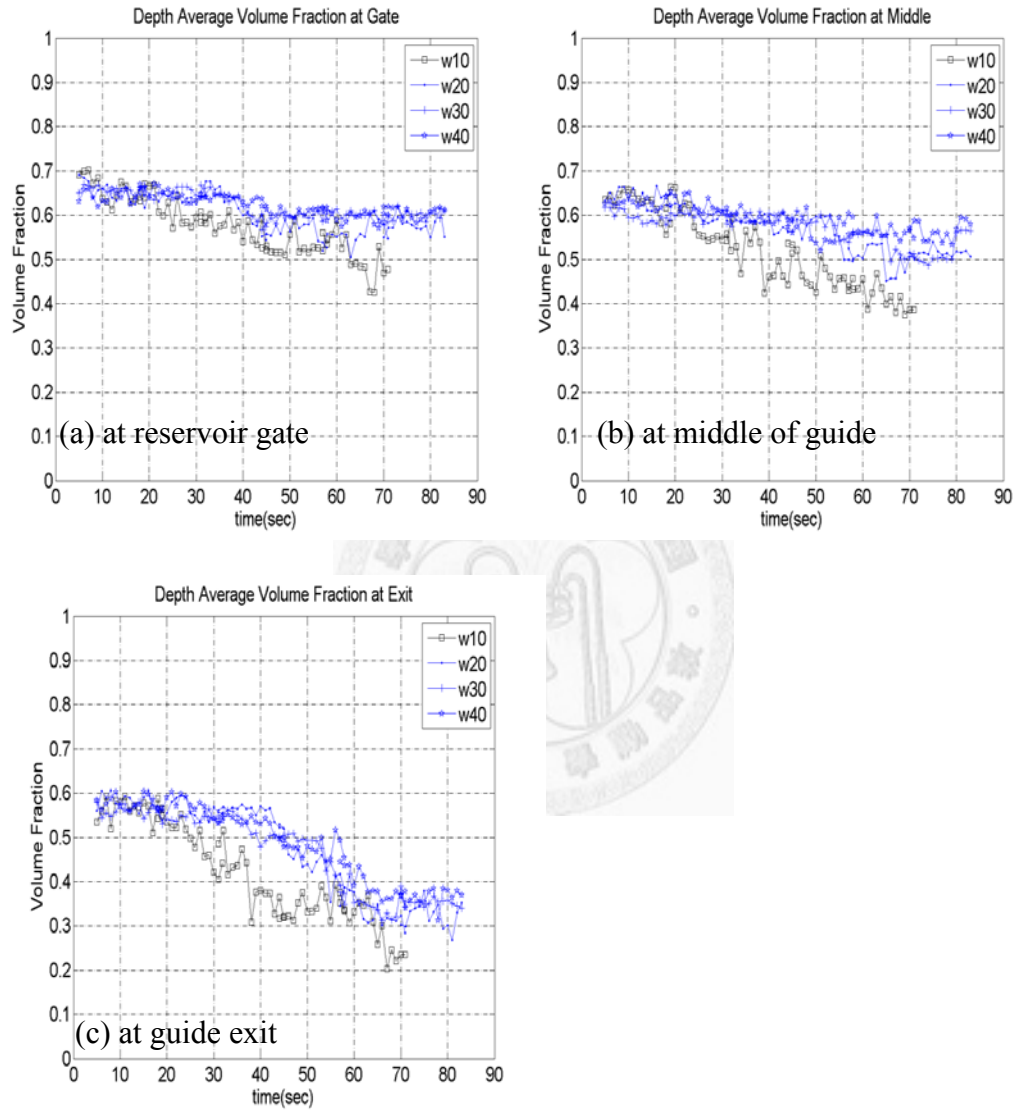


Figure 4.17 Temporal profile of depth-averaged bulk solid volume fraction at different streamwise locations with four reservoir packing widths.

Form figure 4.17, it is apparent that the solid volume fraction for the flow from the narrowest packing ($W=6\text{cm}$) went through more unsteady decay at the three

streamwise locations as compared to the rest three packings. We attempt to estimate a degree of overall decay by:

$$D = \frac{\bar{\phi}_{ref} - \bar{\phi}_{final}}{\bar{\phi}_{ref}} \times 100\%, \quad (4.5(a))$$

in which $\bar{\phi}_{ref}$ is a reference value calculated by the sum of the first thirteen $\bar{\phi}_i$, which should correspond to the plateau for steady discharge. The second term $\bar{\phi}_{final}$ calculates the sum of *last* thirteen $\bar{\phi}_i$. The sequence of D thus indicates the degree of decay of $\bar{\phi}(t)$ during the whole discharge. The values obtained for the four packing geometries with identical height (H=40cm) at the three locations are provided in Table 4.1. An apparently higher D is found for the narrowest packing (W=10D) for all locations, especially at downstream side.

Table 4.1 Overall decay level (equation 4.4(d)) for flows from different packing widths at the three locations.

Streamwise location Packing width	Gate	Middle	Exit
W=6cm	28.2%	38.2%	50.6%
W=12cm	14.3%	23.4%	47.4%
W=18cm	7.72%	16.7%	36.4%
W=24cm	7.71%	11.3%	34.5%

To find a correlation between the occurrence of dramatic changes in $\bar{\phi}(t)$ and that in $\bar{U}(t)$, we changed to use a local reference, $\bar{\phi}_{ref} = \sum_{i=n}^{n+13} \bar{\phi}_i, n = 1, 2, 3 \dots$ to estimate a local decay degree in order to characterize the onset of abrupt change takes place. A local decay can be estimated by:

$$D_l = \frac{\sum_{i=n}^{n+13} \bar{\phi}_i - \sum_{i=n+13}^{n+26} \bar{\phi}_i}{\sum_{i=n}^{n+13} \bar{\phi}_i} \times 100\%, n = 1, 2, 3 \dots \quad (4.5(b))$$

In other words, the numerator of 4.4(b) calculate the difference between the sum of thirteen consecutive $\bar{\phi}_i$ starting at n and the sum of the following thirteen $\bar{\phi}_i$. The time, n, when a 10% local decay occurs is determined and summarized in table 4.2 showing clearly that such decay occurred much earlier for the flow from the narrowest packing.

Table 4.2 Local decay level (equation 4.4(b)) for flows from different packing widths at the three locations.

Streamwise location Packing width	Gate	Middle	Exit
W=6cm	22sec	22sec	17sec
W=12cm	46sec	44sec	42sec
W=18cm	none	50sec	33sec
W=24cm	none	50sec	35sec

If we mark these moments on the corresponding velocity temporal profiles in figure 4.18, it is observed that the time of 10% local decay of $\bar{\phi}(t)$ agrees reasonably well to the onset of dramatic drop in $\bar{U}(t)$ implying local flow dilatation. Such agreement is found for all packing geometries at the guide exit and near the reservoir gate for flows from the packing with $W=6\text{cm}$ and 12cm .

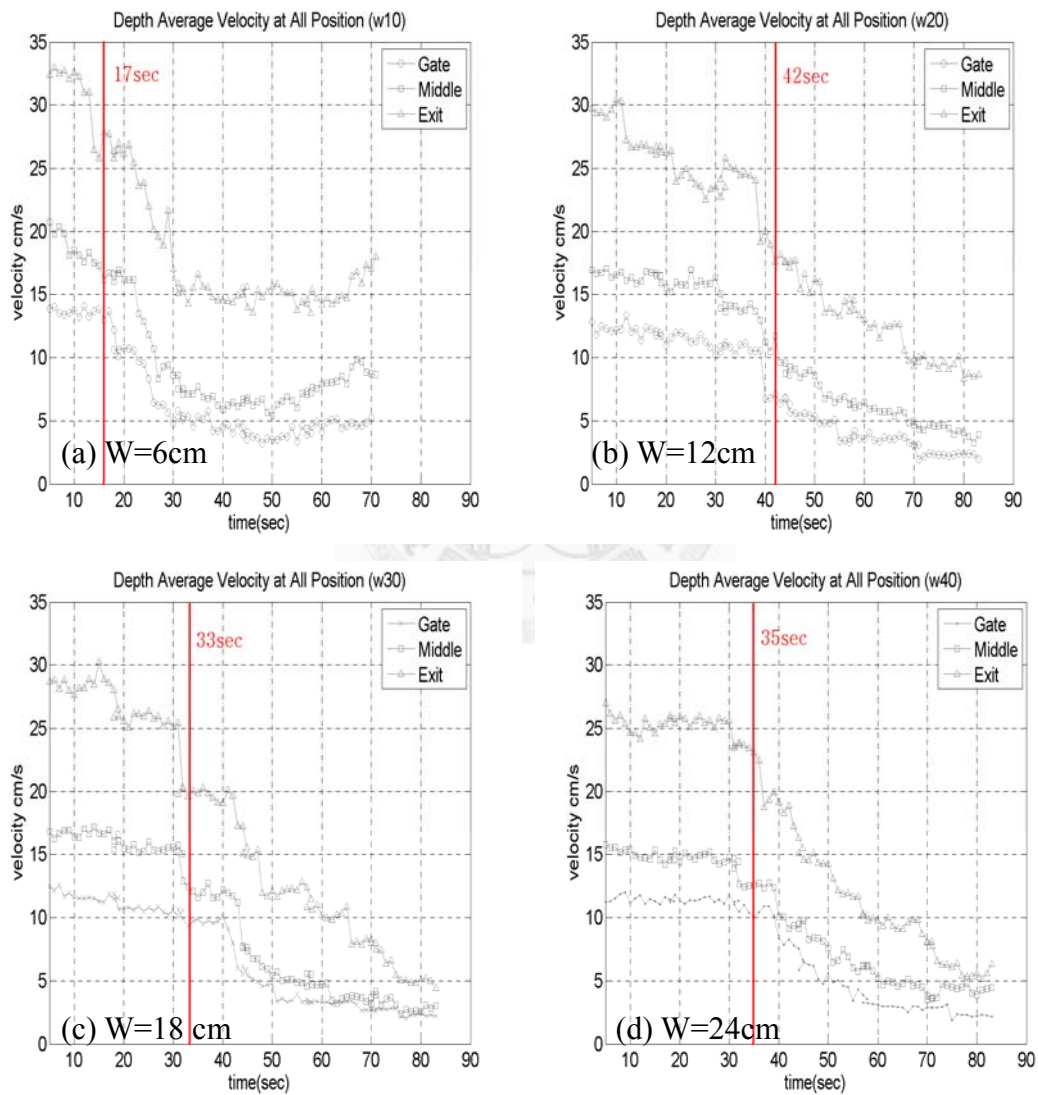


Figure 4.18 Comparison of the time with 10% local decay in $\bar{\phi}(t)$ (marked by the red vertical line) to the temporal profiles of $\bar{U}(t)$ from different packing geometries

Chapter 5 Impact Force of a Steady dry Granular Flow

This chapter focuses on the resulting force when a steady dry granular flow impinge an obstacle on an inclined chute. Three force components on the obstacle were measured simultaneously including the impact force, the tangential shearing and the normal loading forces on the obstacle surface. We also capture high-speed images on the resulting flow from which the same force components are estimated from a two-dimensional control volume analysis. The data from such 2D estimation is compared to the in-situ 3D measurement to evaluate the performance of such image-based research method.

5.1 Experimental Facility

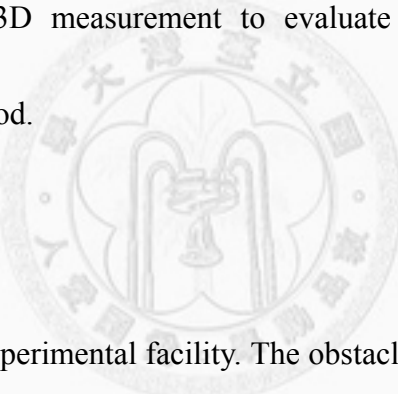


Figure 5.1 shows the experimental facility. The obstacle was constructed using the load cell module introduced in section 2.1.3 and was fixed at a position 100cm downstream from the reservoir gate. (granular mass of different dimensions with $H=40$ cm and $W=6$ cm~24 cm were prepared.) The chute angle was adjusted to $\theta=20, 23,$ and 26 degrees from the horizontal. To facilitate flows across the load cell box, we added flat plates of different thickness so that two depths $h=2.4$ cm and 4.8 cm were created from the load cell top surface (see Fig 5.1(b)). The load cell signal—including the impact force, the tangential shearing and the normal loading forces—was acquired at

1000Hz while the sphere motions were recorded by a lateral high-speed digital camera at 600FPS. The camera was rotated so that the CCD lower edge matches to the chute base, followed by the calibration procedures described in section 2.1.2.



Figure 5.1 Experimental facility: (a) the chute and where the load cell module was installed; (b) flow depth h from the load cell top surface to the base.

5.2 Impact, Shear and Normal Signals

We converted the load cell signals via the verified weight-voltage relationship in section 2.1.4. For the two load cells for the impact and normal loading forces, their default signal is negative for compressive component. For the shear load cell, we installed in the direction that a force in the streamwise direction gives positive signals. We first examine the measured forces for a steady flow from different reservoir packing geometries, with $H=40$ cm and $W=6$ cm~24 cm, down a 20-degree chute of 4.8 cm-depth. For each packing, three experiments were conducted and the results

with increasing W are shown in figure 5.2(a)-(d). The impact force from the front load cell box and the shear and normal loadings from the rear box (see figure 2.3) are shown by the black-solid line(—), the black-dashed line(----), and the gray-dash-dot line(-.-.-), respectively. It is observed that the impact force increases quickly and becomes steady at roughly 10~12 seconds after flow impingement; the normal and the shear loadings on the rear load cell box, however, remain nearly zero. To explain these findings, we turn to examine the flow images and all the steady flows from the four packing geometries did not climb over the load cell module but piled in front of it. When the flowing mass was brought to an abrupt stop giving a sharp increase of the load signal to a steady plateau. A reflection pressure wave propagated upstream. When the wave front met the upcoming granular mass, the flowing spheres were brought to a halt generating a phenomenon similar to shock-wave as reported by Gray (reference [15]). A granular bore developed upslope at nearly constant speed, arresting the flowing mass at a constant rate which explains the lasting force signal on the front load cell. Since very limited granular mass ran over the load cell module, nearly zero force was imparted on both the shear and normal load cells in the rear.

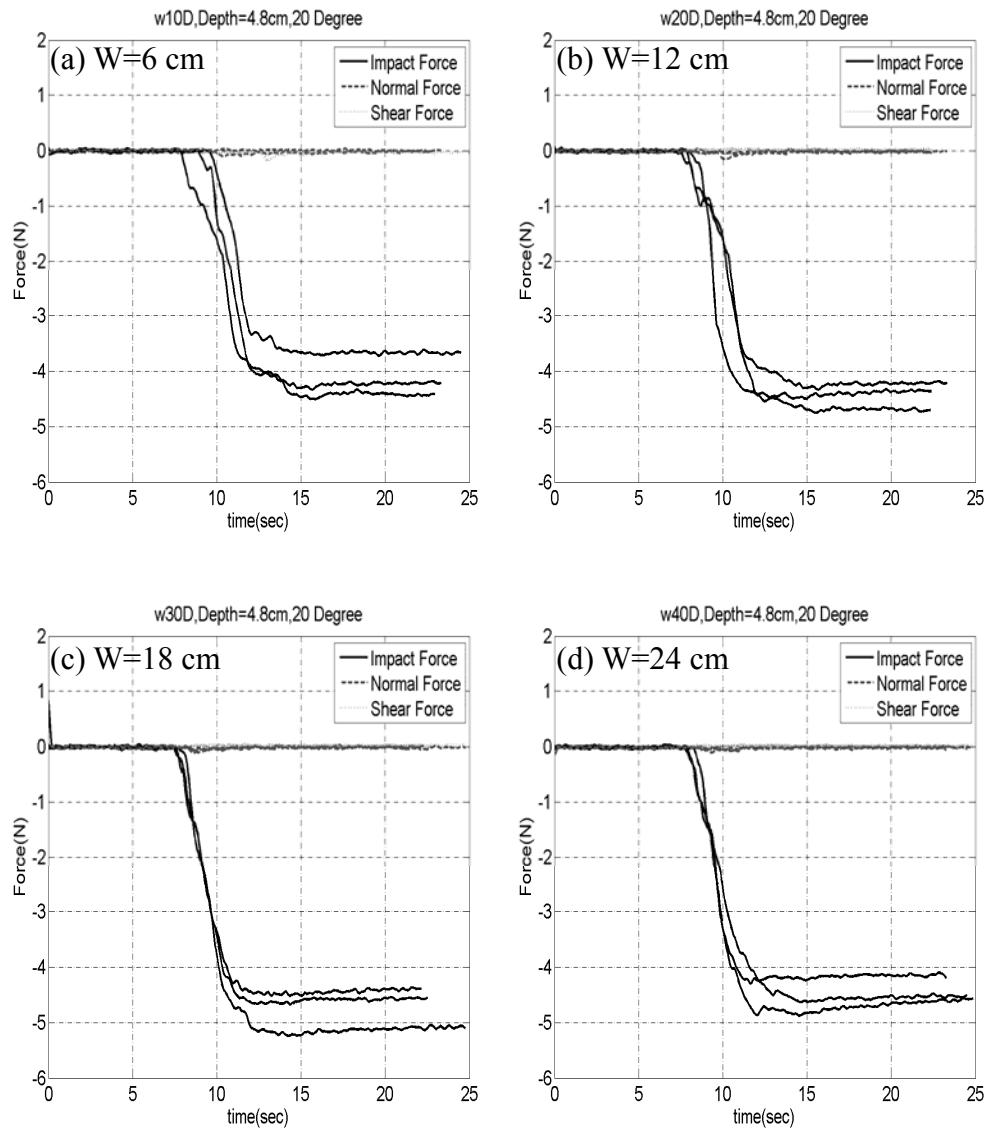


Figure 5.2 Force components on the load cell module for steady flows from four packing widths down a chute of 4.8 cm depth and 20° inclination: W=(a)6cm, (b)12cm, (c)18cm, and (d)24 cm with constant H=40cm.

We then added bed height to prepare a shallower chute of depth $h=2.4\text{cm}$ and the running spheres could climb over the load cell module but in a very random formation due to frequent rebounds. Upon impact, reflection pressure wave still developed and propagated upslope to stop the flowing mass. However, it is very interesting to observe that these arrested spheres formed two distinctive

configurations: one in orderly arrangement in figure 5.3(a) similar to a FCC structure but the other with a much looser and random packing in figure 5.3(b). Which to occur seems random from our finite number of experiments and we further found that the packing style has great influence on the flow rheology as described below.



Figure 5.3 Packing formation for the spheres arrested in front of the impact load cell for chute of 2.4 cm depth and 20° inclination: (a) close orderly packing and (b) loose and random packing.

When a close orderly packing was formed, the flowing granular mass climbed the load cell module only for a short duration since the reflection pressure wave arrested most of the flowing materials suppressing the climbing. In contrast, when the arrested materials were in random formation, the reflection pressure wave seemed to destroy the packing when the pile collapsed at some point. When the piled materials collapsed, the upcoming spheres had passage to cross the load cell module but such thin flow soon ceased when the pressure wave from the collapsed pile started to arrest

the flow again. Such “arrest-and-collapse and flow” cycle repeated until the arrested mass has accumulated to the reservoir gate. The intermittent and highly unsteady cross flows over the load cell module resulted in the spiky fluctuating signals on the front impact load cell (black-solid lines) in figures 5.4 (a) to (d). The signal when close orderly packing occurred is shown by the red-solid curve and they are much smoother for less flow over the load cell box. Note that the plateau measured on the impact load cell in figure 5.2 is no longer developed in the current flows partly due to the intermittent “arrest-and-collapse and flow” cycle in the black-solid lines in figure 5.4. As for why the red-line shows slow decay in force magnitude may result from some internal force distribution mechanism developed only in an orderly-packed bed which phenomenon is beyond the scope of this work. Such phenomenon that the arrested mass formed close orderly packing was only observed for the shallow chute ($h=2.4$ cm) at 20-degree inclination.

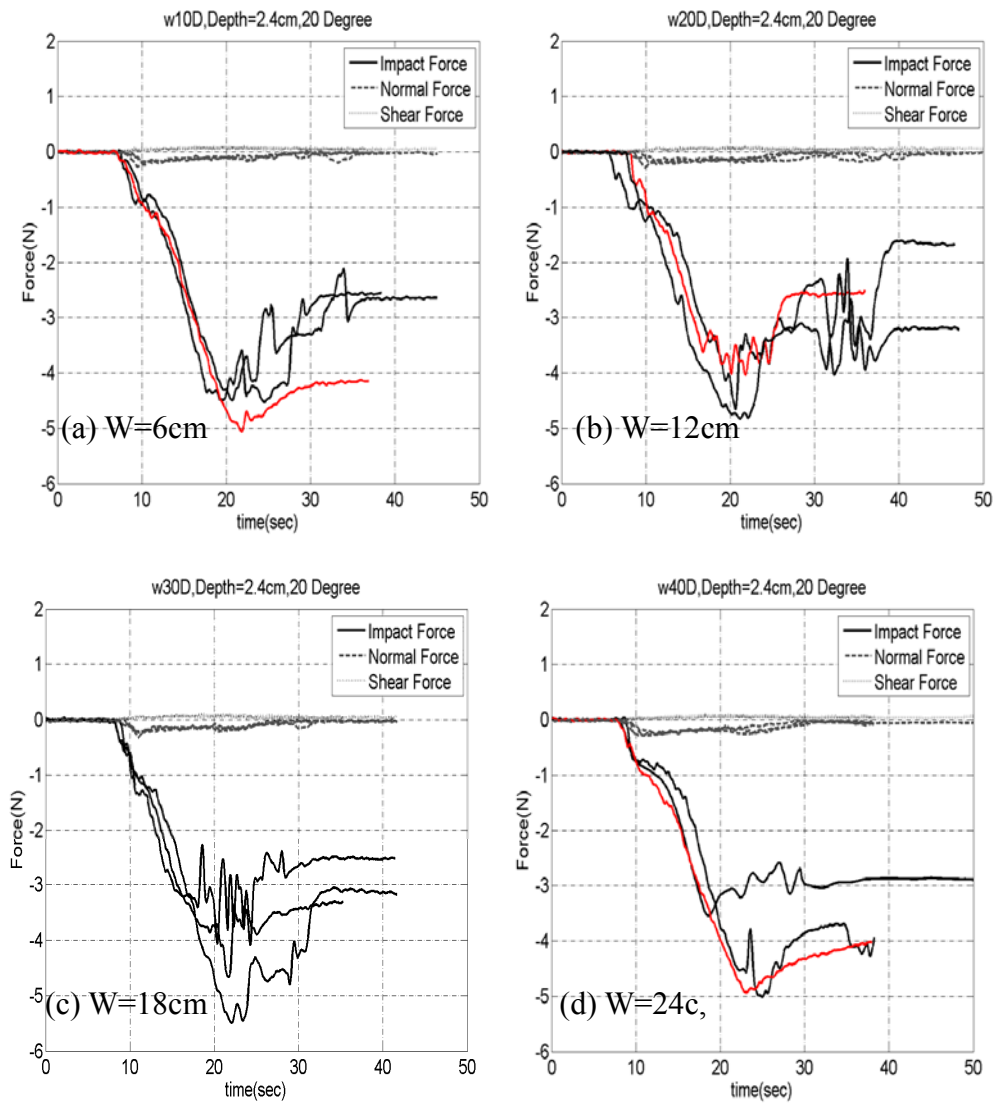
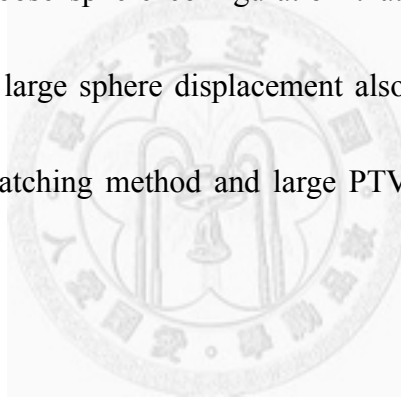


Figure 5.4 Force components on the load cell module for steady flows from four packing widths down a chute of height $h=2.4$ cm at $\theta=20^\circ$: $W =$ (a) 6cm, (b) 12cm, (c) 18cm, and (d) 24cm with constant $H=40$ cm.

At greater inclination angle, only random packing was observed and the signals obtained with $h=2.4$ cm and $\theta=23^\circ$ and 26° are shown in figure 5.5 and figure 5.6, respectively. For both θ , granular flows from the four packing geometries consistently crossed the load cell module giving lasting force signals. The impact and normal loading forces kept around 1N and 0.2N until a dramatic drop appeared later when the

discharge switched from steady to the decaying regime revealed in chapter 4. The shear loading, however, stayed nearly zero since the local sphere motions were fierce rebounds that stayed in contact with the sensing surface for too short a time to impart detectable tangential impulse. Though the rear normal load cell also experiences these random and fierce bouncing motions, it is the reverse of momentum component perpendicular to the load cell surface that accumulated into a larger total momentum change over time to give a detectable 0.2N force component. It is also such bouncing motion that results in a loose sphere configuration that invalidates the continuum assumption. The resulting large sphere displacement also degrades the effectiveness of the nearest neighbor matching method and large PTV errors occurred inevitably from time to time.



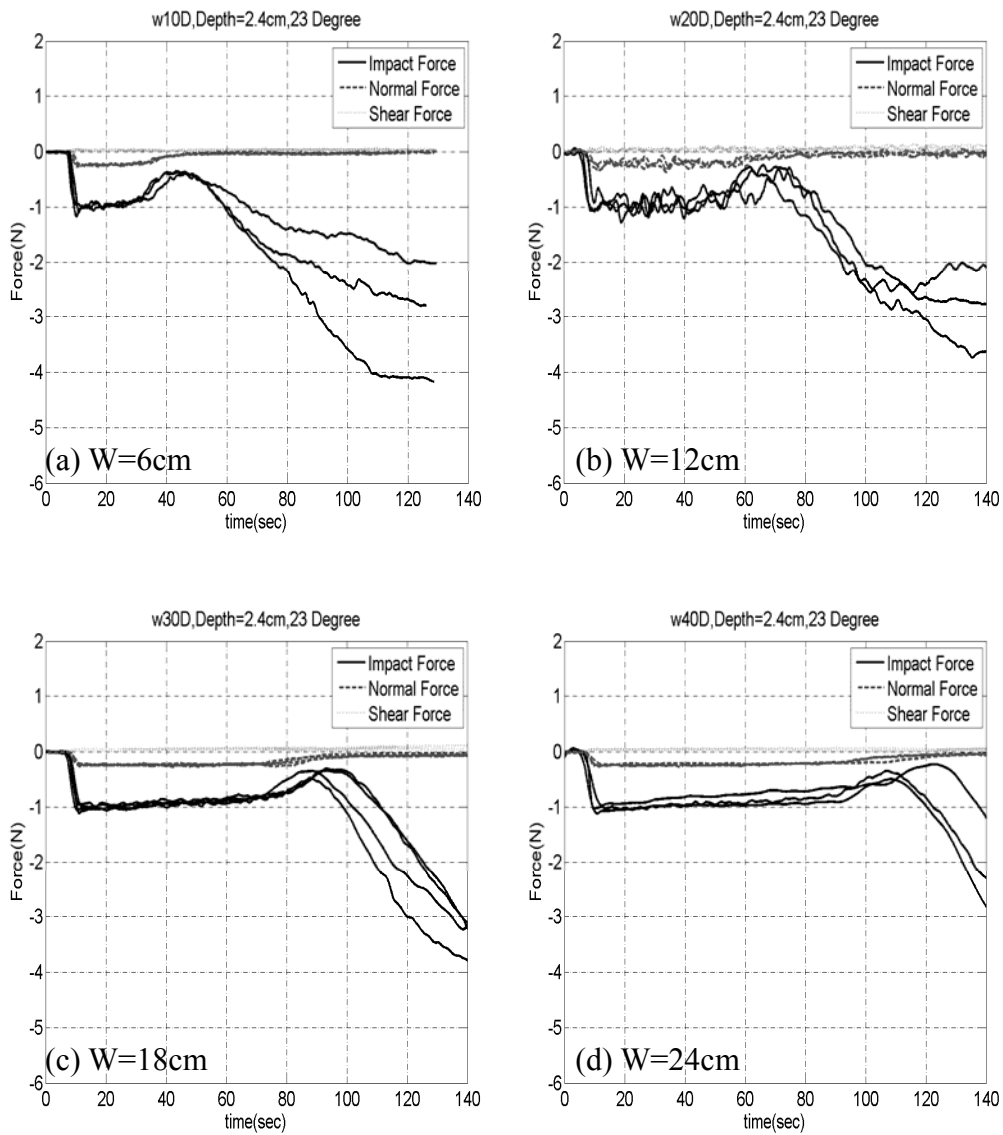


Figure 5.5 Force components on the load cell modules for steady flows from four packing widths down a chute of height $h=2.4\text{ cm}$ at $\theta=23^\circ$: $W =$ (a) 6cm, (b) 12cm, (c) 18cm, and (d) 24cm with constant $H=40\text{cm}$.

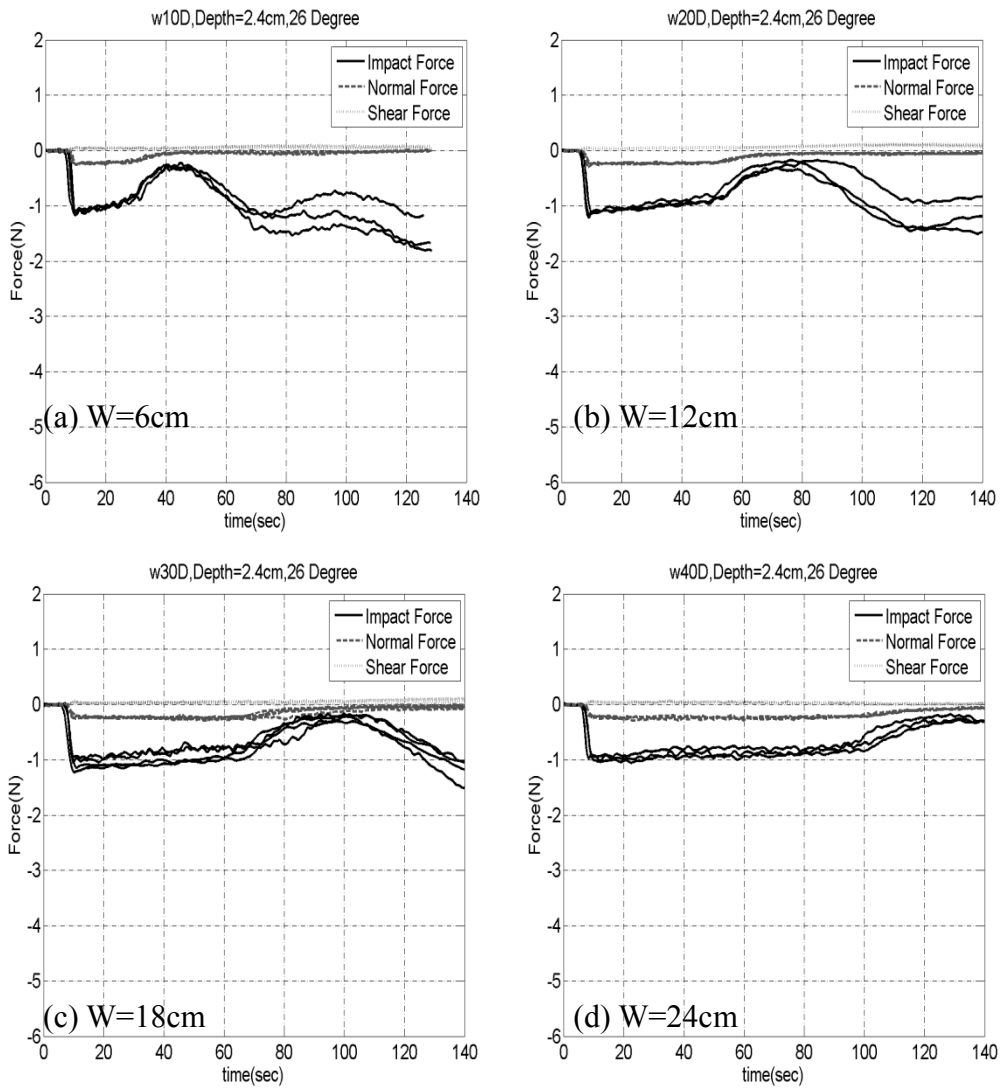


Figure 5.6 Force components on the load cell module for steady flows from four packing widths down a chute of height $h=2.4$ cm at $\theta=26^\circ$: $W =$ (a) 6cm, (b) 12cm, (c) 18cm, and (d) 24cm with constant $H=40$ cm.

Next, we examine the results obtained for thicker flows with $h=4.8$ cm using $\theta=23^\circ$ and 26° in figure 5.8 and figure 5.9, respectively. Steady flows still developed across the load cell module but now with a noticeable stationary zone of height around 7-9D in front of the impact plate as shown in a snapshot in figure 5.7. The crossing spheres formed a thin layer—with an averaged thickness around 3D—over

the shear and the normal load cells.

We first observe that the impact force for thick flows ($h=4.8\text{cm}$) down the chute at $\theta=23^\circ$ and 26° fell in the range of 5-7N which is comparable to that developed in flows of both depths on the 20° -chute. As shown in figures 5.2 and 5.4, the impact force for flows at $\theta=20^\circ$ with $h=4.8$ and 2.4cm are around 4-5N and 3-5N, respectively. However, when thin flows are generated down steeper chute at $\theta=23^\circ$ and 26° , the impact force drops dramatically to 1N. With image evidence, we know that stationary bulks accumulated in front of the impact load cell module in thick flows at the three inclination angle. Such static pile also developed in thin flows at $\theta=20^\circ$ (see figure 5.3). Thus, it is natural to speculate that it is these accumulated static spheres that give the 5N loading on the impact load cell. Both the increment of θ and reduction of flow depth h facilitated sphere motion across the load cell module and hence fewer spheres were arrested giving much smaller impact force. Further, it is also these facilitated sphere motions that reduced the internal friction between the flowing and the arrested mass. Hence the signals for the two thin and steeper flows are much smoother than those for thick flows or thin flows at mild angle in which strong dissipating interaction took place at the interface of moving and stationary bulks.

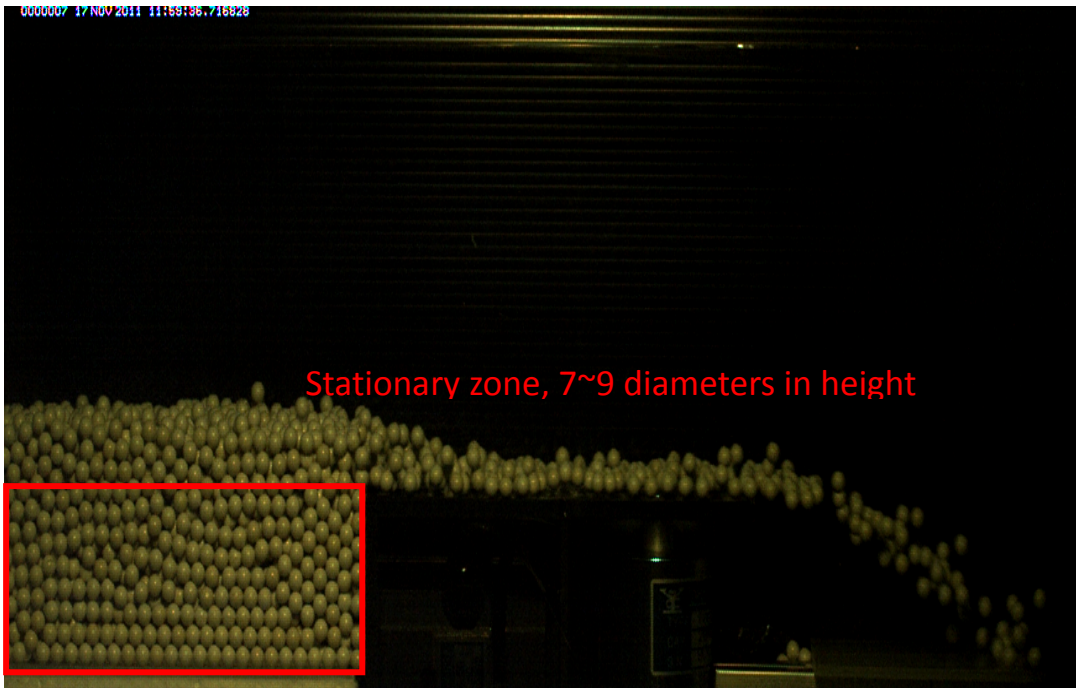


Figure 5.7 Stationary zone in front of the impact cell for chute of depth $h=4.8$ cm.

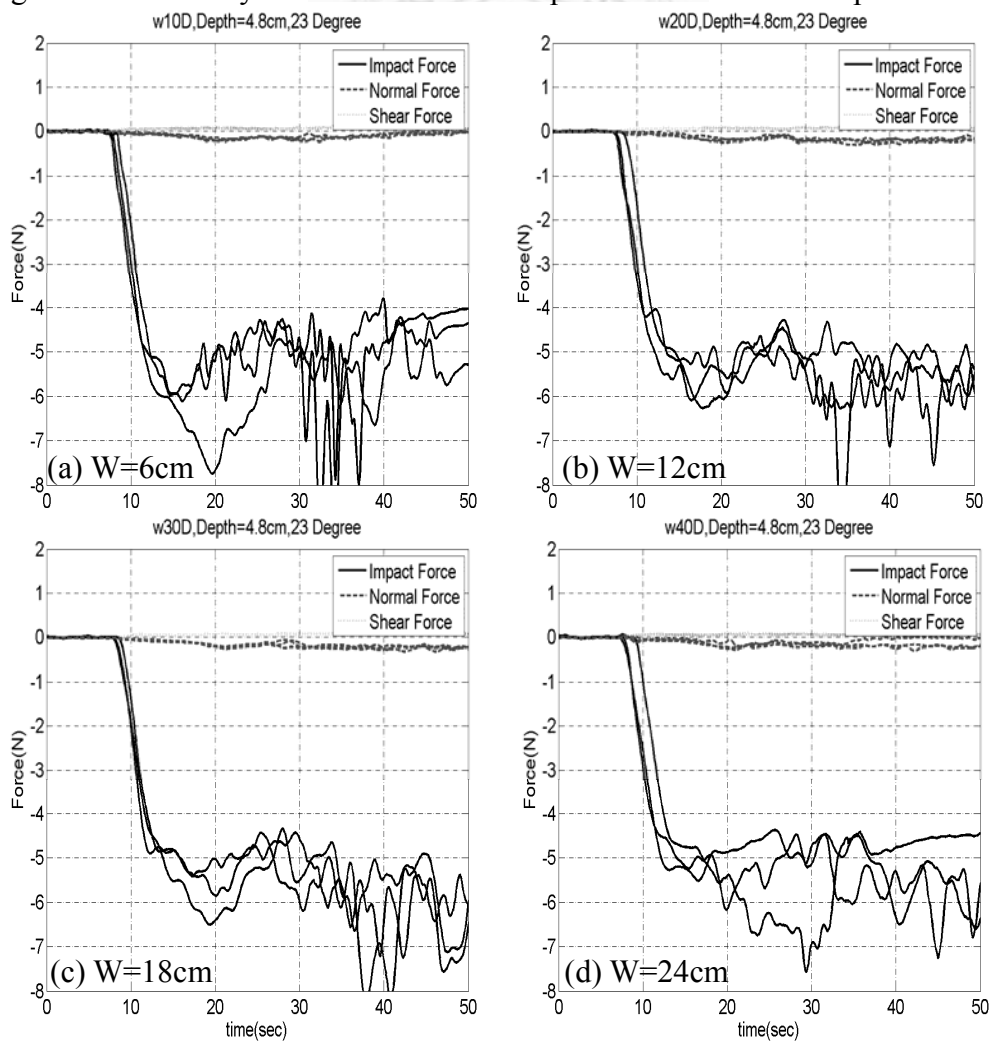


Figure 5.8 Force components on the load cell module for steady flows from four packing widths down a chute of height $h=4.8$ cm at $\theta=23^\circ$: $W =$ (a) 6cm, (b) 12cm, (c) 18cm, and (d) 24cm with constant $H=40$ cm.

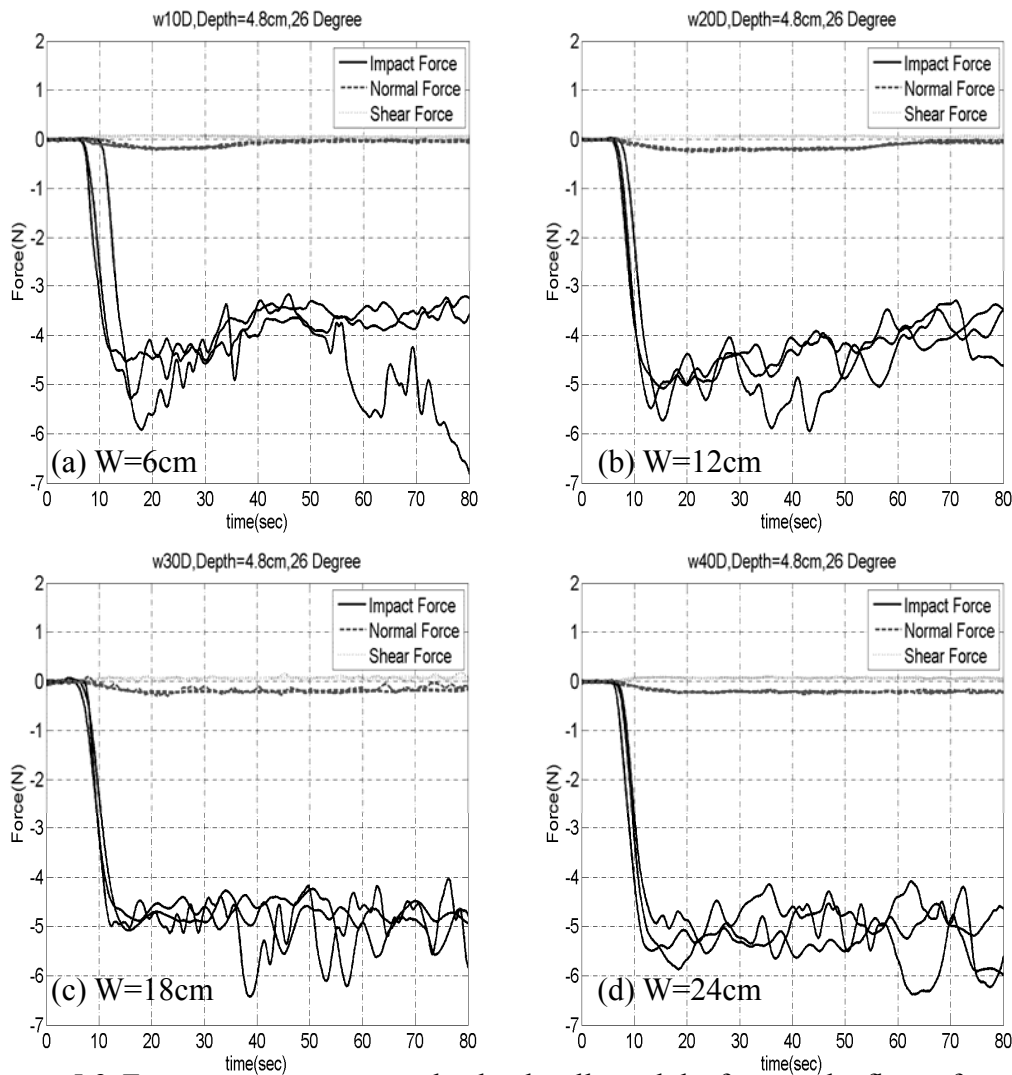


Figure 5.9 Force components on the load cell module for steady flows from four packing widths down a chute of height $h=4.8$ cm at $\theta=26^\circ$: $W =$ (a) 6cm, (b) 12cm, (c) 18cm, and (d) 24cm with constant $H=40$ cm.

The shear and normal loading forces for these flows are compared separately in figure 5.10 (a) and (b). Positive curves represent shear force data and negative ones are for the normal force measurements. Both force components show rapid increase of magnitude from time zero to a plateau that lasts for a duration increasing with W

during the development of steady flows. Since the packing mass was finite, the flow discharge rate eventually decayed to give decreasing force magnitudes and unsteady fluctuations. It is apparent that the duration of force plateau grows with the size of reservoir packing (W) but all at similar magnitudes: the shear and normal force plateau are slightly below 0.1N and around 0.2N, respectively. Finally, the normal force component on the steeper chute ($\theta=26^\circ$) is slightly smaller than that developed on the chute with $\theta=23^\circ$ due to the gravity component perpendicular to the chute scales with $\cos\theta$. Recall that granular flows down a chute at $\theta=20^\circ$ could not climb over the load cell box, nearly zero shear and normal forces were observed.

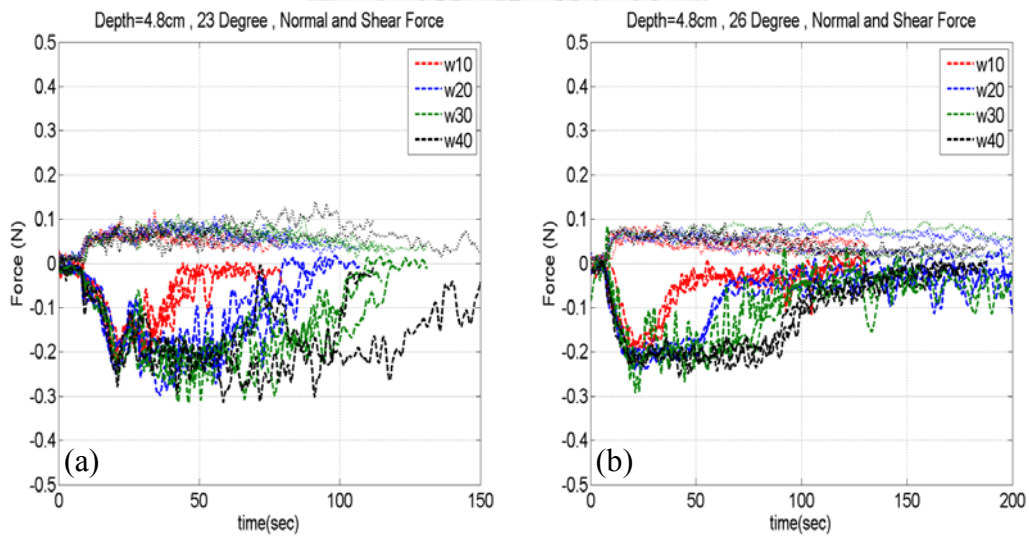


Figure 5.10 Shear and normal force components for steady flows down a chute of height $h=4.8$ cm at (a) $\theta=23^\circ$ and (b) $\theta=26^\circ$.

In the following section, we will perform two-dimensional control volume

analysis on the high-speed images to estimate the same three force components. The obtained results will be compared to the present in-situ three-dimensional force measurements to evaluate the feasibility of high-speed imaging technique in granular flow research.

5.3 Methodology of Image Analysis

In this section, we describe how we apply control volume analysis on the high-speed digital images to estimate the impact, the shear, and the normal load.

5.3.1 Force Measurements From Images: Control Volume Analysis and Reynolds

Transport Theorem

We first introduce Reynolds transport theorem and apply it in a control volume analysis on the acquired high-speed images assuming the bulk is continuum-like. A control volume CV at time t is defined by the blue box in a continuum in figure 5.11 and the enclosed control mass moves with the bulk and leaves the CV to a new location, marked by the red square, at a later time $t + \Delta t$.

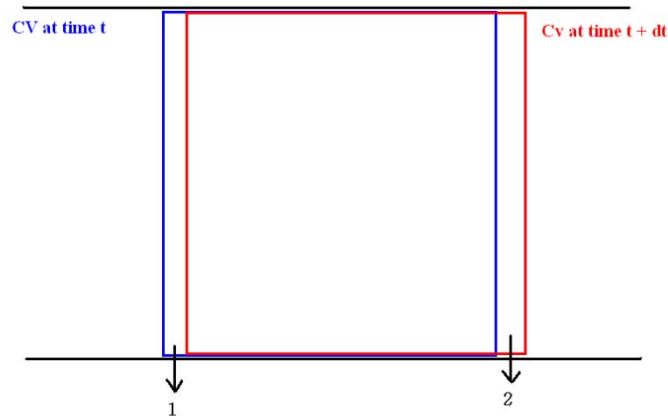


Figure 5.11 Control volume at two instants.

Let $B = mb$ represent some extensive property of the control mass within CV with m and b denoting the total mass and the corresponding intensive property. In integral form, we may express $B = \int_{CV} \rho b dV$, with ρ represents the continuum density field within a control volume. This extensive property of the control mass at time $t + \Delta t$ can be expressed as

$$B_{CM(t+\Delta t)} = B_{CV(t+\Delta t)} - B_{1(t+\Delta t)} + B_{2(t+\Delta t)} \quad (5.1-a)$$

where B_1 and B_2 denote the extensive property contained in area 1 and area 2 left out from and included to a CV as the continuum moves. The time rate change of the extensive property of the control mass can be expressed as

$$\frac{\Delta B_{CM}}{\Delta t} = \frac{B_{CM(t+\Delta t)} - B_{CM(t)}}{\Delta t} = \frac{B_{CV(t+\Delta t)} - B_{1(t+\Delta t)} + B_{2(t+\Delta t)} - B_{CM(t)}}{\Delta t} \quad (5.1-b)$$

Let the control mass coincide with the control volume at time t , giving $B_{CM(t)} = B_{CV(t)}$.

Equation (5.1-b) can be manipulated into

$$\frac{\Delta B_{CM}}{\Delta t} = \frac{\Delta B_{CV}}{\Delta t} - \frac{B_{1(t+\Delta t)}}{\Delta t} + \frac{B_{2(t+\Delta t)}}{\Delta t} \quad (5.1-c)$$

Let $\Delta t \rightarrow 0$, we obtain

$$\frac{DB_{CM}}{Dt} = \frac{dB_{CV}}{dt} - \lim_{\Delta t \rightarrow 0} \frac{B_{1(t+\Delta t)}}{\Delta t} + \lim_{\Delta t \rightarrow 0} \frac{B_{2(t+\Delta t)}}{\Delta t} \quad (5.1-d)$$

in which D/Dt represents the material derivative. If we transform this differential

form into an integral form, we get

$$\frac{DB_{CM}}{Dt} = \frac{d}{dt} \int \rho b dV - \dot{B}_{in} + \dot{B}_{out} \quad (5.1-e)$$

where \dot{B}_{in} and \dot{B}_{out} represent the time rate of change of this extensive property

entering and leaving the control volume. Equation (5.1-e) states that the time rate

change of extensive property for a moving control mass is equal to the time rate

change of the extensive property within the control volume—thus the volume

integral—plus the net flux of the extensive property through the control volume

bounding surface. Now, we use $B=mU$ to represent the streamwise momentum of a

control mass that coincides with CV at one moment with U denoting the velocity

component parallel to the chute base and m is mass. The time rate change of the total

x-momentum of a control mass can be then be expressed as

$$\frac{D(mU)}{Dt} = \frac{d}{dt} \int \rho U dV - \int \rho_1 U_1 U_1 dA_1 + \int \rho_2 U_2 U_2 dA_2 = F_{surface} + F_{body} \quad (5.2)$$

with A_1 and A_2 representing the cross section areas perpendicular to U . We then

equate the the time rate change of the streamwise momentum of a control mass to the

sum of body force and surface force according to Newton's second law.

To apply such control volume formula to analyze the current experimental images, we chose two control volumes next to the front and the rear load cell boxes as shaded in figure 5.12. The first, CV1, is defined on top of the rear load cell box with its free surface extends above all the flowing material. The second, CV2, is defined in front of the front load cell box with a streamwise span of $35D$ (D being the sphere diameter) which is limited by our CCD size at the required spatial and temporal resolution.

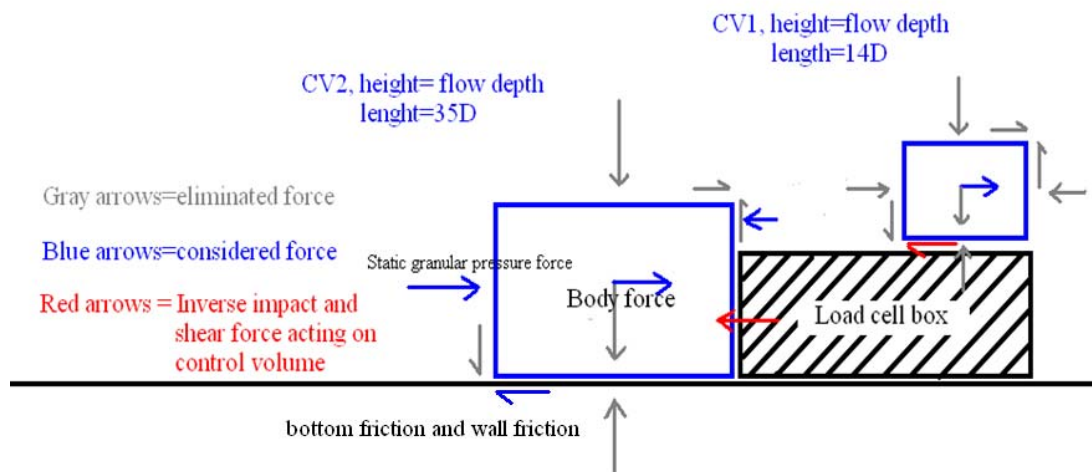


Figure 5.12 Two control volumes, CV1 and CV2, defined for control volume analysis on the flow images.

We simplified the surface force components based on a few flow conditions observed in our experiments. First, we assume that the static granular pressure is hydrostatic and can be described by egh . For CV1 on the rear load cell, there is no friction and normal force on the top control surface since no material crosses this bounding surface. Since the flow over the rear load cell is very thin and loose, it is

reasonable to expect nearly zero bulk motion perpendicular to the chute base (y-direction) and hence friction force resulted along the right and the left vertical control surfaces is negligible. Though hydrostatic pressure also results in normal forces on these two bounding surfaces, the thin and loose flow conditions on both sides allow us to ignore static granular pressure streamwise variation. For CV2, forces on the top control surface were ignored for the same reasons applied to CV1. We assume that the friction coefficient between the bulk and the boundary is uniform and has the same value for the wall and the base since these bounding surfaces are all made by acrylic. We further assumed an isotropic hydrostatic granular pressure to describe the friction force by multiplying the friction coefficient with effective normal granular pressure. We also neglect static granular pressure force on right vertical control surface because its flow depth was much thinner than that on the left surface. The reaction force from the front load cell box exerts another surface force on CV2 as sketched by the red arrows. In addition to surface forces, the blue arrow in each CV represents the corresponding gravity force component parallel and perpendicular to the chute base.

We now turn to describe how the impact force on the front load cell box can be estimated from a control volume analysis on CV2 using the conservation of streamwise (x-) momentum. Recall the impact force, F_I , is treated as a surface force

on the right control surface, manipulation of equation (5.2) gives

$$F_1 = \frac{d}{dt} \int \phi \rho_s U dV - W \int_0^h \rho_s U_1 U_1 dy + W \int_0^h \rho_s U_2 U_2 dy - \rho_s W h g \sin \theta \int_0^h \phi_1 dy - \rho_s \phi g V \sin \theta - \mu \rho_s g W \cos \theta \int \int \phi dx dz - 2 \mu \rho_s g \cos \theta \int \int \phi (h - z) dx dz \quad (5.3-a)$$

In this expression, ρ_s represents the sphere density, V represents the volume of whole CV, W stands for chute width, ϕ and U are the bulk solid volume fraction and velocity estimated by 2D lateral images. The subscripts 1 and 2 indicate the local values evaluated at the left or the right control surface, respectively. Hence, $\int dA_1$ and $\int dA_2$ execute surface integrals on the left and the right control surfaces. Similarly, control volume analysis of the x-momentum in CV1 gives the shear loading force, F_s ,

$$F_s = \frac{d}{dt} \int \phi \rho_s U dV - W \int_0^h \rho_s U_1 U_1 dy + W \int_0^h \rho_s U_2 U_2 dy - \rho_s \phi g V \sin \theta \quad (5.3-b)$$

Conservation of y – momentum in CV1 gives the normal loading force on the rear load cell box as

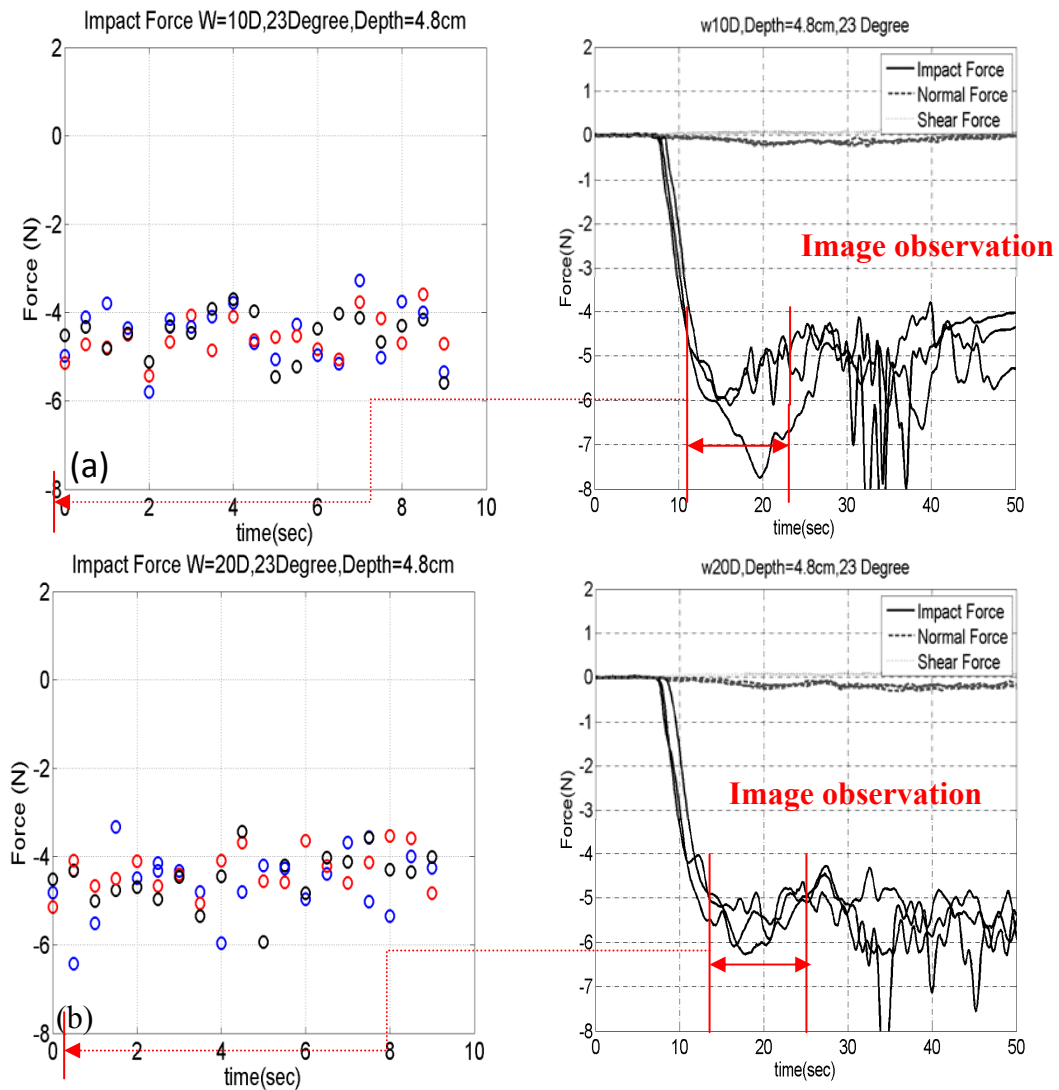
$$F_N = \rho_s \phi V g \cos \theta \quad (5.3-c)$$

5.4 Comparison of Force Data from Load-Cell and Control Volume Analysis of Images

We have introduced how we could estimate a force component from control volume analysis on the granular flow information derived from image-based PTV and area-weighting space average. This analysis relies on lateral imaging from the chute side and thus is a two-dimensional estimation. It is undoubtedly desired to examine how these results compare to the in-situ three-dimensional force data from the load cells. Note that the control volume analysis is two-dimensional, the obtained value was multiplied by the chute width to estimate a 3D force component as that sensed by the load cell.

Figure 5.13(a)-(d) are prepared for the data obtained for dry flows from different reservoir packing widths down the chute of height $h=4.8$ cm at 23° . The left subfigure shows the impact force from the control volume analysis (after multiplication with the chute width) and the load-cell measurement is presented on the right. Limited by the camera memory, we only recorded sphere motions when the corresponding load-cell signal has reached the plateau on its temporal profile. To achieve this, we first conducted several measurements on the load cell and used their collective profiles, as that shown in the right subfigure of figure 5.13, to decide when to record the flow after the gate was opened. For example, for the case examined in

figure 5.13(a), the flow hit the load cell roughly 8 seconds from gate opening and a force plateau was observed after 10 seconds. Thus, we started recording flow images from 10 to 20 seconds and this duration is marked here on the load-cell temporal profile by the two vertical red lines. Three experiments were recorded and analyzed for each flow and all results from the control volume analysis are shown by different colors in the left subfigure.



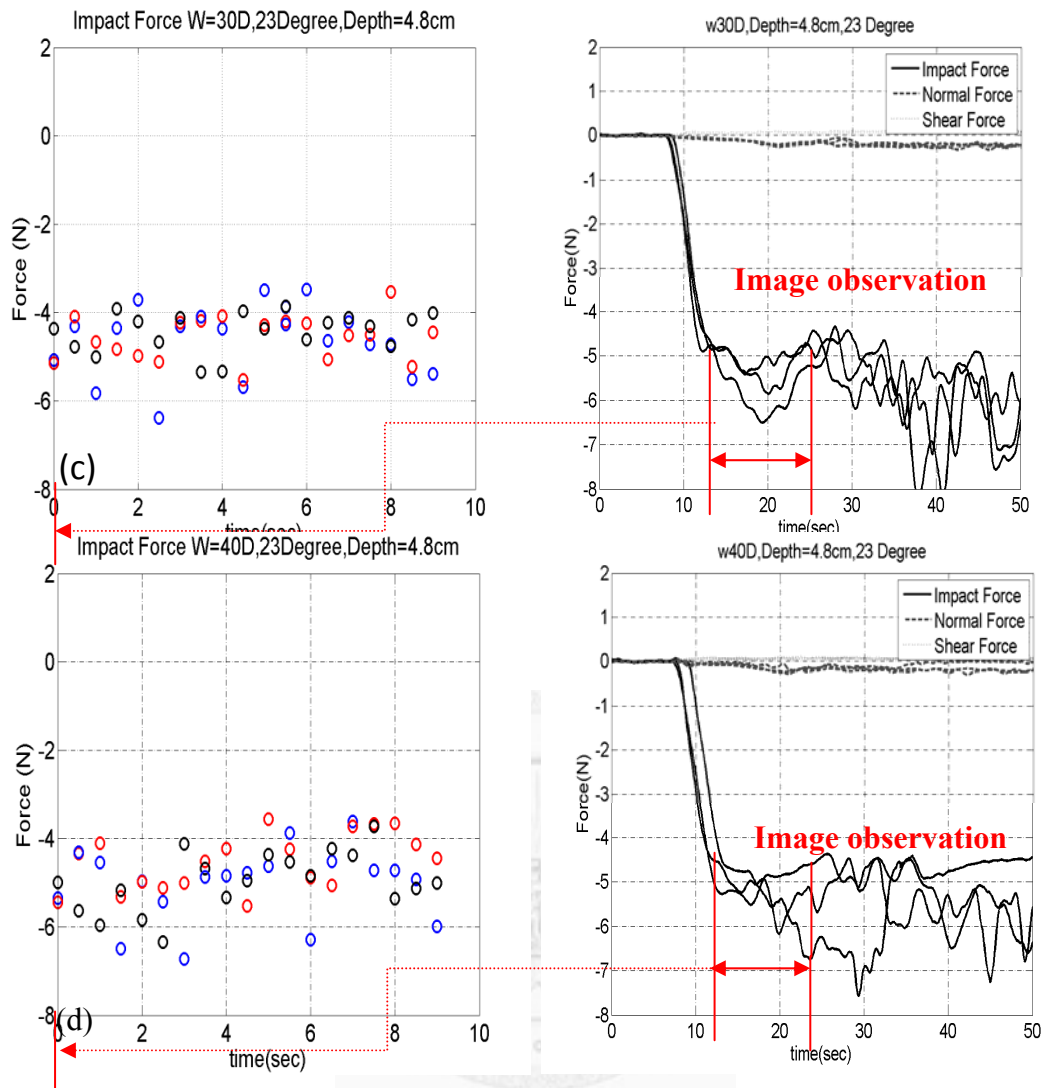
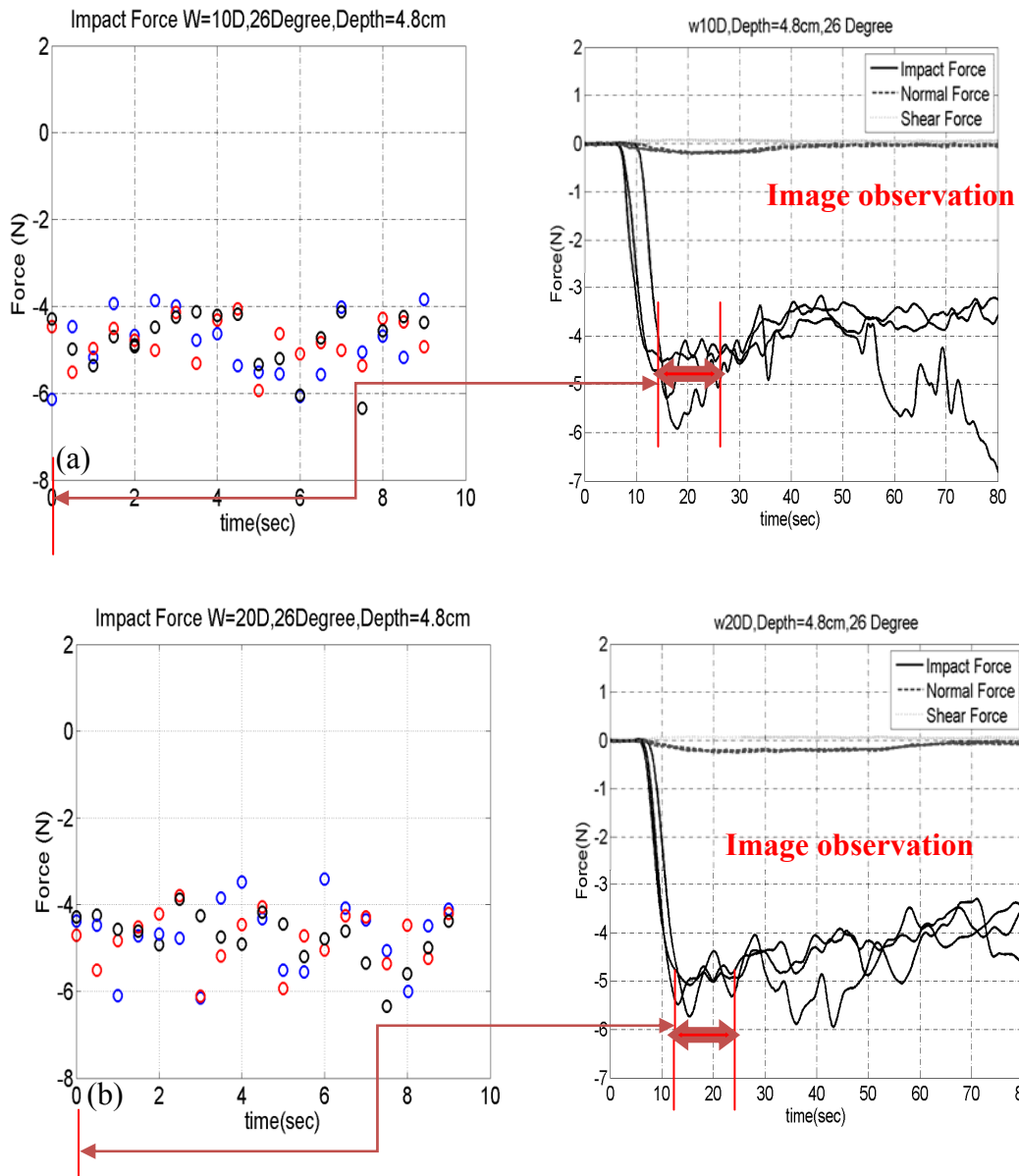


Figure 5.13 Comparison of impact force obtained from the control volume analysis (left) and in-situ load cell measurement (right) for flows from different packing widths $W =$ (a) 6cm, (b) 12cm, (c) 18cm, and (d) 24cm with identical $H = 40$ cm. The chute depth and angles are $h = 4.8$ cm and $\theta = 23^\circ$.

Similarly, the other sets of comparison was prepared in figure 5.14 (a)-(d) for flow impacts on the chute at 26° . Good agreement is obtained for all the steady flows giving impact force magnitude around 5N, independent of the chute angle and reservoir packing geometries. Careful examination also reveals that the two-dimensional control volume analysis estimates an impact force slightly smaller

than the in-situ load cell measurements. Such slight underestimation may be attributed to momentum flux variation across the chute width due to non-uniform velocity or density profiles. However, such 3D flow information is beyond the capability of lateral imaging since the material is opaque.



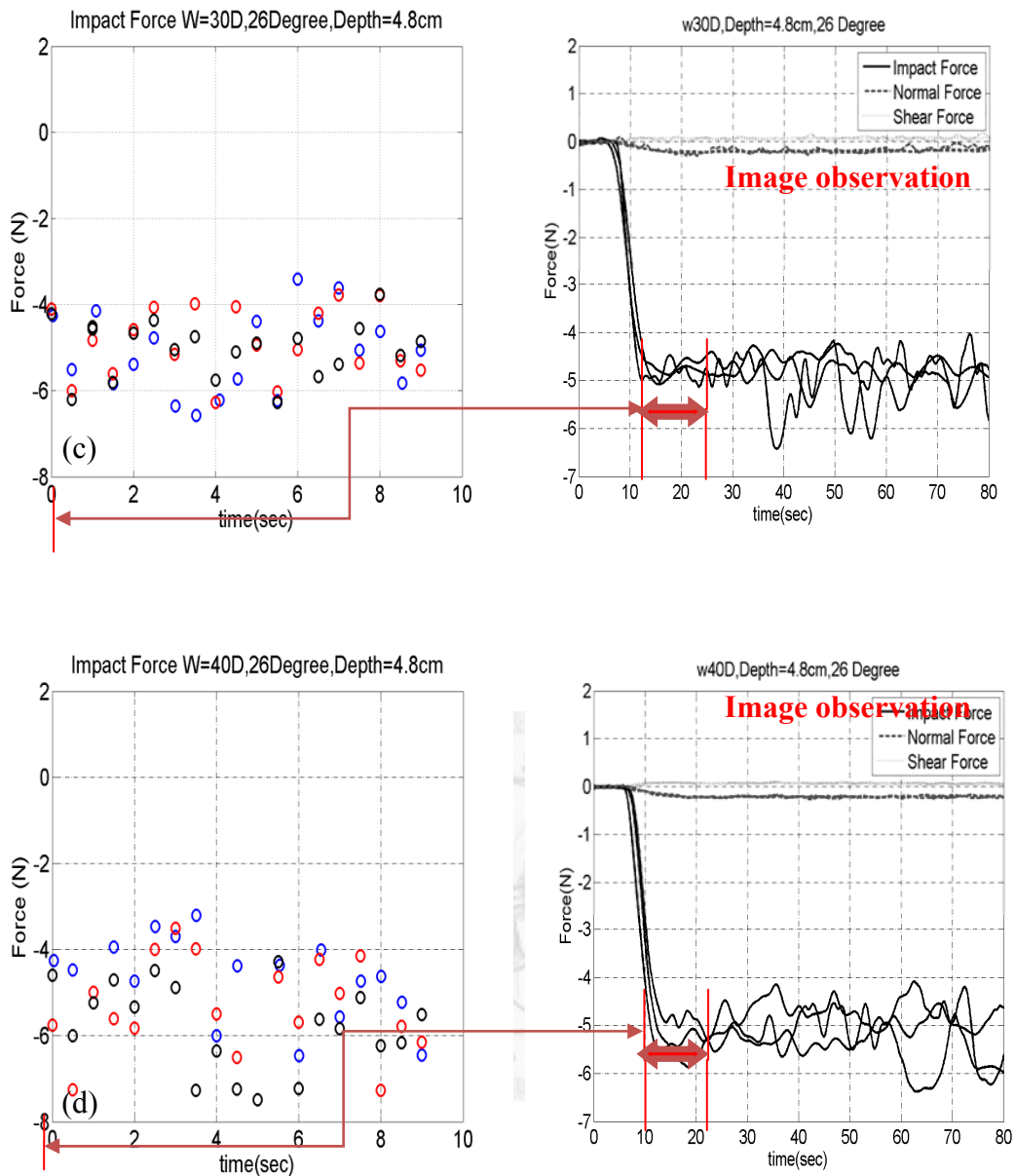
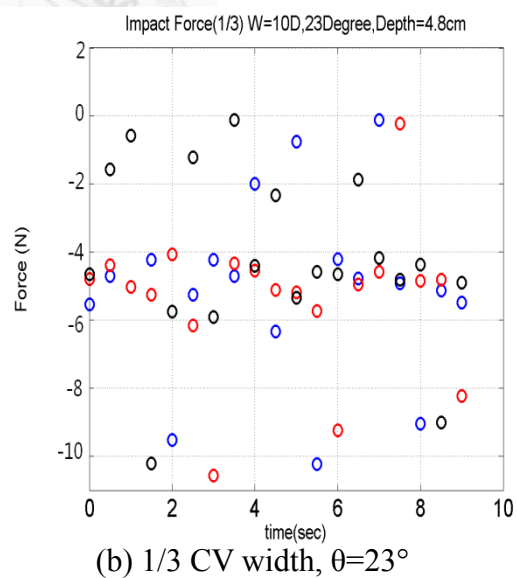
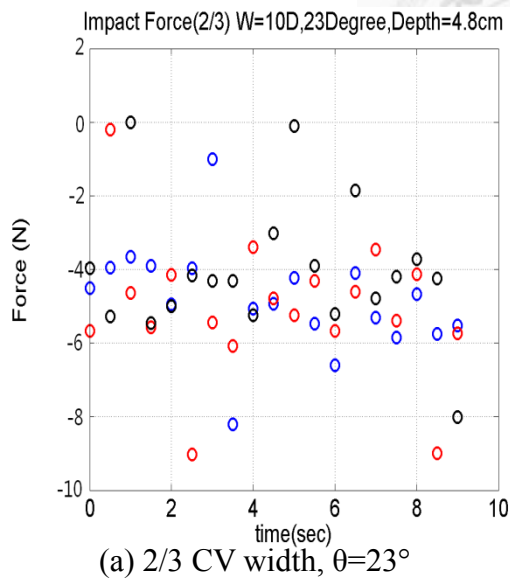


Figure 5.14 Comparison of impact force obtained from control volume analysis (left) and in-situ load cell measurement (right) for a dry granular flow from different reservoir packings $H=40$ cm, $W=$ (a) 6cm, (b) 12cm, (c) 18cm, and (d) 24cm down a chute of $h=4.8$ cm and $\theta=26^\circ$.

It is natural to suspect the results from the current control volume analysis may change with the control volume size. We then divided the initial control volume into 1/3 and 2/3 of its original streamwise length (35D shown in figure 5.7) and examine the corresponding results. The impact force obtained for flows from the narrowest

packing ($W=6\text{cm}$) is firstly examined in figure 5.15. Those obtained for flows at $\theta=23^\circ$ using 2/3 and 1/3-wide control volume are shown in figure 5.15(a) and (b) and compared to the data shown in the subfigure of 5.13(a) using the whole control volume width. All the measured impact force fluctuates primarily between 5.72 and 6.72N but more and more fluctuating data are observed when the control volume width is reduced. Similarly, when the impact force for the steeper flows at $\theta=26^\circ$ is compared in the left subfigure of 5.14(a) and figures 5.15(c) and (d), the data again fluctuate about a mean around 6.04-7.04N but with larger variations for shorter CV.



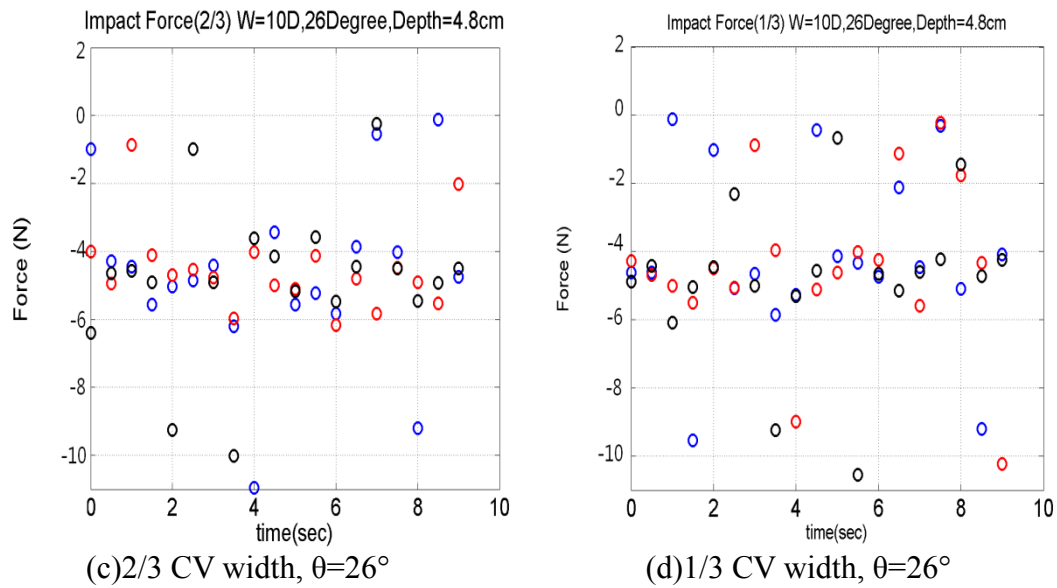


Figure 5.15 Comparison of impact force using control volume of 2/3- and 1/3-original width for dry flows from the narrowest packing ($W=6\text{cm}$) down the chute at (a)-(b): $\theta=23^\circ$ and (c)-(d): $\theta=26^\circ$. The data with 2/3 CV width is shown first for each inclination.

We suspected the fluctuations to result from matching the wrong spheres in the nearest neighbor method giving erroneous PTV results. From the experimental picture shown in figure 5.7, we report a stationary zone piled in front of the load cell module on which a very thin surface flow, of only 3~4-diameter thick developed. It is the time rate change of streamwise momentum of these moving spheres that contributes to the current impact force and thus the errors from PTV thus can affect our control volume analysis result as we shorten the CV streamwise length. For such rapid surface flows, large voids formed in the flow and the spheres moving outside of the layer adjacent to the chute lateral wall may still be captured through the voids in the wall layer. Therefore, a sphere adjacent to the chute wall at time t may be matched with a sphere

emerging from the ‘inner layers’ at $t + \Delta t$ giving erroneous PTV results. To resolve these PTV errors, we manually traced the spheres adjacent to the chute wall for six consecutive images of interval 1/600 seconds to obtain manual PTV results for each sphere at five moments. These resulted in five bulk velocities at consecutive times and we calculated the mean for the use in the momentum balance equation to recalculate the impact force, F_1 . The resulted F_1 for the two flows at $\theta=23^\circ$ and 26° using 1/3 CV width are shown in figure 5.16 with the corresponding standard deviation (from temporal average). Noticeable improvement on data conformity is observed as compared to those shown in figures 5.15.

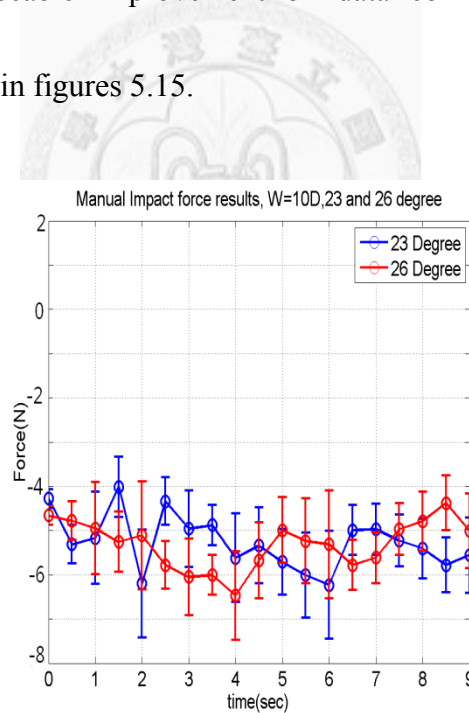
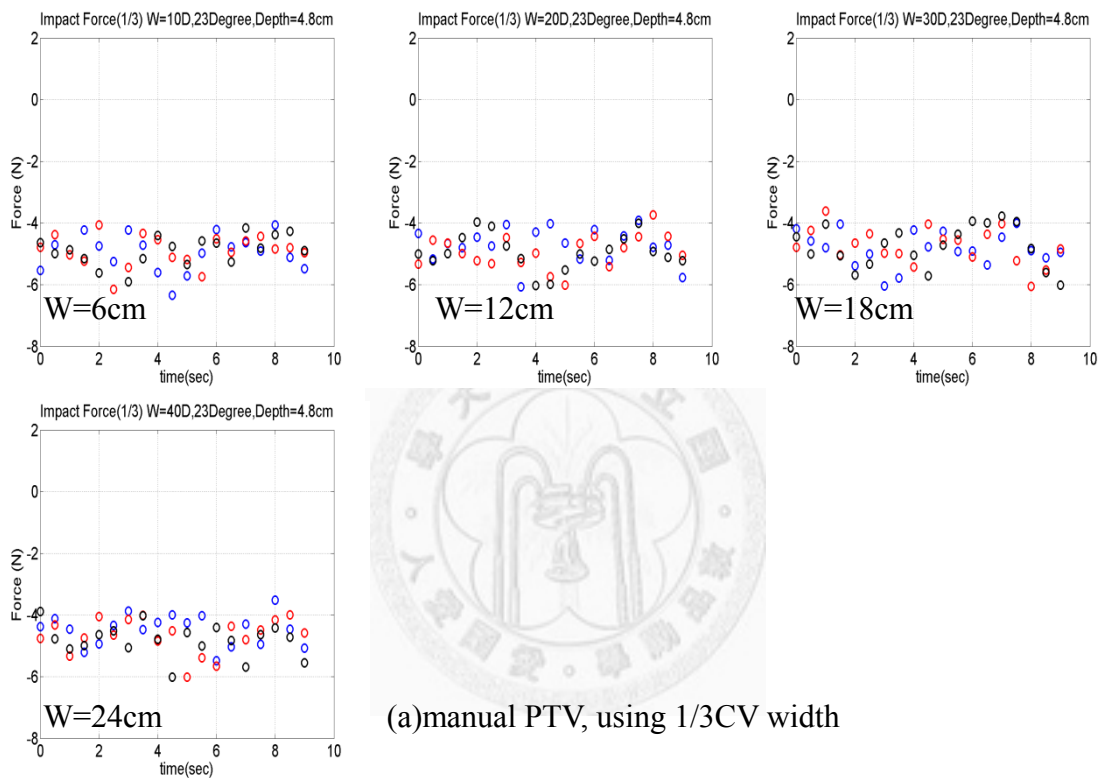


Figure 5.16 Impact force using manual PTV results in the control volume analysis using 1/3 width of the original length for flows from the narrowest packing, $W=6\text{cm}$, at $\theta=23^\circ$ (red) and 26° (blue). Here shows the mean of five consecutive data using 1/600 seconds interval with the corresponding standard deviation.

We then applied such manual PTV to all the other experiments using 2/3 and 1/3 CV width and the obtained impact force for the flows at $\theta=23^\circ$ and 26° from different packing widths are shown in figures 5.17 and 5.18, respectively. The data with 2/3 and 1/3 CV width are separated in subfigures (a) and (b).



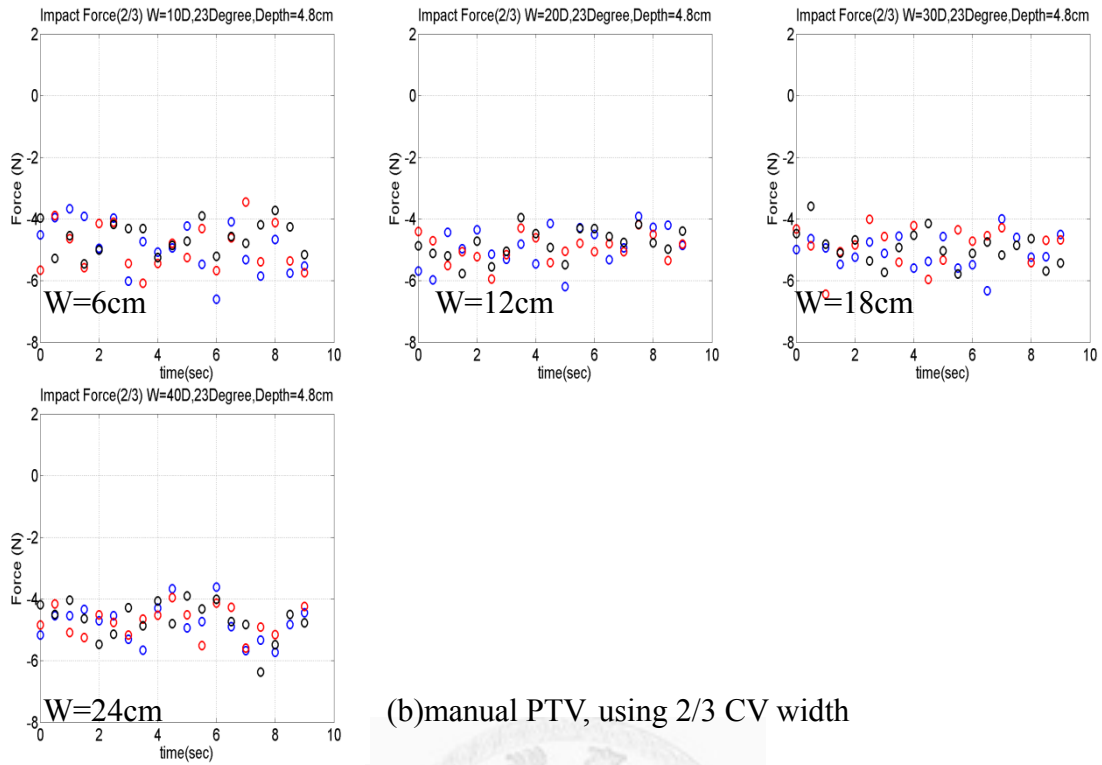
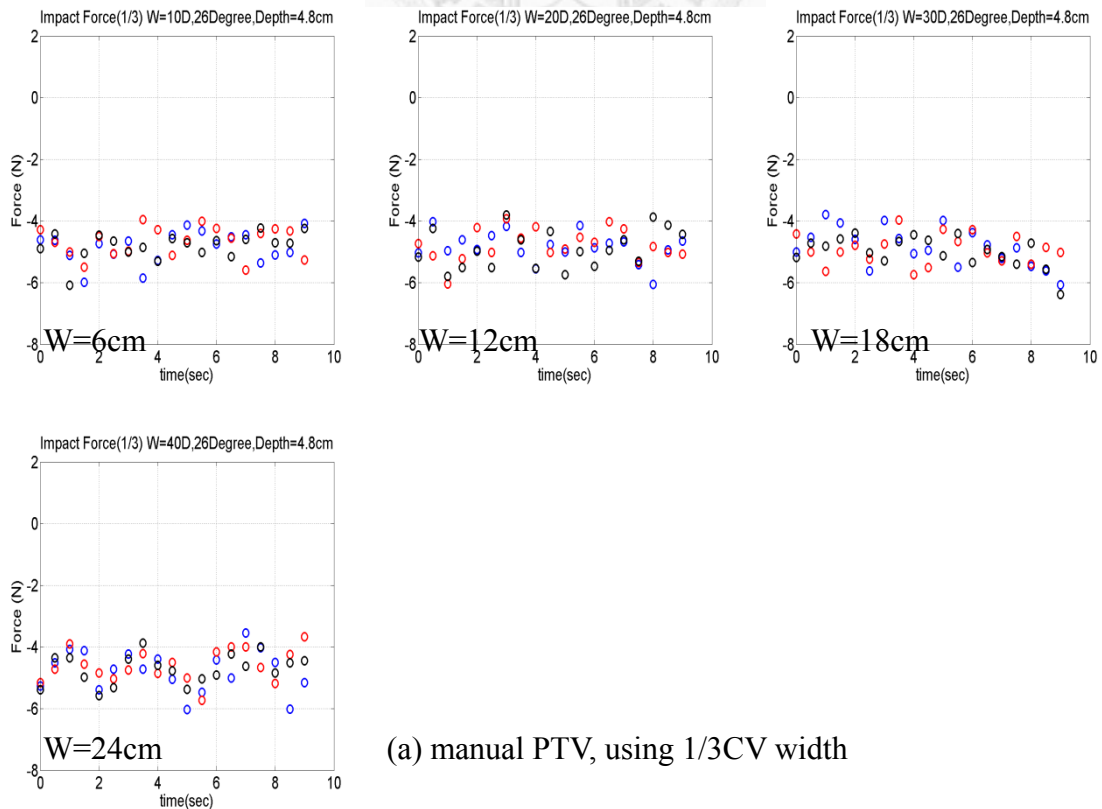
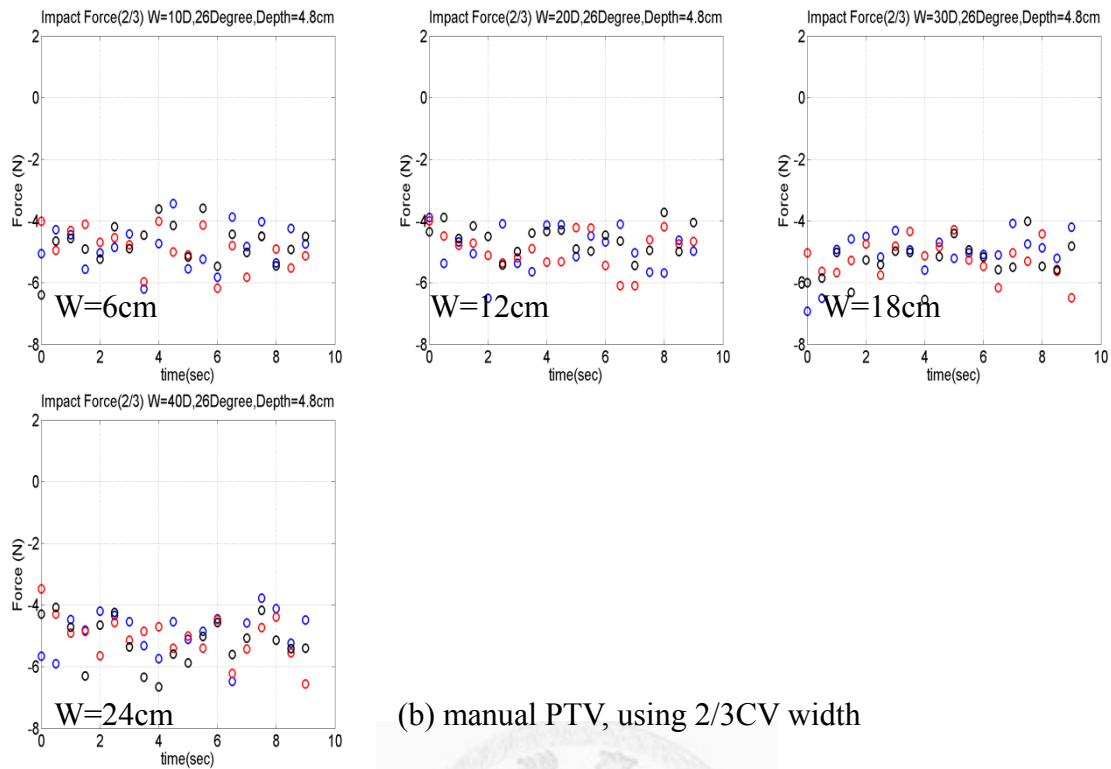


Figure 5.17 Impact force using manual PTV data for flows at $\theta=23^\circ$ from different packing widths with constant $H=40\text{cm}$. Control volume analysis using 1/3 and 2/3 CV width are shown separately in (a) and (b).





(b) manual PTV, using 2/3CV width

Figure 5.18 Impact force using manual PTV data for flows at $\theta=26^\circ$ from different packing widths with constant $H=40\text{cm}$. Control volume analysis using 1/3 and 2/3 CV width are shown separately in (a) and (b).

Next, we examine the shear and normal force loads estimated from the second control volume, CV2, atop of the rear load cell box (see fig 5.12) using the same observation duration as that adopted for the impact force estimation. Considering that the load cell sensing surface only occupies half chute width, the force magnitude is multiplied by two to obtain a load across the chute width.

We first show the data for flows down the chute with $h=4.8\text{ cm}$ and inclination at $\theta=23^\circ$ in figure 5.19, where the circle (negative) and the cross (positive) data are for the shear and the normal components. For the normal load, the in-situ load cell gives a plateau around $0.2\sim 0.3\text{N}$, (see figure 5.10(a)) and multiplication by two gives

a load of 0.4~0.6N that agrees well with the current control volume analysis. For all the four reservoir packing. We also compare the shear and normal loads for flows down a steeper chute at $\theta=26^\circ$ but the same height ($h=4.8$ cm) in figure 5.20. The normal loading obtained from the control volume analysis is again compared well to the load cell data—two times of that shown in figure 5.10(b).

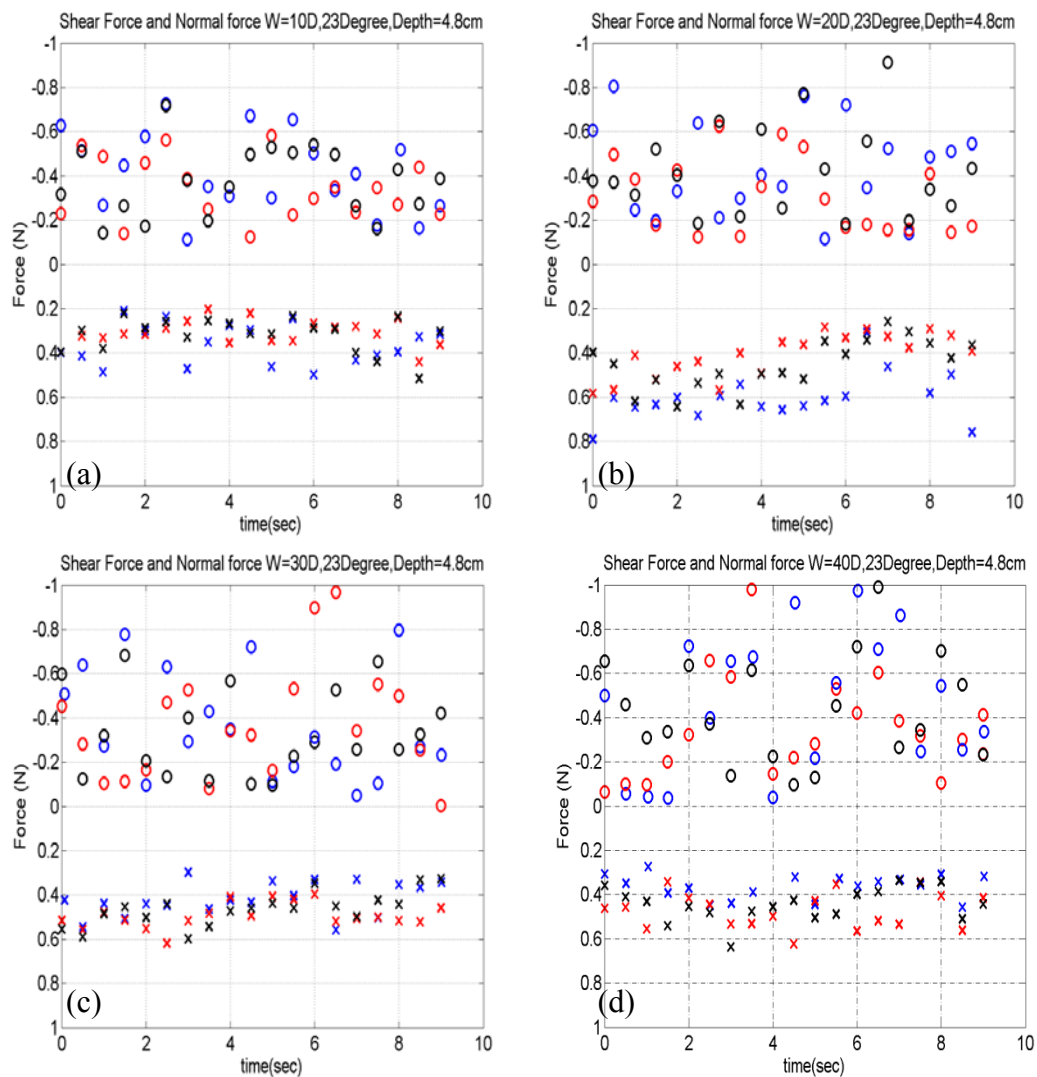


Figure 5.19 Normal (x) and shear (o) force obtained from control volume analysis for dry granular flows down a chute of $h=4.8$ cm and $\theta=23^\circ$ from different reservoir packing widths with constant $H=40$ cm: $W=$ (a) 6cm, (b) 12cm, (c) 18cm, and (d) 24cm.

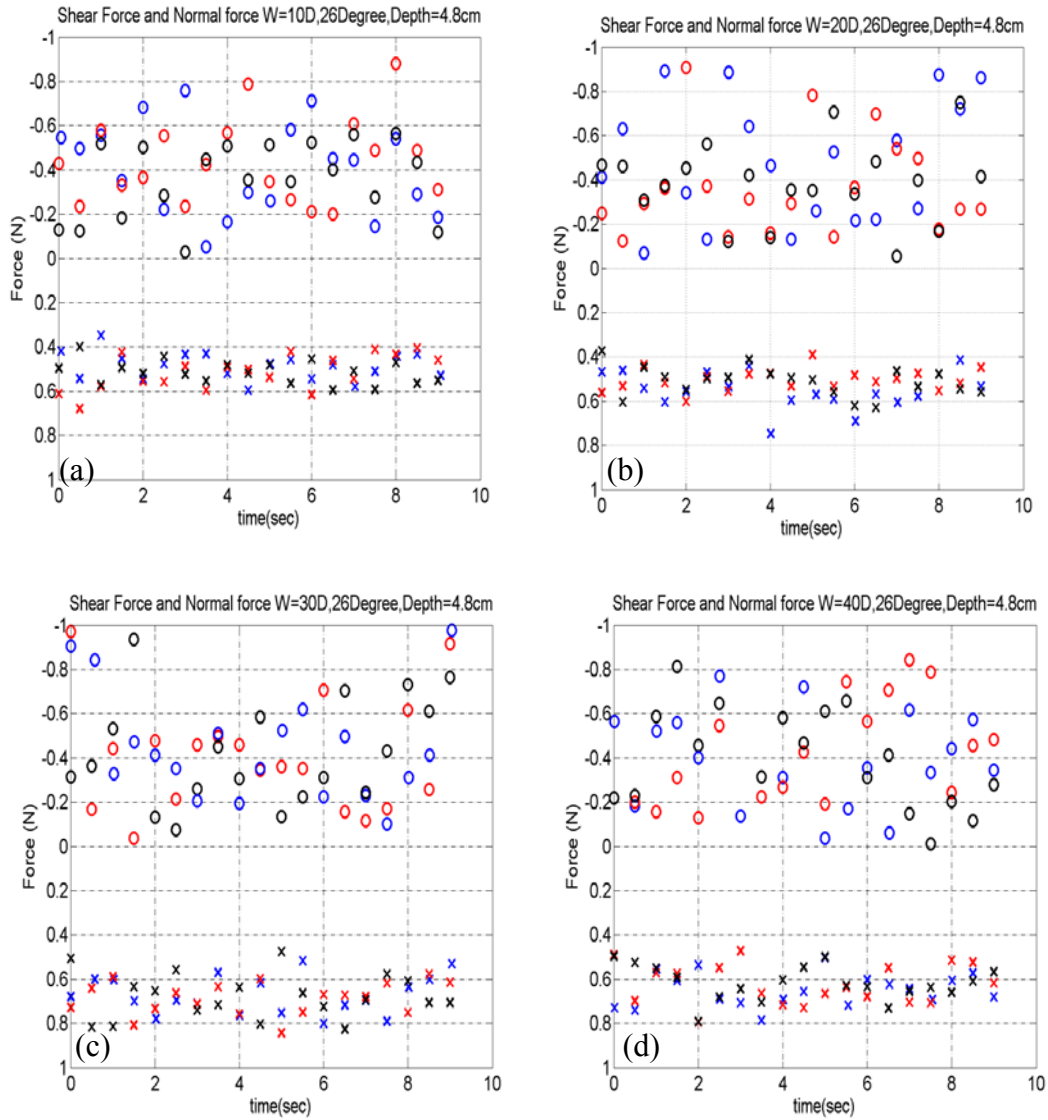


Figure 5.20 Normal (x) and shear (o) force obtained from control volume analysis for dry granular flows down a chute of $h=4.8$ cm and $\theta=26^\circ$ from different reservoir packing widths with constant $H=40$ cm: $W=$ (a) 6cm, (b) 12cm, (c) 18cm, and (d) 24cm.

However, distinctive discrepancy is found in shear force measurement. The integrated image processing and control volume analysis gave a shear force loads oscillating more severely between 0.2-0.6N with a seemingly mean of 0.4N that greatly exceeds the value of 0-0.2N (with a factor 2 multiplied) from the shear load cell. Such overestimation is attributed to either erroneous PTV or counting too many

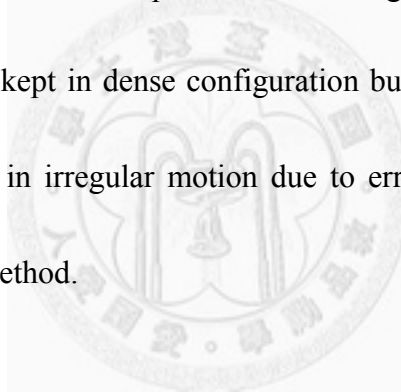
spheres in our image analysis as explained below.

From figure 5.10(b), the signal from shear load cell decreases in time in the range of 0~0.1N with the examination time. At first, we suspected an overestimation of the 3D solid volume fraction from the 2D projection area. However, the good agreement in the normal load estimation rules out this possible cause since F_N in equation (5.3-c) depends totally on ϕ . We noticed that the spheres running over the load cell box is rather dilute with severe bouncing and random sphere motions. Thus, we turned to check if we matched the wrong spheres in the PTV algorithm as in the analysis for impact force. We performed manual PTV on six consecutive images like before and used these instantaneous data to obtain a mean and its standard deviation. We deliberately chose a few instantaneous moments for this comparison as those indicated in table 5.1. Much improved agreement is found to the in-situ load cell data.

Table 5.1 Shear force estimated from CV analysis of manual PTV data

θ \ Packing	W=6 cm	W=12 cm	W=18cm	W=24cm
23°	At 1sec : 0.1207 ± 0.05N	At 3sec : 0.1093 ± 0.05N	At 5sec : 0.0571 ± 0.02N	At 7sec : 0.0628 ± 0.06N
26°	At 2sec : 0.0936 ± 0.04N	At 4sec : 0.0566 ± 0.01N	At 6sec : 0.0667 ± 0.05N	At 8sec : 0.0492 ± 0.02N

From this chapter, we observed that every force component—impact, shear, and normal loads—remained nearly constant shortly after a steady granular flow hit the load cell module. The packing geometry and hence the total number of reservoir spheres did not affect the steady force magnitudes but only extended the duration of nearly constant force plateau. We also estimated these force components indirectly via two-dimensional control volume analysis on bulk streamwise momentum using high-speed images and compared the results to the direct load-cell measurements. The current image analysis algorithm is capable of estimating granular force components when the flowing spheres kept in dense configuration but becomes ineffective when the spheres are loose and in irregular motion due to erroneous PTV data from the present nearest neighbor method.



Chapter 6 Conclusions and Future Aspect

In this thesis, we established a laboratory-scale facility to study the interaction force between a steady granular flow and a obstacle on an inclined chute. The experimental facility (see figure 2.1) includes a reservoir of packing width W and height H , an inclined chute at angle θ , high-speed image acquisition system, and load cell sensing modules. Two types of load cell modules developed and calibrated individually in this work: one measuring only the normal force to determine an overall mass flow rate and the duration of a steady flow; the other acting as an obstacle on the incline and sensing both the shear and the normal force as the bulk impacted and crossed it (see figure 2.3 and 2.4).

We recorded the sphere motions by high-speed image acquisition system from the side and developed an image processing routine to measure individual sphere motion. This routine integrates the circular Hough transformation to locate sphere center in each image followed by the nearest neighbor method to pair the same spheres in two consecutive images to achieve particle tracking velocimetry (PTV). The errors in locating and matching spheres were estimated and provided in table 3.1 and table 3.2, respectively.

We installed the load cell module on the chute at a streamwise distance 100 cm

away from the reservoir and prepared chute of different inclination angles θ and two depths, h . We released granular mass from the reservoir of fixed gate opening and let steady flow develop on the chute and run over the load cell module. We received signals from different components in the load cell module and compared the data to the 2D image control volume analysis. At $\theta=20^\circ$ and $h=4.8$ cm, the granular flow cannot climb over the load cell module but accumulated in front of the impact surface, producing a clear impact force of 4~5N but zero normal and shear force. At $\theta=20^\circ$ and $h=2.4$ cm, the flow developed two distinctive packing configurations in front of the impact surface and for the one in random configuration, a ‘jammed and collapsed’ cycle was observed during and little granular mass crossed the module during the ‘collapsed’ phase. Fluctuating impact force of 3~6N was measured and the resulting normal and shear force loadings are highly unsteady and of nearly zero magnitude. These load cell data at low inclination angle ($\theta=20^\circ$) and the images of different packing configurations are given in figures 5.2, 5.3, and 5.4. For shallow flow ($h=2.4$ cm) at higher inclination angle, $\theta=23^\circ$ and 26° , the resulting flow is composed of fierce sphere bouncing motion over the load cell box giving a rather steady load cell signal over time in figures 5.5 and 5.6: about 1N impact force in the front load cell and 0.2N normal loading on the rear load cell. A nearly zero shear force was detected due to short contact time. For thicker flows with $h=4.8$ cm at $\theta=23^\circ$

and 26° , steady flows developed across the load cell module with a noticeable stationary zone of height around $7\sim 9D$ in front of the impact plate (see Figure 5.7). The running spheres formed a thin layer—of averaged depth around $3D$ —over the rear shear- and the normal-loading plates. The impact force magnitudes fell nicely in the range of $5\sim 7N$ and the shear and normal forces remained slightly below $0.1N$ and around $0.2N$, respectively. These steeper and thicker flow data are shown in figures 5.8, 5.9, and 5.10.

We then applied two-dimensional control volume analysis to the bulk momentum using the captured lateral images to estimate the interaction force with the obstacle (load cell module). The obtained 2D data was multiplied by the chute width to obtain an equivalent 3D force component which was compared to the three-dimensional in-situ load cell measurements for evaluation. We only compared steeper and thicker flows (with $h=4.8\text{cm}$ and $\theta=23^\circ, 26^\circ$) since the bouncing sphere motions in the steep shallower flow invalidated the current PTV matching algorithm. The mild flows at $\theta=20^\circ$ were not considered since no steady flow could develop across the load cell module. The methodology of control volume analysis is described in section 5.3. We compared the impact force first and found out that the control volume analysis results matched reasonably well with the in-situ load cell measurements when the largest control volume width ($\sim 35D$) was employed.

However, when we shrank the CV width towards the impact surface to $1/3$ and $2/3$ original value, severer fluctuations were obtained. This phenomenon was speculated to result from erroneous PTV data for more dilute and chaotic flow near the load cell. We thus conducted manual matching and much improved results were obtained. The relevant results are shown in figures 5.13~5.18. We also examined the shear and normal loadings and obtained agreeing results for the normal loading but total failure for the shear loading (see figures 5.19 and 5.20). We repeated manual PTV at a few chosen moments (see table 5.1) and the results now fell nicely in the range of in-situ load cell data. We thus conclude that the current image analysis is capable of granular force estimation only when the flowing spheres are in dense configuration.

Apart from interaction forces from a steady flow, we also studied the discharging characteristics of reservoir materials in different packing geometries. We placed the reservoir at small 4 degrees on a horizontal hoister with a fixed gate opening of 10cm height. Experimental POM spheres of nearly identical diameter were packed to different widths, W , and heights, H . To quantify a total mass flow rate, we put a plastic container to receive the discharged spheres. The accumulated sphere total weight was monitored over time by the aforementioned load cell module with its measuring surface laid at the center of the container base. The temporal profile of accumulated weight was employed to identify a steady discharge and we found out

that enlarging the packing width (W) and height (H) could extend the steady duration (see figure 4.2). We further defined “deviation time” to denote the termination of steady discharge from a specific packing geometry (see section 4.2.1). The following unsteady discharge was also analyzed the difference from an steady discharge and a peculiar deviating temporal profile for unsteady discharge was revealed for the flow from the narrowest packing. For the narrowest, the deviation from the steady discharge scales with $e^{3.25t^{0.25}}$ but a much milder deviation, $e^{1.25t^{0.45}}$, was detected for all the flows from thicker packing widths (W=12cm, 18cm, and 24cm).

As an attempt to understand the discharge nature, a high-speed camera was installed to record the sphere motions by the side of the connection guide that where the spheres flowed from the reservoir gate to the container (or the chute). The sphere motions and hence the bulk flow properties were analyzed at three streamwise locations—at the reservoir gate, at the guide center, and by the guide exit—with a 7-cm separation (see figure 4.1). We examined the instantaneous depth profiles for bulk velocity and solid volume fraction in figure 4.7 to figure 4.10. We also computed the corresponding depth-averaged values using equations 4.3(a) and 4.3(b) for flows from each packing geometry and their temporal variations are compared (see figures 4.12 and figure 4.14). We noticed that the narrowest packing gave distinctive temporal profiles for the depth-averaged bulk velocity and solid volume fraction. The instant

when a depth-averaged solid volume fraction drops was found to coincide with when the depth-averaged velocity changed dramatically.

For future perspectives, we would like to examine a wide range of flow conditions to see whether the findings of this thesis are universal to other dry granular flows. Flow conditions that may be explored include: thinner W and H , spheres of different density and sizes, chute widths, heights, and inclination angles, and where to install the load cell obstacle.



Reference

- [1] D. M. Mueth, H. M. Jaeger, and S. R. Nagel, “Force distribution in a granular medium”, *Physical Review E* 57, 3164, 1998
- [2] C. Josserand, P. Y. Lagr´ee, and D. Huillier, “Granular pressure and the thickness of a layer jamming on a rough incline”, *Laboratoire de Mod´elisation en M´ecanique*, 2008
- [3] A. V. Ermoshkin and I. Erukhimovich, “Towards a statistical theory of associating telechelics: equilibrium molecular structural distribution and one-cluster static scattering”, *Journal of Chemical Physics*, vol. 110, no. 3, 1998
- [4] A. A. Mills, S. Day, and S. Parkers, “Mechanics of the sandglass”, *Eur.J.Phys.* 97-109, 1996
- [5] G. Y. Onoda and E. G. Liniger, “Random loose packings of uniform spheres and the dilatancy onset” *Physical Review Letters*, vol. 64, no. 22, 1990
- [6] F. Radjai and D. E. Wolf, “Features of static pressure in dense granular media” *Granular Matter* vol.1, 3-8, 1998
- [7] “*Understanding Data Converts*”, Application report, Texas instrument, 1995

- [8] O. Pouliquen and N. Renaut, “Onset of granular flows on an inclined rough Surface: dilatancy effects” *J. Phys. II France* 923-935, 1996
- [9] R. Valentino, G. Barla, and L. Montrasio, “Experimental analysis and micromechanical modelling of dry granular flow and impacts in laboratory flume tests” *Rock Mech. Rock Engng*, vol.41, no.1, 153–177, 2008
- [10] C. A. Yeh, “In-situ measurements of unsteady hydro dynamic forces on a solid boundary using strain-gage based transducers”, Department of Mechanical Engineering, College of Engineering, Nation Taiwan University, 2010
- [11] L. H. Huang, “Dynamics of two-phase granular nixture in a rotating drum with a focus on liquid effect”, Department of Mechanical Engineering, College of Engineering, National Taiwan University, 2010
- [12] S. Knight, “A constitutive law for granular flows: Predicting the appearance of static zones”, *Rayleigh-Knight essay*, Department of Applied Mathematics and Theoretical Physics, University of Cambridge, 2008.
- [13] C. Ancey, “Dry granular flows down an inclined channel: Experimental investigations on the frictional-collisional regime”, *Physical Review E*, vol. 65, 011304, 2001
- [14] H. Capart, D. L. Young, and Y. Zech, “Voronoi imaging methods for the

measurement of granular flow”, *Experiments in Fluids*, 32, 121-135, 2002

[15] J. M. N. T. Gray, Y. -C. Tai, and S. Noelle. “Shock waves, dead zones and particle-free regions in rapid granular free-surface flows”, *J. Fluid Mech*, vol. 491, pp. 161–181, 2003

[16] S. F. Edwards and R. B. Oakeshott, “Theory of powders”, *Physica*, vol.A157, 1080-1090, 1989

[17] GDR MiDi, “On dense granular flows”, *Eur Phys.*, JE 14, 341, 2004

[18] Y. Forterre and O. Pouliquen, “Flows of dense granular media”, *Annu Rev Fluid Mech*, 40, 1, 2008

[19] C. S. Campbell and C. E. Brennen, ”Computer simulation of granular shear flows,” *J. Fluid Mech.* 151, 167, 1985

[20] L. Bocquet, W. Losert, D. Schalk, T. C. Lubensky, and J. P. Gollub, “Granular shear flow dynamics and forces: Experiment and continuum theory”, *Phys. Rev. E* 65, 011307, 2001

[21] I. S. Aranson, and L. S. Tsimring, “Continuum theory of partially fluidized granular flows”, *Phys. Rev. E* 65, 061303, 2002

[22] P. Jop, Y. Forterre, and O. Pouliquen, “A constitutive law for dense granular

flows”, *Nature* 441, 727–731, 2006

[23] H. M. Jaeger, R. S. Nagel, and R. P. Behringer, “Granular solids, liquids and gases”. *Rev. Mod. Phys.* 68, 1259, 1996

[24] R. C. Daniel, A. P. Poloski, and A. E. S’aez, “A continuum constitutive model for cohesionless granular flows”. *Chem. Eng. Sci.* 62, 1343–1350, 2007

[25] P.Jop, Y.Forterre and O.Pouliquen, “Crucial role of side walls for granular surface flows: consequences for the rheology”. 2005

[26] Chung, Y.C., Hsiau, S.S., Liao, H.H. and Ooi, J.Y. “An improved PTV technique to evaluate the velocity field of non-spherical particles” *Powder Technology* 202, 151-161. 2010

